

Flow induced crystallization of polyolefins

Citation for published version (APA):

Balzano, L. (2008). *Flow induced crystallization of polyolefins*. [Phd Thesis 1 (Research TU/e / Graduation TU/e), Chemical Engineering and Chemistry]. Technische Universiteit Eindhoven.
<https://doi.org/10.6100/IR632386>

DOI:

[10.6100/IR632386](https://doi.org/10.6100/IR632386)

Document status and date:

Published: 01/01/2008

Document Version:

Publisher's PDF, also known as Version of Record (includes final page, issue and volume numbers)

Please check the document version of this publication:

- A submitted manuscript is the version of the article upon submission and before peer-review. There can be important differences between the submitted version and the official published version of record. People interested in the research are advised to contact the author for the final version of the publication, or visit the DOI to the publisher's website.
- The final author version and the galley proof are versions of the publication after peer review.
- The final published version features the final layout of the paper including the volume, issue and page numbers.

[Link to publication](#)

General rights

Copyright and moral rights for the publications made accessible in the public portal are retained by the authors and/or other copyright owners and it is a condition of accessing publications that users recognise and abide by the legal requirements associated with these rights.

- Users may download and print one copy of any publication from the public portal for the purpose of private study or research.
- You may not further distribute the material or use it for any profit-making activity or commercial gain
- You may freely distribute the URL identifying the publication in the public portal.

If the publication is distributed under the terms of Article 25fa of the Dutch Copyright Act, indicated by the "Taverne" license above, please follow below link for the End User Agreement:

www.tue.nl/taverne

Take down policy

If you believe that this document breaches copyright please contact us at:

openaccess@tue.nl

providing details and we will investigate your claim.

Flow induced crystallization of polyolefins

PROEFSCHRIFT

ter verkrijging van de graad van doctor aan de
Technische Universiteit Eindhoven, op gezag van de
Rector Magnificus, prof.dr.ir. C.J. van Duijn, voor een
commissie aangewezen door het College voor
Promoties in het openbaar te verdedigen
op woensdag 16 januari 2008 om 14.00 uur

door

Luigi Balzano

geboren te Pompeï, Italië

Dit proefschrift is goedgekeurd door de promotoren:

prof.dr. S. Rastogi

en

prof.dr. P.J. Lemstra

Copromotor:

dr.ir. G.W.M. Peters

A catalogue record is available from the Eindhoven University of Technology Library

ISBN: 978-90-386-1199-0

Copyright © 2008 by L. Balzano

Printed at the Universiteitsdrukkerij, Eindhoven University of Technology, Eindhoven.

Cover design: Luigi Balzano and Bregje Schoffelen (Oranje Vormgevers)

The research described in this dissertation was financially supported by the Dutch Polymer Institute.

(DPI) project # 132.

Table of Contents

Summary	1
Chapter 1 Introduction	3
1.1 <i>Preamble.....</i>	3
1.1.1 Process-properties relation	3
1.1.2 Historical survey on polyethylene and polypropylene.....	4
1.2 <i>Processing of polyolefins.....</i>	5
1.3 <i>Aim of the thesis</i>	7
1.4 <i>Outline of the thesis.....</i>	8
1.4.1 iPP melts containing small amount of DMDBS.....	8
1.4.2 PE melts with a bimodal molecular weight distribution	9
1.4.3 iPP with unimodal molecular weight distribution.....	9
1.5 <i>References.....</i>	10
Chapter 2 Flow induced crystallization in iPP-DMDBS blends: implications on morphology of shear and phase separation	13
2.1 <i>Introduction</i>	14
2.2 <i>Experimental method</i>	16
2.2.1 Materials.....	16
2.2.2 Sample preparation	17
2.2.3 X-Ray characterization.....	17
2.2.4 Rheological characterization	19
2.2.5 DSC.....	19
2.3 <i>Results and discussion</i>	20
2.3.1 Effects of DMDBS on structure and morphology of iPP in the solid state	20
2.3.2 Crystallization under quiescent conditions	22
2.3.3 Morphology of the system in Region II	26

2.3.4	Rheology of the system in Region II	29
2.3.5	Effect of flow on iPP-DMDBS blends near the gel transition	31
2.3.6	Morphological implications of flow and DMDBS phase separation on the crystallization of iPP	34
2.4	<i>Conclusions</i>	36
2.5	<i>References</i>	38

Chapter 3 Thermo-reversible DMDBS phase separation in iPP: effects on flow induced crystallization 41

3.1	<i>Introduction</i>	41
3.2	<i>Experimental method</i>	43
3.2.1	Materials.....	43
3.2.2	Sample Preparation	43
3.2.3	X-Ray Characterization	44
3.2.4	Rheological Characterization.....	45
3.2.5	DSC.....	45
3.3	<i>Results and discussion</i>	45
3.3.1	Thermoreversibility in the phase diagram	45
3.3.2	Linear viscoelasticity of the system in Region I-PS.....	52
3.3.3	Crystallization on cooling after flow in Region I-PS.....	53
3.4	<i>Conclusions</i>	58
3.5	<i>References</i>	59

Chapter 4 Crystallization and dissolution of flow induced precursors 63

4.1	<i>Introduction</i>	63
4.2	<i>Experimental method</i>	65
4.2.1	Synthesis of a bimodal HDPE.....	65
4.2.2	X-ray characterization	66
4.3	<i>Results and discussion</i>	67
4.3.1	Rheological characterization	67

4.3.2	Thermodynamics of flow induced precursors.....	70
4.3.3	Flow induced precursors just above the equilibrium melting temperature	72
4.4	<i>Conclusions</i>	79
4.5	<i>References</i>	79
Chapter 5 Precursors, crystallization and melting in sheared bimodal HDPE melts		83
5.1	<i>Introduction</i>	84
5.2	<i>Experimental method</i>	85
5.2.1	Material preparation	85
5.3	<i>Characterization</i>	85
5.3.1	Rheology	85
5.3.2	Small Angle X-Ray Scattering (SAXS).	86
5.3.3	Wide Angle X-Ray Scattering (WAXS or WAXD).	86
5.3.4	Shear experiments.....	87
5.4	<i>Results and discussion</i>	87
5.4.1	Flow induced precursors above the equilibrium melting temperature	87
5.4.2	Stable and relaxing precursors above the equilibrium melting temperature	90
5.4.3	Flow induced shishes below the equilibrium melting temperature: the influence of temperature	91
5.4.4	Flow induced shishes below the equilibrium melting temperature: the influence of flow conditions.....	93
5.4.5	Separating shish creation from the kebab crystallization.....	95
5.4.6	Crystallization onset temperature after short term shear.....	100
5.4.7	Melting of shish kebabs.....	101
5.5	<i>Conclusions</i>	103
5.6	<i>References</i>	104

Chapter 6 Metastable structures <i>during</i> fast short term shear	107
6.1 <i>Introduction</i>	107
6.2 <i>Materials and methods</i>	109
6.2.1 <i>Materials</i>	109
6.2.2 <i>X-ray characterization</i>	109
6.2.3 <i>Shear experiments</i>	111
6.3 <i>Results and Discussion</i>	112
6.3.1 <i>Flow conditions in short term shear</i>	112
6.3.2 <i>Flow induced precursors during short term shear</i>	113
6.3.3 <i>Crystallization after short term shear.</i>	114
6.4 <i>Conclusions</i>	121
6.5 <i>References</i>	121
Chapter 7 Conclusions and recommendations	125
7.1 <i>Conclusions / Technology assessment</i>	125
7.2 <i>Recommendations for future research</i>	126
Samenvatting	129
Acknowledgements.....	133
Curriculum Vitae	135

Flow induced crystallization of polyolefins

Polymers are a widespread class of materials that provide an often advantageous combination of properties. Easy processability and high versatility combined with low costs make polymers *the* materials for an increasing number of high-tech and commodity applications. Semi-crystalline polyolefins are an important class of polymers, produced in more than 150 million metric tons per year. They are used to make a wide range of products ranging from fibers with superior mechanical properties to flexible packaging and molded parts. The properties of these materials are related to the whole history of the material, from chemistry/catalysis in the reactor and, in particular, to the processing conditions. Nowadays, there is a growing interest in added value to these products by achieving outstanding properties such as high stiffness (up to ~ 150 GPa) for fibers and clarity for injection molded parts. This demands more thorough studies on the process-properties relation that is not yet fully understood.

The main objective of this thesis is to enhance the nucleating efficiency of the polymer by inducing oriented structures possessing good epitaxial matching. The goal is achieved by developing the oriented structures in polymer melt either by (a) making use of fillers that self assemble into nano sized fibrils and orient under flow or (b) by the addition of identical higher molar mass molecules possessing considerably higher relaxation times compared to the base (matrix) polymer.

In the first part of the thesis, the crystallization of isotactic polypropylene (iPP) in the presence of 1,3:2,4-bis(3,4-dimethylbenzylidene)sorbitol (DMDBS) is discussed. DMDBS is a small organic compound with a high melting temperature (~ 250 °C) used as a nucleating agent and so-called clarifier for iPP. The nucleating efficiency of this compound, in the low concentration regime (less than 1 wt%), is very high and leads to very small iPP crystallites

that confer clarity to the material. DMDBS can crystallize within the molten polymer matrix forming a percolated network of nano-fibrils whose surface hosts a large number of tailored nucleation sites. Because of the epitaxial relation between iPP and DMDBS, iPP lamellae grow always radially on DMDBS fibrils, i.e. with the crystalline c-axis parallel to the fibril axis, the so the so-called shish-kebab morphology (rather similar to the well-known food product). Therefore, the orientation of DMDBS fibrils templates the orientation of iPP lamellae. Randomly oriented DMDBS fibrils lead to randomly oriented iPP lamellae and aligned DMDBS fibrils lead to aligned iPP lamellae. A long lasting alignment of DMDBS fibrils can be obtained deforming their network even above the melting point of the polymer. Nearly 0.5 wt% of oriented DMDBS fibrils can template very oriented (fiber-like) polymer morphologies.

In the second part of this thesis, the flow induced crystallization of high density polyethylene (HDPE) with a bimodal molecular weight distribution is discussed. This material is an intimate blend of low and high molecular weight polymer chains (LMW and HMW) synthesized with a new chemistry route as described in the thesis of N. Kukalyekar (Ph.D. thesis Eindhoven University of Technology, December 2007). Just above the equilibrium melting temperature ($T_m^0 = 141.2\text{ }^\circ\text{C}$) of the polymer, the mutually entangled HMW chains can be stretched with shear and, due to the restricted number of molecular conformations, nucleate into needle-like crystals. By choosing appropriate flow conditions, a suspension of shishes (extended chain crystals) can be formed while the nucleation of kebabs (folded chain crystals) is suppressed because of a too high temperature. With perfect epitaxy matching and a good state of dispersion, shishes are the ideal substrate for the nucleation of HDPE lamellae. On cooling after the application of shear at $142\text{ }^\circ\text{C}$, HDPE lamellae nucleate using shishes as a heterogeneous substrate and, therefore, with the crystalline c-axis parallel to the shish direction. Similarly to the case of iPP-DMDBS blends, it is observed that nearly 0.5 wt% of pre-aligned shishes can template very oriented (fiber-like) morphologies.

Chapter 1

Introduction

1.1 Preamble

1.1.1 Process-properties relation

Polymeric materials exhibit an intricate process-properties relationship that links the properties of the final products to the whole history of the material. Figure 1.1 describes the connections from synthesis, via processing, to product properties.

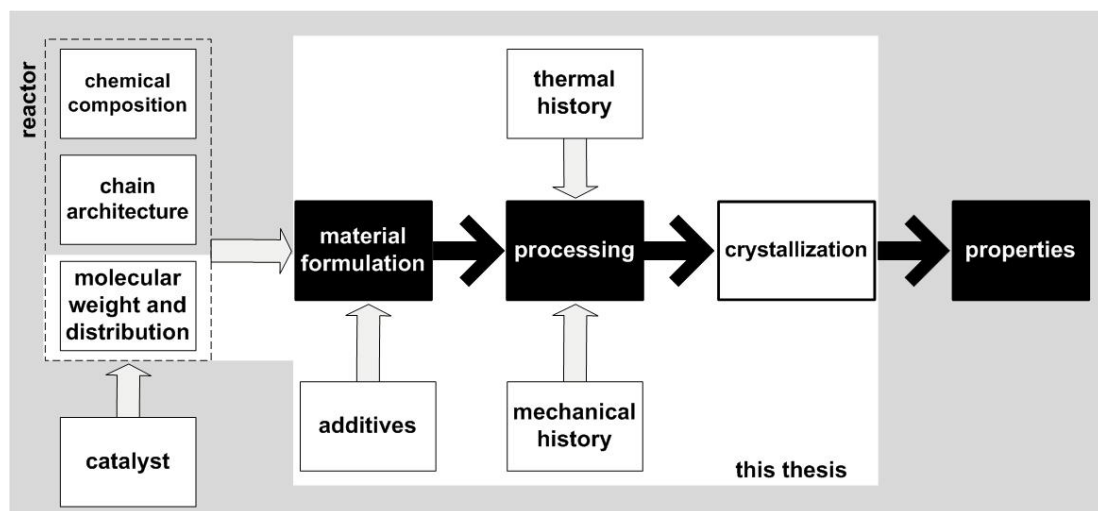


Figure 1.1: Flow chart describing the process-properties relationship in semi-crystalline polymeric materials.

In the last decades, many scientific studies have been devoted to identify relevant parameters and their role in this relationship. Interdisciplinary efforts have led to the production of new materials, with advantageous properties, that have replaced traditional ones (glass, ceramics, metal, wood, ...) in many applications and have enabled developments in new areas, like micro-electronics and biomedical applications. However, some aspects of the process-properties relation in polymeric materials are not yet fully understood. Their clarification could lead, eventually, to materials with properties tailored to the application. A

modern shift in industrial paradigms demands to achieve this goal without developing ‘new’ polymers but, instead, making use of ‘old’ polymers that are based on relatively cheap and readily available monomers¹. For many applications, polyolefins are the ideal candidates.

1.1.2 Historical survey on polyethylene and polypropylene

Polyolefins are commodity materials obtained by polymerizing olefins (alkenes-1). Nowadays, with more than 150 million metric tons² per year, polyolefins are the most widespread class of polymers. Polyolefins are inert materials and, when recycled, environmentally harmless. The number of products based on these materials, from packaging to ballistic, from structural to biomedical applications, increases every day.

The simplest polyolefin is polyethylene (PE) that is a sequence of ethylene monomers. Polyethylene was discovered in the 1930s by Fawcett and Gibson at ICI in strong collaboration with prof. T. Michels of the Free University of Amsterdam who pioneered the behavior of gases at elevated pressures. The first industrial PE grades were produced by the English company ICI in 1939. Initially, it was possible to produce only a highly branched and with low density PE (LDPE). This highly amorphous material, with high toughness, is still used in today’s packaging applications. A major breakthrough came in the 1950s, when Ziegler³ and Natta^{4, 5} (1963 Nobel Prize in Chemistry laureates) discovered organometallic catalysts capable of synthesizing high density linear polyethylene (HDPE). Because of a regular chain structure, HDPE can partially crystallize and it exhibits better mechanical properties. In the 1960s, polyethylene attracted the attention of physicists. Pennings⁶ and Keller⁷ pioneered the formation of elongated crystals (shish-kebabs) in stirred solution and stressed melts. At the same time, Ward⁹ found that upon solid state drawing of melt crystallized HDPE, re-organization of the molecules increases the E-modulus up to 60 GPa. These studies unveiled the role of the morphology in the properties of semicrystalline materials, enabling developments in the area of high performance materials from flexible molecules. At the end of the 1970s, at DSM Research in the Netherlands, Smith and Lemstra^{10, 11} invented a process to spin ultra high molecular weight PE (UHMWPE) from a semi-dilute solution. After drawing, E-moduli of up to 150 GPa could be achieved. One of the last breakthroughs was at the end of the 1970s, when Kaminsky¹² discovered metallocene

catalysts allowing for narrow molecular weight distributions and enhancing the control over chain structure of homo- and co-polymers.

The second simplest polyolefin is polypropylene (PP) that is obtained by polymerizing propylene. PP is basically PE with a methyl side group every other carbon atom in the back-bone. The relative orientation of the side groups in the space (tacticity) is very important for the properties of the material. Atactic PP (aPP), with randomly distributed side groups, can not crystallize and is a rubbery material. In contrast, isotactic PP (iPP), with the side groups consistently on one side, has the necessary long range order required for crystallization. iPP is a competitor for HDPE because it has a higher melting point and can be made transparent with the use of clarifying agents. The synthesis of iPP was enabled by Ziegler-Natta catalysts¹³ and was performed, for the first time, by the Italian company Montecatini in 1957.

1.2 Processing of polyolefins

This thesis deals with topics closely related to melt-processing of polyolefins. Polyolefins are often processed via the molten state, applying flows and temperature gradients. Melt-processing has the advantage of not involving solvents and can be used to create complicated shapes. However, with the design of a manufacturing process for polyolefins and, more in general, for all polymeric materials, one should also consider parameters like molecular weight (M_w) and molecular weight distribution (M_wD). It is well established that the viscosity of the melt (η) scales with M_w according to a power law¹⁴⁻¹⁸: $\eta \propto M_w^{3.4}$. Melt-processing is possible only for relatively low molecular weight materials. In the other cases, more complicated routes are available but, often, they are limited to simple profiles, mostly fibres and tapes.

Flow during processing enhances the crystallization rate of the polymer by promoting the formation of nuclei of the crystalline phase¹⁹⁻³³. This alters the final morphology of the polymer and thus the (mechanical, optical, transport, ...) properties of the material^{34, 35}. Remarkably, the final morphology of the polymer strongly depends on the structures, called *precursors*, present in the early stages of crystallization. These precursors are structures with undetectable degree of crystallinity but with a certain degree of order. Occasionally, because

of local density fluctuations or further growth due to flow, precursors exceed some critical dimensions and become spontaneous growing crystalline nuclei. Flow induced precursors (FIPs) can be generated at relatively high temperatures (i.e. around the thermodynamic melting point) and, for a strong enough flow, exhibit an anisotropic morphology. These precursors can be quite large and they initiate the growth of ‘shish kebabs’; i.e. anisotropic crystallites made of a fibrillar core decorated with a stack of lamellae^{6, 8, 36}. In some cases, shish-kebabs can entirely replace the spherulitic assemblies of lamellae that are characteristic for crystallization in quiescent conditions. This can be advantageous for some polymer products but, definitely, not for all of them. For instance, shish-kebabs cause a high modulus and a high strength in fibres^{10, 37, 38}. In contrast, they can be the source of mechanical weakness (brittleness)^{39,40} in injection-moulded products. Figure 1.2 shows examples of spherulites and shish-kebabs obtained by crystallizing polyolefins under quiescent and flow conditions.

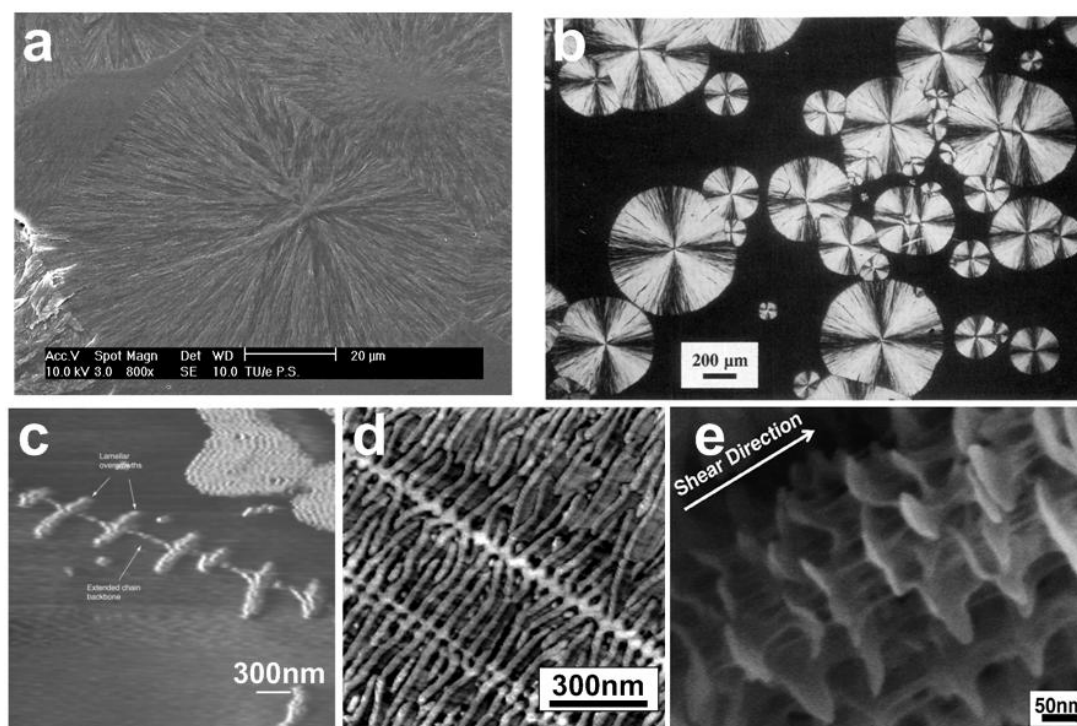


Figure 1.2: a) Scanning electron micrograph of a melt crystallized iPP spherulites (courtesy P.Schmit); b) Optical micrograph of iPP spherulites growing in the melt (reproduced with permission from Figure 2, page 32 of reference 41); c) polyethylene shish-kebab in the melt (reproduced with permission from reference 42); d) Polyethylene shish-kebabs forming zip fastener structures (reproduced with permission from reference 43); e) Multiple shishes crossing the same kebabs in polyethylene (reproduced with permission from Figure 3 of reference 44).

For some polymers, for instance iPP, nucleation is relatively slow and processing is accelerated with nucleating agents (NAs)⁴⁵⁻⁴⁷. NAs have a marked impact on the morphology of the polymer and, by reducing the size of the crystallites, can improve the mechanical properties and reduce the haze. When using NAs, their chemical nature, concentration, dispersion and aspect ratio need to be considered as extra parameters affecting the final morphology of the polymer. In addition, during flow, the nucleating particles influence the local distribution of stresses enhancing the orientation in the surrounding molecules. This phenomenon can be very important in the flow induced crystallization of polymer melts containing fillers⁴⁸.

1.3 Aim of the thesis

The aim of this thesis is to identify basic principles for the onset of oriented morphologies (shish-kebabs) during flow of melt-processable semicrystalline polyolefins.

For polyolefins, the objective is often to achieve the desired properties with melt processing at low costs. When the desired properties are the result of an oriented morphology, the goal can be attained by a) tailoring the melt with small amounts of a ‘smart’ additive or b) with a clever choice of the molecular weight distribution, both in combination with the right processing conditions (temperature and flow history). In our experimental work, we consider three systems:

- iPP containing small amount of 1,3:2,4-bis(3,4-dimethylbenzylidene)Sorbitol or DMDBS;
- PE with a bimodal molecular weight distribution;
- iPP with unimodal molecular weight distribution;

In all cases, molecular weights allowing melt processability are selected.

1.4 Outline of the thesis

1.4.1 iPP melts containing small amount of DMDBS

DMDBS is an additive which is used as a nucleating agent for iPP^{49, 50}. The formula is shown in Figure 1.3. The affinity between this additive and the polymer is very high. Only tiny amounts of DMDBS, less than 1 wt%, cause dramatic changes in the morphology of iPP. Crystal assemblies can become smaller than the wavelength of the light (~400 nm) and turn iPP from an opaque to a clear and transparent material⁵¹.

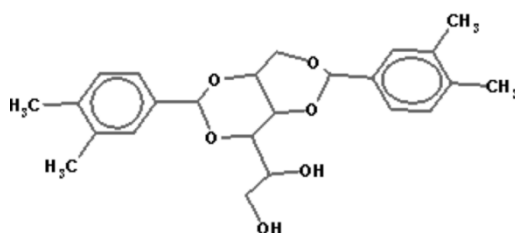


Figure 1.3: Chemical structure of DMDBS.

The polar molecules of DMDBS can dissolve in the molten iPP only at very high temperatures. On cooling, DMDBS self-assembles, phase separating from the melt, and forms a percolated network of fibrils⁵² whose surface hosts nucleation sites tailored for iPP.

The state of the art regarding the crystallization of iPP in presence of small amount of DMDBS is described in the Introduction to Chapter 2 and Chapter 3.

In Chapter 2*, the impact of DMDBS on the crystallization of iPP is discussed. In particular, we address the role of DMDBS fibrils in templating the iPP morphology after flow (shear) at high temperatures where the viscosity of the melt is low and the relaxation times are short.

In Chapter 3†, the thermo-reversibility of DMDBS phase separation is studied and the investigation on the role of DMDBS fibrils in templating the iPP morphology is extended to higher temperatures.

* Partially reproduced from: Balzano, L. et al. 'Flow induced crystallization in iPP-DMDBS blends: implications on morphology of shear and phase separation', *Macromolecules* **2007** (Accepted)

† Partially reproduced from: Balzano, L. et al. 'Thermo-reversible DMDBS phase separation in iPP: effects on flow induced crystallization', *Macromolecules* **2008** (Submitted)

1.4.2 PE melts with a bimodal molecular weight distribution

It is well established that small amounts of high molecular weight chains promote the formation of shish-kebabs during flow induced crystallization^{22, 26, 28, 30, 33, 53-58}. It has been proposed that the underlying mechanism relies on the enhanced creation of flow induced precursors with anisotropic morphology due to stretching of the high molar mass chain network⁵⁹⁻⁶¹. Stretched chains have a high segmental orientation that allows them to crystallize faster than coiled chains^{19, 62} and form fibrillar crystals²¹. To validate this hypothesis, we use a specially synthesized blend of a low molar mass linear HDPE containing 7 wt% of high molar mass linear HDPE. Under shear, this material exhibits a high tendency to generate shish-kebabs. Shish generated at high temperature can be used as a heterogeneous substrate for the nucleation of the rest of the molecules; exact lattice matching and good state of dispersion make them the ideal nucleating substrate.

The state of the art of flow induced crystallization, relevant to the work presented in this thesis, is summarized in the Introduction paragraphs of Chapter 4 and Chapter 5.

In Chapter 4^{*}, the dynamics of flow induced precursors just above the equilibrium melting point is discussed. This investigation unveils, for the first time, the possibility to generate a suspension of extended chain shishes only.

In Chapter 5[†], the investigation on the nature of shishes just above the equilibrium melting temperature is expanded and their potential as nucleators for the bulk of the polymer is systematically explored.

1.4.3 iPP with unimodal molecular weight distribution

In Chapter 4 and 5, the formation of shishes via crystallization of needle-like flow induced precursors is observed at relatively high temperature after the application of shear. Precursors are partially disordered assemblies of molecules and a question on whether they

^{*} Partially reproduced from: Balzano, L. et al. ‘Crystallization and dissolution of flow induced precursors’, *Physical Review Letters* **2007** (Accepted)

[†] Partially reproduced from: Balzano, L. et al. ‘Precursors, crystallization and melting in sheared bimodal HDPE melts’, *Macromolecules* **2008** (Submitted)

can survive during flow arises. In Chapter 6*, this issue is addressed *during* fast short term shear.

1.5 References

1. Warzelhan, V.; Brandstetter, F. *Macromol. Symp.* **2003**, 201, 291-300.
2. Younkin, T. R.; Connor, E. F.; Henderson, J. I.; Friedrich, S. K.; Grubbs, R. H.; Bansleben, B. A. *Science* **2000**, 287, 460-462.
3. Ziegler, K. *Angew. Chem.* **1952**, 64, 323.
4. Natta, G. *J. Polym. Sci.* **1955**, 16, 143.
5. Natta, G.; Corradini, P. *Atti Accad. Nazl. Lincei, Mem.* **1955**, 8, (4), 73.
6. Pennings, J.; Kiel, A. M. *Kolloid ZZ Polym* **1965**, 205, 160.
7. Keller, A. *Phyl. Mag.* **1957**, 2, 1171.
8. Binsbergen, F. L. *Nature* **1966**, 211, 516-517.
9. Capaccio, G.; Ward, I. M. *Nature* **1973**, 243, 130.
10. Smith, P.; Lemstra, P. J. *Journal of Materials Science* **1980**, 15, 505-514.
11. Smith, P.; Lemstra, P. J.; Pijpers, J. P. L.; Kiel, A. M. *Colloid & Polymer Sci.* **1981**, 259, 1070-1080.
12. Kaminsky, W. *Journal of Polymer Science Part A: Polymer Chemistry* **2004**, 42, (16), 3911 - 3921.
13. Natta, G. *Nobel Lecture December 12, 1963*.
14. Doi, M.; Edwards, S. F., *The theory of polymer dynamics*. Clarendon Press: Oxford, 1986.
15. Dealy, J. M.; Larson, R. G., *Structure and Rheology of Molten Polymers*. Hanser Gardner Pubns: Cincinnati, 2006.
16. Macosko, C., *Rheology : principles, measurements, and applications*. VCH: Weinheim, 1994.
17. Rubinstein, M.; Colby, R. H., *Polymer Physics*. Oxford University Press: 2003.
18. de Gennes, P. J., *Scaling concepts in polymer physics*. Cornell University Press: Ithaca, NY, 1979.
19. Devaux, N.; Monasse, B.; Haudin, J. M.; Moldenaers, P.; Vermant, J. *Rheol. Acta* **2004**, 43, 210-222.
20. Heeley, E. L.; Maidens, A. V.; Olmsted, P. D.; Bras, W.; Dolbnya, I. P.; Fairclough, J. P. A.; Terril, N. J.; Ryan, A. J. *Macromolecules* **2003**, 36, 3656-3665.
21. Janeschitz-Kriegl, H.; Eder, G. *Journal of Macromolecular Science, Part B* **2007**, 46, 591-601.
22. Jerschow, P.; Janeschitz-Kriegl, H. *International Polymer Processing* **1997**, 12, (1), 72-77.
23. Kumaraswamy, G.; Issaian, A. M.; Kornfield, J. A. *Macromolecules* **1999**, 32, 7537-7547.
24. McHugh, A. J. *Polym. Eng. Sci.* **1982**, 22, 15-26.
25. Muthukumar, M. *Advances in Chemical Physics* **2004**, 128.

* Partially reproduced from: Balzano, L. et al. 'Metastable structures during fast short term shear', *Macromolecules* **2008** (Submitted)

26. Nogales, A.; Hsiao, B. S.; Somani, R. H.; Srinivas, S.; Tsou, A. H.; Balta-Calleja, F. J.; Ezquerra, T. *Polymer* **2001**, 42, 5247-5256.
27. Pogodina, N. V.; Winter, H. H.; Srinivas, S. *Journal of Polymer Science: Part B: Polymer Physics* **1999**, 37, 3512-3519.
28. Seki, M.; Thurman, D. W.; Oberhauser, J. P.; Kornfield, J. A. *Macromolecules* **2002**, 35, 2583-2594.
29. Somani, R. H.; Yang, L.; Hsiao, B. S. *Physica A* **2002**, 304, 145-157.
30. Van der Beek, M. H. E.; Peters, G. W. M.; Meijer, H. E. H. *Macromolecules* **2006**, 39, (5), 1805 -1814.
31. Yamazaki, S.; Watanabe, K.; Okada, K.; Yamada, K.; Tagashira, K.; Toda, A.; Hikosaka, M. *Polymer* **2005**, 46, 1685-1692.
32. Ziabicki, A.; Alfonso, G. C. *Macromol. Symp.* **2002**, 185, 211-231.
33. Zuidema, H.; Peters, G. W. M.; Meijer, H. E. H. *Macromolecular Theory and Simulations* **2001**, 10, (5), 447 - 460.
34. Schrauwen, B. A. G.; Breemen, L. C. A. v.; Spoelstra, A. B.; Govaert, L. E.; Peters, G. W. M.; Meijer, H. E. H. *Macromolecules* **2004**, 37, 8618-8633.
35. Meer, D. W. v. d.; Pukanszky, B.; Vancso, G. J. *J. Macromol. Sci.-Phys.* **2002**, 41, 1105-1119.
36. Hill, M. J.; Barham, P. J.; Keller, A. *Colloid & Polymer Sci.* **1980**, 258, 1023-1037.
37. Baastiansen, C. W. M., *Oriented structures based on flexible polymers*. PhD thesis, Eindhoven University of Technology: 1991.
38. Govaert, L. E., *Deformation behavior of oriented polyethylene fibers*. PhD thesis, Eindhoven University of Technology: 1990.
39. Ward, I. M., *Structure and properties of oriented polymers*. Chapman and Hall: London, 1997.
40. Schrauwen, B. A. G., *Deformation and failure of semi-crystalline polymers*. PhD thesis, Eindhoven University of Technology: 2003.
41. Basset, D. C.; Franck, F. C.; Keller, A. *Phyl Trans Roy Soc London A* **1994**, 348, 29-43.
42. Hobbs, J. K.; Miles, M. J. *Macromolecules* **2001**, 34, 353-355.
43. Hobbs, J. K.; Humphris, A. D. L.; Miles, M. J. *Macromolecules* **2001**, 34, 5508-5519.
44. Hsiao, B. S.; Yang, L.; Somani, R. H.; Avila-Orta, C. A.; Zhu, L. *Physical Review Letters* **2005**, 94, 117802.
45. Binsbergen, F. L.; de Lange, B. G. M. *Polymer* **1970**, 11, (6), 309-322.
46. Beck, H. N. *Journal of Applied Polymer Science* **1967**, 11, (5), 673 - 685.
47. Binsbergen, F. L. *Polymer* **1970**, 11, (5), 253-267.
48. Hwang, W. R.; Peters, G. W. M.; Hulsen, M. A.; Meijer, H. E. H. *Macromolecules* **2006**, 39, 8389-8398.
49. Thierry, A.; Fillon, B.; Straupe, C.; Lotz, B.; Wittmann, J. C. *Progr. Colloid Polym. Sci.* **1992**, 87, (31), 28-31.
50. Shepard, T. A.; Delsorbo, C. R.; Louth, R. M.; Walborn, J. L.; Norman, D. A.; Harvey, N. G.; Spontak, R. J. *Journal of Polymer Science: Part B: Polymer Physics* **1997**, 35, 2617-2628.
51. Kristiansen, M.; Werner, M.; Tervoort, T.; Smith, P.; Blomehofer, M.; Schmidt, H. W. *Macromolecules* **2003**, (36), 5150-5156.
52. Thierry, A.; Straupe, C.; J.; W.; Lotz, B. *Macromol Symp* **2006**, 241, 103-110.
53. Heeley, E. L.; Morgovan, A.; Bras, W.; Dolbnya, I. P.; Gleeson, A. J.; Ryan, A. J. *Phys. Chem. Comm.* **2002**, 5, 158-160.
54. Yang, L.; Somani, R. H.; Sics, I.; Hsiao, B. S.; Kolb, R.; Lohse, D. *J. Phys. Condens. Matter* **2006**, 18, 2421-2436.

55. Bashir, Z.; Odell, J. A.; Keller, A. *Journal of Materials Science* **1984**, 19, 3713-3725.
56. Kimata, S.; Sakurai, T.; Nozue, Y.; Kasahara, T.; Yamaguchi, N.; Karino, T.; Shibayama, M.; Kornfield, J. A. *Science* **2007**, 316, (5827), 1014 - 1017.
57. Dukovski, I.; Muthukumar, M. *Journal of Chemical Physics* **2003**, 118, (14), 6648-6655.
58. Ryan, A. J.; Fairclough, J. P. A.; Terril, N. J.; Olmsted, P. D.; Poon, W. C. K. *Faraday Discussions* **1999**, 112, (13-29).
59. Keller, A.; Kolnaar, H. W. H., *Flow induced orientation and structure formation*. VCH: New York, **1997**; Vol. 18.
60. Somani, R. H.; Yang, L.; Zhu, L.; Hsiao, B. S. *Polymer* **2005**, 46, 8587-8623.
61. Ogino, Y.; Fukushima, H.; Matsuba, G.; Takahashi, N.; Nishida, K.; Kanaya, T. *Polymer* **2006**, 47, 5669-5677.
62. Coppola, S.; Balzano, L.; Gioffredi, E.; Maffettone, P. L.; Grizzuti, N. *Polymer* **2004**, 45, 3249-3256.

Chapter 2*

Flow induced crystallization in iPP-DMDBS blends: implications on morphology of shear and phase separation

Nucleation is the limiting stage in the kinetics of polymer crystallization. In many applications of polymer processing, nucleation is enhanced with the addition of nucleating agents. 1,3:2,4-bis(3,4-dimethylbenzylidene) sorbitol or DMDBS is a nucleating agent tailored for isotactic polypropylene (iPP). The presence of DMDBS changes the phase behavior of the polymer. For high enough temperatures the system iPP-DMDBS forms a homogeneous solution. However, in the range of concentration spanning from 0 to 1 wt% of DMDBS, the additive can phase separate/crystallize above the crystallization temperature of the polymer, forming a percolated network of fibrils. The surface of these fibrils hosts a large number of sites tailored for the nucleation of iPP. The aim of this Chapter is to investigate the combined effect of flow and DMDBS phase separation on the morphology of iPP. To this end, we studied the rheology of phase separated iPP-DMDBS systems and its morphology with time resolved Small Angle X-ray Scattering (SAXS). The effect of flow is studied combining rheology, SAXS and a short term shear protocol. We found that, with phase separation, DMDBS forms fibrils whose radius (~ 5 nm) does not depend on the DMDBS concentration. The growth of these fibrils leads to a percolated network with a mesh size depending on DMDBS concentration. Compared to the polymer, the relaxation time of the network is quite long. A shear flow, of 60 s^{-1} for 3 s, is sufficient to deform the network and to produce a long-lasting alignment of the fibrils. By design, lateral growth of iPP lamellae occurs orthogonally to the fibril axis. Therefore, with crystallization, the pre-orientation of DMDBS fibrils is transformed into orientation of the lamellae. This peculiarity is used here to design thermo-mechanical histories for obtaining highly oriented iPP morphologies after shearing well above the melting point of the polymer (i.e. without any undercooling). In contrast, when shear flow is applied prior to DMDBS crystallization, SAXS showed that iPP crystallization occurs with isotropic morphologies.

*Partially reproduced from: Balzano, L. et al. 'Flow induced crystallization in iPP-DMDBS blends: implications on morphology of shear and phase separation', *Macromolecules* **2007** (Accepted)

2.1 Introduction

Morphology control is an important issue in polymer processing as it influences a broad range of properties of the final products. For instance, mechanical, optical and transport properties of polymeric materials depend on the size and shape of the crystallites^{1,2}. It is well known that thermal and mechanical histories do play an important role in the creation of these morphological features^{3,4} and that additives can also have a remarkable influence^{2, 5-8}. Nucleating agents are a family of additives used to speed up processing rates of polymers. In the case of isotactic polypropylene (iPP) a common nucleating agent is a sorbitol derivative: 1,3:2,4-bis(3,4-dimethylbenzylidene)sorbitol or DMDBS. DMDBS is a chiral molecule that can self-assemble or crystallize within the molten polymer matrix. Self-assembly takes place because of inter-molecular hydrogen bonds formation. Hydrogen bonds, in this case, work essentially in one direction and drive the molecules to pile up (see Figure 2.1). This leads to the unidirectional growth of fibrillar crystals. Elementary DMDBS fibrils, in iPP, have a diameter of ~ 10 nm and a length up to several microns. They can also form bundles with a diameter up to 100 nm.

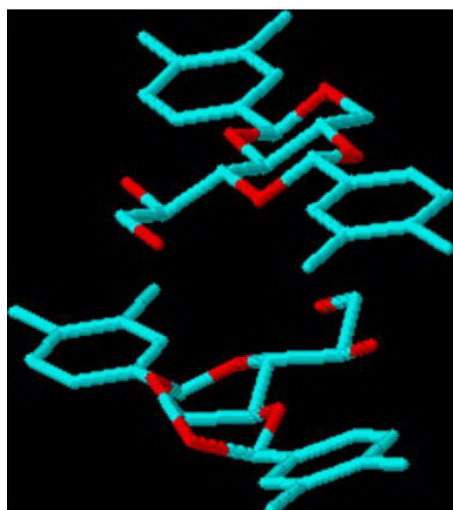


Figure 2.1: A stack of two DMDBS molecules.

Crystallization of DMDBS within the iPP matrix corresponds to a liquid-solid phase separation, in the following, referred to as DMDBS crystallization or DMDBS phase separation. The DMDBS molecule has a special ‘butterfly’ configuration, see Figure 1.3. The ‘wings’ of the molecule (phenyl rings with two methyl groups attached) enable dissolution in the polymer and, at the same time, are tailored nucleation sites for iPP, while the ‘body’

comprises two moieties: one dictates the geometry of the molecule and the other bears the polar groups (hydroxyls) for hydrogen bond formation⁹. Polarity is one of the main features of DMDBS. In contrast, iPP is a fully apolar molecule. This difference becomes clear and leads to a rich phase diagram when iPP and DMDBS are compounded together.

Kristiansen et al.¹⁰ proposed a monotectic model for this phase diagram where the eutectic point lies near 0.1 wt% of the additive. In their model, miscibility of the two molecules is always possible at high temperatures (Region I). They define four concentration regimes based on different phase transitions occurring during the cooling of a homogenous mixture. From the application point of view, the most interesting concentration regime extends from ~0.1 wt% to ~1 wt% of DMDBS where iPP exhibits a high clarity. The phase diagram, in this concentration range, is schematically shown in Figure 2.2.

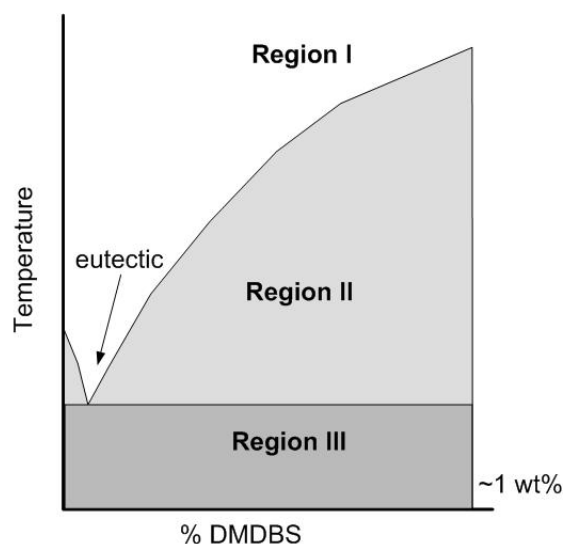


Figure 2.2: Schematic phase diagram for iPP-DMDBS mixtures up to ~1 wt% (quantitative data shown in Figure 2.9).

Cooling a homogeneous mixture (Region I) leads to crystallization of DMDBS before crystallization of the polymer (Region II)¹⁰. With crystallization, DMDBS forms a percolated network of fibrils suspended in the polymer matrix. The nucleation sites for the polymer reside on the surface of this network. The fibrillar arrangement provides a high surface to volume (S/V) ratio and, therefore, a large number of nucleation sites per unit of volume. However, S/V alone cannot explain the nucleation ability of DMDBS. Thierry et al.^{9, 11} and Fillon et al.¹¹ demonstrated that DMDBS is a good nucleating agent for iPP because of a good lattice matching between its crystals and the 3_1 helix of the polymer. The same authors

also define an efficiency scale for nucleating agents, ranging from 0 to 100 %, based on characteristic crystallization temperatures. Dibenzylidene sorbitol (DBS), a nucleating agent very similar to DMDBS, was rated at 41 %. Among several nucleating agents, they found that 4-Biphenyl carboxylic acid (2 wt% in iPP) has the highest nucleation efficiency (66%).

The effect of several sorbitol based nucleating agents on quiescent crystallization kinetics and the morphology of iPP has been widely explored¹²⁻¹⁴, as was the rheology of these systems^{12, 15, 16}. Surprisingly, little attention has been paid to the role of sorbitol based nucleating agents on the crystallization of iPP during or after imposition of a flow, the most common scenario in processing. A notable exception is the work of Nogales et al.^{17, 18}. They studied the flow induced crystallization of iPP-DBS compounds after the phase separation of the additive under well defined conditions, by means of both scattering and imaging techniques. For 1 wt% of DBS, they observed, during cooling, after application of modest shear flows (shear rates ranging from 0.1 to 20 s⁻¹ at 170 °C), the formation of polymer morphologies characterized by high degrees of orientation.

However, the role of DMDBS phase separation in flow induced crystallization of iPP-DMDBS blends is not yet fully clarified and is the topic of this Chapter. The work includes also the changes in the rheology of the melt, associated to the formation of the DMDBS fibrillar network, and the flow behavior of this network. The results are based on a combination of Small Angle X-ray Scattering (SAXS), Dynamic Scanning Calorimetry (DSC) and Rheology. Four different iPP-DMDBS blends, containing 0, 0.3, 0.7 and 1.0 wt% of the additive are investigated in quiescent and flow conditions. We address three aspects of these blends: 1. crystallization without application of flow (quiescent conditions); 2. influence of flow prior to the crystallization of DMDBS; 3. influence of flow after crystallization of DMDBS.

2.2 Experimental method

2.2.1 Materials

The iPP used in this work is a commercial homopolymer grade from Borealis GmbH (Austria), labeled HD120MO, with molecular weight, M_w , of 365 kg/mol and a

polydispersity, M_w/M_n , of 5.4. DMDBS (Millad 3988) was obtained in powder form from Milliken Chemicals (Gent, Belgium) and used as received.

2.2.2 Sample preparation

The polymer, available in pellets, was first cryo-ground and then compounded with DMDBS in a co-rotating twin screw mini-extruder (DSM, Geleen) for 10 min at temperatures ranging from 230 to 250 °C, the higher the DMDBS concentration the higher the compounding temperature used. To prevent degradation of both, polymer and additive, this operation was performed in a nitrogen rich atmosphere. The material obtained was compression molded with a hot press into films of different thicknesses: 1mm for rheology and 200µm for X-ray experiments. The compression molding temperature was 220 °C and the molding time was 3min. The resulting films were quenched to room temperature and cut in disk-like samples. Following the same procedure, three blends of iPP with 0.3, 0.7 and 1 wt% of DMDBS were prepared. For convenience, these three blends are respectively referred to as B03, B07 and B1 in the text.

2.2.3 X-Ray characterization

X-ray characterization was performed at the European Synchrotron Radiation Facility (ESRF) in Grenoble (France). Time resolved Small Angle X-ray Scattering (SAXS) experiments were performed at beamline BM26/DUBBLE. Scattering patterns were recorded on a two dimensional gas filled detector (512x512 pixels) placed at approximately 7.1 m from the sample. Scattering and absorption from air were minimized by a vacuum chamber placed between sample and detector. The wavelength adopted was $\lambda=1.03$ Å. SAXS images were acquired with an exposure of 5 s and were corrected for the intensity of the primary beam, absorption and sample thickness. The scattered intensity was integrated and plotted against the scattering vector, $q = (4\pi / \lambda)\sin(\vartheta / 2)$ where ϑ is half of the scattering angle. The long period was calculated as $L_p = 2\pi / (q_{I_{MAX}})$, where $q_{I_{MAX}}$ is the q value corresponding to the maximum in the scattered intensity. Finally, we defined an integrated intensity as:

$$I_I = \int_{q_{\min}}^{q_{\max}} I(q) dq \text{ where } q_{\min} \text{ and } q_{\max} \text{ are the minimum and the maximum experimentally}$$

accessible q values respectively. Two dimensional SAXS images were also used for the characterization of anisotropic morphologies. For this purpose, it was necessary to define three azimuthal regions¹⁹. The definitions adopted in the present work are given in Figure 2.3.

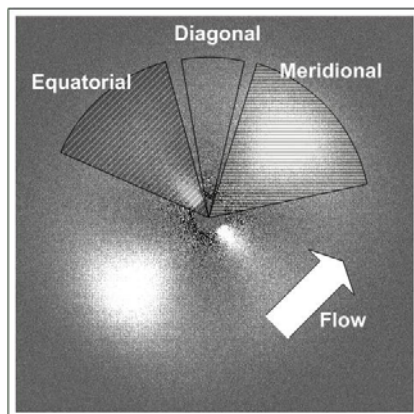


Figure 2.3: Anisotropic two dimensional SAXS image with definitions of the azimuthal intensity regions. Arrow indicates the applied flow direction.

Shear flow experiments in combination with SAXS were carried out in a Linkam Shear Cell (CSS-450) modified with Kapton windows using a ‘short term shearing’ protocol. First, samples were annealed at 230 °C for 3 min to erase the memory of any previous thermo-mechanical treatment. Next, the temperature was decreased by 10 °C/min to the desired test temperature where flow was applied under isothermal conditions. For the purpose of this Chapter, we limit ourselves to the application of only one shear condition: nominal shear rate of 60 s⁻¹ for 3 s. Finally, depending on the experimental requirements, the temperature was either decreased to the room temperature or kept constant.

Wide Angle X-ray scattering (WAXD) experiments were performed separately on beamline ID11 of the ESRF. The results were used to determine crystallinity and the phases present in the samples. Two dimensional images were recorded on a Frelon detector. Before analysis, the scattering of air and of the empty sample holder was subtracted. After radial integration, the intensity was plotted as a function of the scattering angle 2ϑ . Deconvolution of the amorphous and crystalline scattered intensities was performed using a sixth order polynomial to capture the ‘amorphous halo’^{20, 21}. The crystallinity index, a measure of the crystal volume fraction, was calculated as:

$$X^{WAXD} = \frac{A_C}{A_C + A_A} \cdot 100 \quad (2.1)$$

where, A_A and A_C are the scattered intensities from the amorphous and the crystalline phases, respectively.

2.2.4 Rheological characterization

Rheological measurements were performed in the linear viscoelastic regime using a strain-controlled ARES rheometer equipped with a 2KFRT force rebalance transducer. In all cases a plate-plate geometry with a diameter of 8 mm was used. Appropriate values of strain were determined with amplitude sweep tests carried out at 5 rad/s over a broad range of strains (ranging from 0.01 to 100 %) ²². During the study of phase transitions, large strains can enhance the process and/or affect the morphology ²³. These effects are minimized by using strains as low as 0.5 % in the experiments.

2.2.5 DSC

The crystallization behavior of the three binary blends iPP-DMDBS was studied in quiescent conditions using Dynamic Scanning Calorimetry (DSC). Samples of approximately 2 mg were placed into aluminum pans and tested in nitrogen atmosphere in a Q1000 calorimeter (TA Instruments). The first step in the thermal treatment was always annealing at 230 °C for 3 min to erase earlier thermo-mechanical histories. Next, samples were cooled to room temperature at a constant cooling rate of 10 °C/min.

Before identifying peak positions and determining crystallinity, a linear baseline was subtracted from the measured heat flow as a function of the temperature. Finally, crystallinity

could be estimated as: $X^{DSC} = \Delta H_c / \Delta H_c^0$, where $\Delta H_c = \int_{T_s}^{T_c} (dH/dT)dT$ and ΔH_c^0 are, respectively, the enthalpy of crystallization of the sample and the enthalpy of crystallization of an ideal 100 % crystalline iPP sample (207.1 J g⁻¹) ²⁴.

2.3 Results and discussion

2.3.1 Effects of DMDBS on structure and morphology of iPP in the solid state

In semi-crystalline polymers, structure and morphology depend on the crystallization conditions (thermal and mechanical histories). In order to isolate the effects due to the presence of DMDBS in the solid state, samples were prepared under the same crystallization conditions i.e. quiescent crystallization with 10 °C/min. Figure 2.4 reports WAXD integrated intensities at room temperature for the neat iPP and the blends with DMDBS.

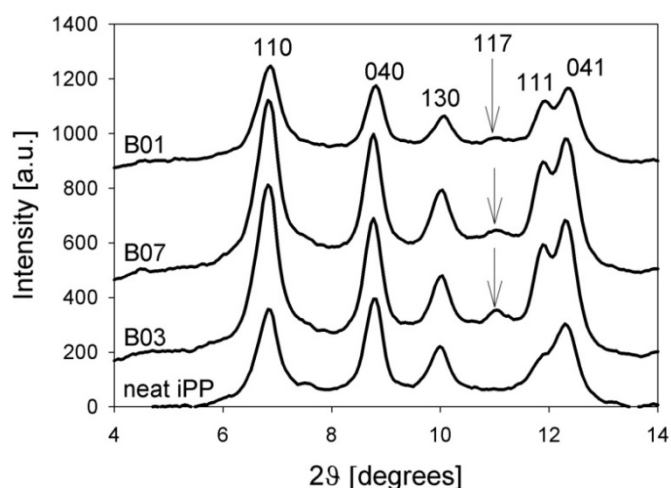


Figure 2.4: WAXD profiles of iPP at room temperature as function of DMDBS concentration. All samples were prepared in the same conditions, i.e. crystallization from the melt at 10 °C/min. Presence of DMDBS induces the broad 117 peak, indicated by the arrow, that is associated to the formation of γ phase crystals. The crystallinity index is $\sim 60\%$ in all cases while the amount of γ phase decreases with DMDBS concentration. Note that, curves are shifted in the vertical direction for clarity.

The neat iPP shows the typical diffraction peaks of the α crystalline modification. When the additive is present, although the α form remains prevalent, the crystal structure of the polymer shows some specific changes. The 111 peak becomes better resolved and a broad 117 reflection appears. This indicates the simultaneous formation of less defected α and small γ crystals. However, we do not observe significant variation in the WAXD crystallinity index; in all cases, it lies around 60%. According to Foresta et al.²⁴, the formation of γ phase crystals in presence of the nucleating agent can be explained from a thermodynamic point of view. The nucleating agent shifts the crystallization of the polymer at higher temperatures

where nucleation of γ phase is favored and can compete with nucleation of α phase. The ratio between γ and α phase crystals, X_γ , can be estimated with:

$$X_\gamma = \frac{A_{117}}{A_{130} + A_{117}} \quad (2.2)$$

where A_{130} and A_{117} are the areas of the non overlapping parts of the 117 and 130 peaks. These two peaks were selected because they are the diagnostic reflections of the γ and the α phase respectively. In the investigated range of concentration, the γ phase content, X_γ , is maximum for B03 ($X_\gamma=0.15$) and drops for B07 ($X_\gamma=0.09$) and B1 ($X_\gamma=0.08$). This drop is probably related to a faster α nucleation rate at higher DMDBS concentrations.

On the morphological side, the long period of iPP lamellae shows pronounced changes as a function of DMDBS concentration going from 19 nm of the neat sample to 23 nm (average value) of samples containing DMDBS, see Figure 2.5.

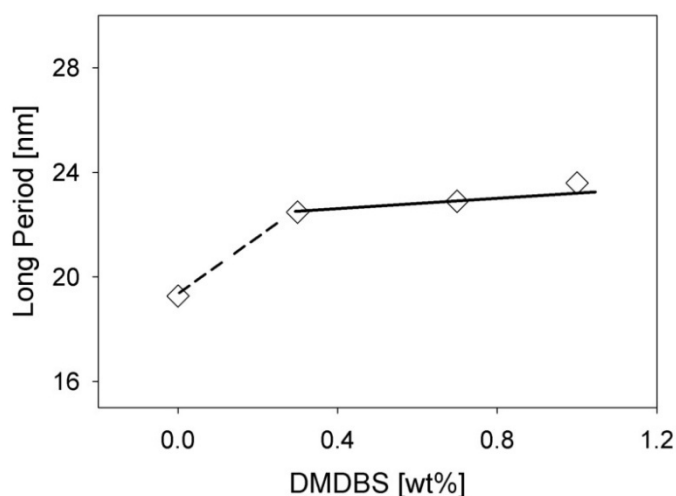


Figure 2.5: Long periods of iPP lamellae at room temperature as a function of DMDBS concentration. All samples were prepared under the same conditions, i.e. crystallization from melt at 10 °C/min. The neat iPP shows a long period of 19 nm and this value rises to ~23 nm for samples containing DMDBS. This increase in long period is due to the formation of thicker crystals in presence of DMDBS

The lamellar thickness, T_L , can be expressed as $T_L = L_p \cdot x$. Since, the crystallinity index does not vary, our experimental observations are consistent with the formation of thicker crystals when DMDBS is present. The reason for this increase in crystal thickness is

the higher crystallization temperature in presence of the nucleating agent⁸ that is discussed hereafter.

2.3.2 Crystallization under quiescent conditions

When cooling a homogeneous mixture of iPP and DMDBS to room temperature, two phase transitions are observed: crystallization of DMDBS and crystallization of the polymer. DSC experiments reveal the temperatures and enthalpies characterizing both these transitions. In the cooling thermograms of Figure 2.6 the crystallization peaks of the polymer are, in all cases, clearly visible. A closer look discloses another, much smaller, exotherm at higher temperatures.

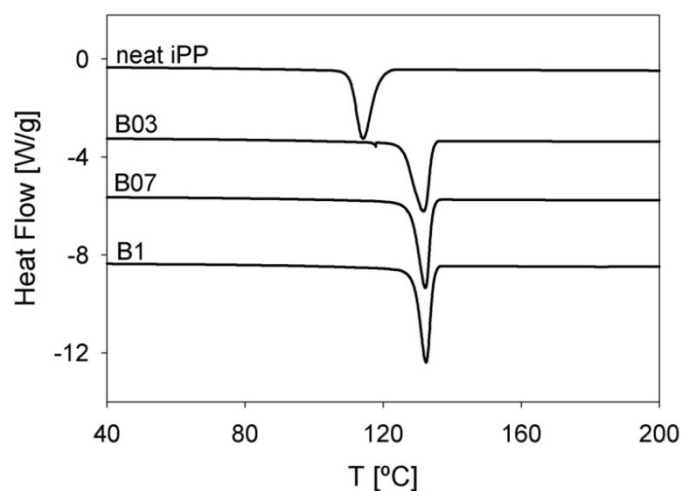


Figure 2.6: DSC cooling thermograms (after subtraction of a linear baseline) for the neat polymer and blends B03, B07 and B1. Experiments were performed at 10°C/min, in N_2 atmosphere, after annealing the samples at 250 °C for 3 min. Curves are shifted along the vertical axis for clarity. With the addition of only 0.3 wt% of DMDBS, the crystallization peak shifts to 132 °C, and its position does not change with further addition of the additive. Nevertheless, the crystallization peak becomes narrower when increasing the amount of DMDBS.

This smaller exotherm is associated with the crystallization of DMDBS and, due to the small amount of the additive, becomes visible only after sufficient magnification, see Figure 2.7. Some relevant DSC data during the cooling experiments are summarized in Table 2.1. Note that these data provide enough information to sketch the phase diagram of the system in the investigated range of concentration.

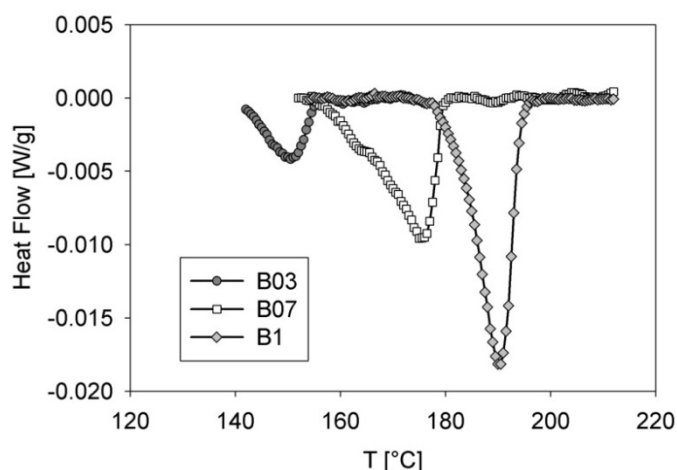


Figure 2.7: Magnification of the cooling experiments of Figure 2.6 in the temperature range preceding the crystallization of the polymer. The small exotherms are associated to the crystallization of DMDBS. As expected, latent heat of crystallization and peak temperature increase with DMDBS concentration. For clarity, curves are shifted to the same baseline.

Table 2.1: Summary of experimental data obtained from DSC data shown in Figure 2.6. T_{peak}^{DSC} and T_{onset}^{DSC} represent peak and onset temperature of the exotherm associated to crystallization of the polymer. t_c is the crystallization time defined as $t_c = (T_{onset}^{DSC} - T_{compl}^{DSC}) / dT/dt$ where T_{compl}^{DSC} corresponds to the completion of the crystallization and dT/dt is the cooling rate ($=10$ °C/min). T_{ps}^{DSC} represents the peak temperature of the exotherm associated to DMDBS crystallization. X^{DSC} is the degree of crystallinity of the polymer.

	T_{peak}^{DSC} [°C]	T_{onset}^{DSC} [°C]	ΔH [J·g ⁻¹]	t_c [s]	T_{ps}^{DSC} [°C]	X^{DSC} [%]
HD120MO	113	120	95.3	123.5		46
0.3% DMDBS – B03	131	135	107.7	68.5	149	52
0.7% DMDBS – B07	132	135	107.7	53.6	175	52
1% DMDBS – B1	132	135	103.5	47.3	189	50

Upon addition of 0.3 wt% of DMDBS, the crystallization temperature (peak value) of iPP, T_c , increases to 131 °C. Further addition of DMDBS has nearly no effect on T_c that is 132 °C for both B07 and B1. Nevertheless, the crystallization peak of the polymer narrows at higher DMDBS contents indicating faster crystallization. Saturation of T_c of iPP with DMDBS concentration was observed also by Kristiansen et al.¹⁰, in their data, T_c reaches ~130 °C at 0.4 wt% DMDBS. Increasing DMDBS concentration, the phase separation occurs

at increasingly higher temperatures. In accordance with WAXD, the final crystallinity of iPP is hardly affected by DMDBS. However, the values measured by DSC, namely 50 %, are noticeably lower than those found with WAXD.

Information on the morphology of the system as a function of the temperature is obtained by means of SAXS. Figure 2.8 shows the integrated scattered intensity as a function of the temperature for the neat iPP and the blends with DMDBS. These data can be interpreted in terms of density fluctuations. As expected, in the neat iPP there is no density fluctuation until the polymer starts nucleating at ~ 120 °C. While, samples containing DMDBS show more complicated temperature dependence. In fact, when phase separation occurs, DMDBS molecules form crystals denser than the polymer.

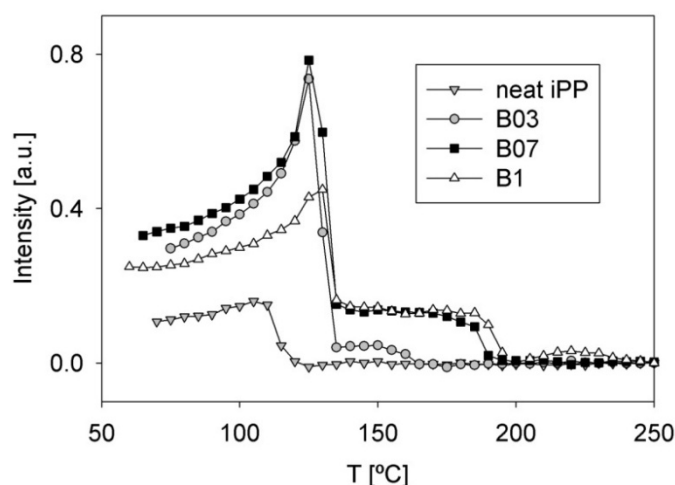


Figure 2.8: Temperature dependence of the SAXS intensity as a function of DMDBS concentration during cooling at 10 °C/min and after annealing at 250 °C for 3 min. In samples containing DMDBS the scattered intensity increases with phase separation because of density fluctuations between DMDBS crystals and the polymer. At lower temperatures, when the polymer crystallizes once again the scattered intensity increases

As a consequence, electron density fluctuations are established and the scattered intensity rises to a plateau. At lower temperature, around 135 °C, independently from DMDBS concentration, nucleation of the polymer triggers a large and abrupt upturn in the intensity. Similar to DSC, some characteristic temperatures for the crystallization of the polymer and of the additive are located and reported in Table 2.2. These data are used to build the phase diagram shown in Figure 2.9 that is used as reference in the rest of this work.

In accordance with Kristiansen et al.¹⁰, three different regions, corresponding to three different physical states of the system, are identified:

Region I: at high temperatures DMDBS and iPP form a homogenous solution;

Region II: at intermediate temperatures the system is phase separated with DMDBS crystallized and iPP molten;

Region III: at low temperatures both DMDBS and iPP are crystallized.

Table 2.2: Summary of the SAXS data obtained from Figure 2.9. T_c^{SAXS} and T_{peak}^{SAXS} are, respectively, the onset temperature for polymer crystallization and the temperature corresponding to the maximum scattered intensity. $T_{onset ps}^{SAXS}$ is the onset temperature for DMDBS phase separation, and $T_{plateau}^{SAXS}$ is the temperature at which the intensity reaches a constant value (above T_c).

	T_c^{SAXS} [°C]	T_{peak}^{SAXS} [°C]	$T_{onset ps}^{SAXS}$ [°C]	$T_{plateau}^{SAXS}$ [°C]
HD120MO	120	108		
0.3% DMDBS – B03	135	125	165	150
0.7% DMDBS – B03	135	125	190	175
1% DMDBS – B1	135	127	195	185

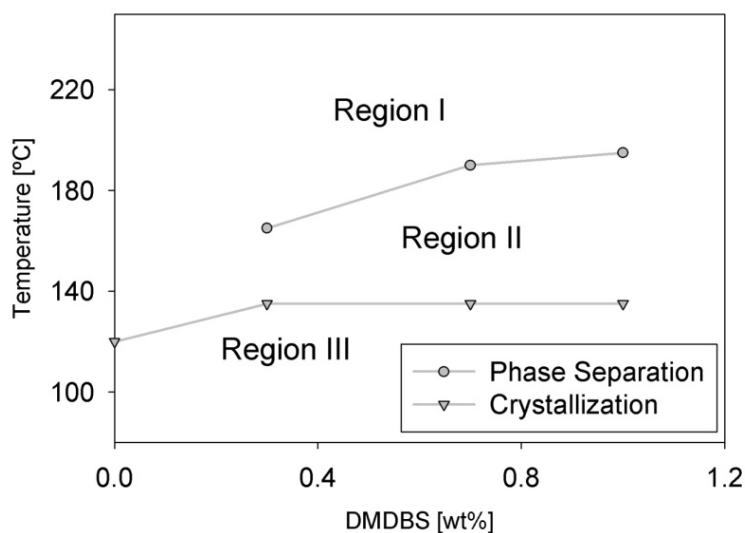


Figure 2.9: Phase diagram of the system iPP-DMDBS (from 0 to 1 wt% DMDBS) obtained, on cooling, using SAXS data. Three regions corresponding to three different states can be identified: Region I) homogeneous liquid, Region II) phase separated system with crystallized DMDBS and molten polymer, Region III) both iPP and DMDBS are crystallized

When the polymer crystallizes, in Region III, SAXS allows for the measure of the long period. Figure 2.10 shows the data concerning the neat polymer, B03, B07 and B1 as a function of temperature. As already discussed, the presence of DMDBS leads to an increase in L_p .

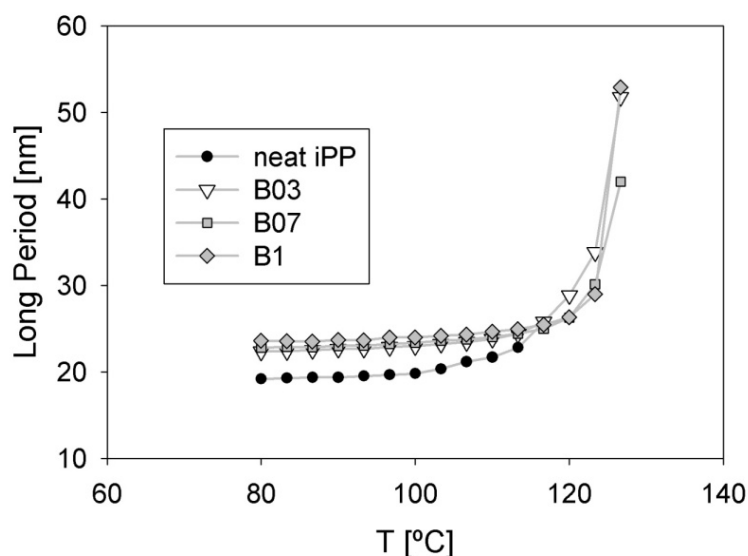


Figure 2.10: Long period as a function of temperature and DMDBS concentration during temperature ramps with cooling rate of 10 °C/min. Presence of DMDBS leads to an increase of the long periods that below 80 °C is quantified in ~4 nm

2.3.3 Morphology of the system in Region II

Two dimensional SAXS images reveal that the increase of the integrated intensity in Region II is caused by an increase of the scattering in all azimuthal directions at low q . Sample images are shown in Figure 2.11.

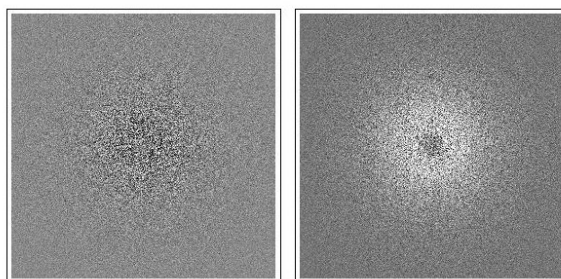


Figure 2.11: SAXS images of the blend B1. Left: material in Region I of the phase diagram and Right: material in Region II of the phase diagram. DMDBS phase separation causes an increase of the scattered intensity in all directions at low q values. For a clear visualization, the scattering of the system in Region I was subtracted.

Such a scattering pattern can be ascribed to the formation of a suspension of randomly oriented DMDBS fibrillar crystals with a length L and a radius R . In this case, the intensity scattered in the q region $2\pi / L < q < 1 / R_c$, can be described with²⁵⁻²⁷:

$$I(q) = \frac{C}{q} \text{Exp} \left(-\frac{R_c^2 q^2}{2} \right) \quad (2.3)$$

where C is a constant including details on the scatterers like concentration and electron density, while R_c is the radius of gyration of the cross section of the scatterers ($R_c = R / \sqrt{2}$). From the existing literature, it is known that DMDBS fibrils are basically endless ($L \rightarrow \infty$), therefore Equation (2.3) is valid for $q < 1/R_c$ in this case. Within this limit, $\text{Log}[I(q) \cdot q]$ versus q^2 is a straight line with a slope $-R_c^2 / 2$. Fitting Equation (2.3) to the data points allows for the calculation of R_c and therefore of R . Figure 2.12 provides an example of such a fit demonstrating that a good agreement between experimental data and Equation (2.3) exists for $0.15 < q < 0.3 \text{ nm}^{-1}$ (i.e. for $0.025 < q^2 < 0.1 \text{ nm}^{-2}$).

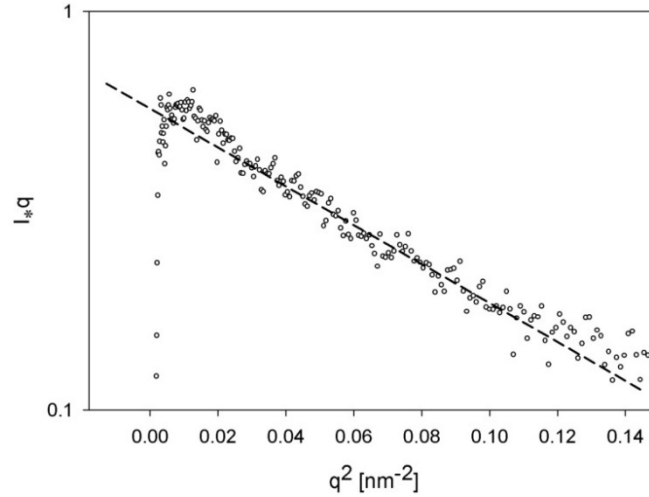


Figure 2.12: SAXS data points with a fit (dashed line) of Equation (2.3) for the blend B1 in Region II. For endless fibrils, Equation (2.3) holds in the limits: $q < 1 / R_c$. The experimental data deviate from the dashed line at $q^2 \cong 0.1 \text{ nm}^{-2}$, consistent with fibrils having a radius of 4.5 nm. At very low q , the agreement between Equation (2.3) and the data ceases at $q^2 = 0.025 \text{ nm}^{-2}$. This could be the fingerprint of bundles of elementary DMDBS fibrils.

This observation is consistent with presence of fibrillar scatterers with a radius of ~ 4.5 nm and a length that exceeds the experimental accessible SAXS range ($L > 200$ nm). As shown in Figure 2.13, the radius of DMDBS fibrils is independent of DMDBS concentration.

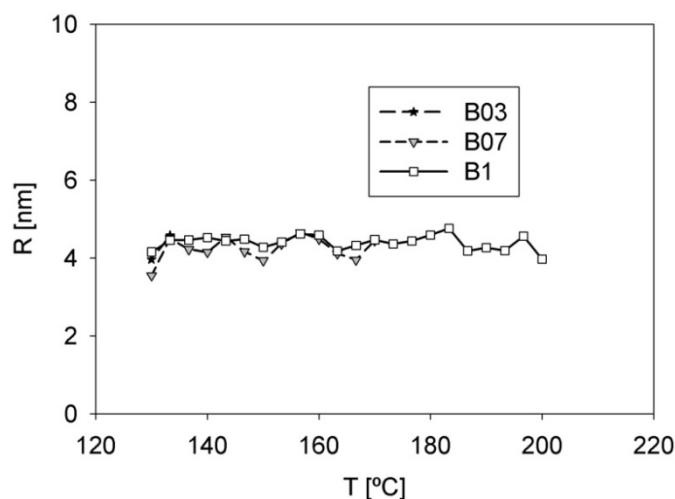


Figure 2.13: Radius of DMDBS fibrils as a function of temperature and DMDBS concentration. The data are obtained fitting Equation (2.3) on the experimental data. For B07 and B1 phase separation starts at higher temperature than B03, therefore more data points are available in these two cases.

This result is in agreement with the findings of Thierry et al.⁹ and Shepard et al.¹² that observed elementary (DBS) fibrils with a radius of ~ 5 nm. It is also reported that elementary fibrils of DBS and DMDBS can form bundles with a radius of ~ 50 nm at concentrations as low as 0.1 wt%^{12, 28}. The population of bundles becomes larger increasing the additive content. From our SAXS experimental range, it is difficult to infer bundles formation; however, this could be the source of discrepancies observed between experimental data points and Equation (2.3) in the low q range. For instance, in Figure 2.12, the agreement between data points and Equation (2.3) ceases at $q^2 = 0.025 \text{ nm}^{-2}$ (i.e. at $q = 0.15 \text{ nm}^{-1}$). The measured intensity is higher than what is predicted by Equation (2.3), suggesting also the presence of thicker scatterers. For instance, if another linear region with a steeper slope could be identified at lower q values, this could indicate the presence of scatterers characterized by a radius $R = \sqrt{2}/0.15 = 9.5 \text{ nm}$, i.e. bundles made of 2 elementary DMDBS fibrils. Unfortunately, with our experimental limits, this aspect is difficult to assess. The detection of larger bundles of elementary DMDBS fibrils is even more difficult because the limit $q < 1/R_c$ proceeds rapidly towards too low values when the radius of the scatterers grows.

2.3.4 Rheology of the system in Region II

Phase separation of DMDBS has a strong influence on the rheology of the system. Relaxation times and moduli increase because of network formation. One way to determine the temperature where this change happens is to measure the storage modulus (G') at constant frequency during cooling from Region I. The data are shown in Figure 2.14.

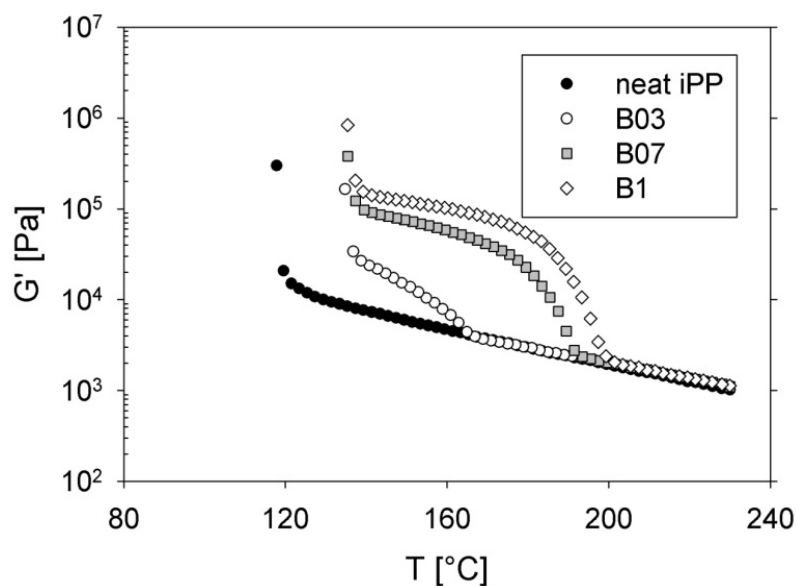


Figure 2.14: Storage modulus ($\omega=5$ rad/s) as a function of temperature for the neat iPP and the blends B03, B07 and B1. Data points are recorded on cooling (rate 10 °C/min) after annealing in Region I. The neat iPP shows a thermo-rheological simple (Arrhenius) behavior in all the temperature range preceding the steep increase of G' because of nucleation. In the blends containing DMDBS, the thermo-rheological simple behavior is also observed at high temperatures (Region I). However, the transition to Region II leads to a more complex behavior with an extra increase of G' corresponding to the phase separation of DMDBS. This increase is ascribed to the growth of DMDBS fibrils with network formation. After completion of phase separation, the Arrhenius behavior is restored until the polymer nucleates in Region III. In Region II, higher DMDBS contents relate to larger increases in G' suggesting the formation of a denser network of fibrils.

As expected, for the neat iPP, G' is only affected by the change in temperature. This implies linear (Arrhenius) behavior on a logarithmic scale²². At lower temperatures, when nucleation sets in, an abrupt upturn is observed. In contrast, G' of samples containing DMDBS exhibits a more complex temperature dependence. When DMDBS starts phase separating, G' raises quickly because of the growth of DMDBS fibrils and deviates from the

linear behavior. After completion of the phase separation and before nucleation of the polymer, the linear dependence is restored. With increasing DMDBS concentration the raise in G' becomes more pronounced because of the formation of a denser network that, in addition, includes more multiple fibril strands that are stiffer than the elementary fibrils. In line with DSC and SAXS, nucleation is observed at similar temperatures for samples containing DMDBS (~ 138 °C), while, the neat iPP nucleates at a lower temperature (~ 120 °C). The changes in the rheology with DMDBS phase separation are not fully described using only one frequency. Therefore, in Figure 2.15 the frequency dependent mechanical response of the neat iPP is compared with that of the blend B07, at 188 °C, after phase separation.

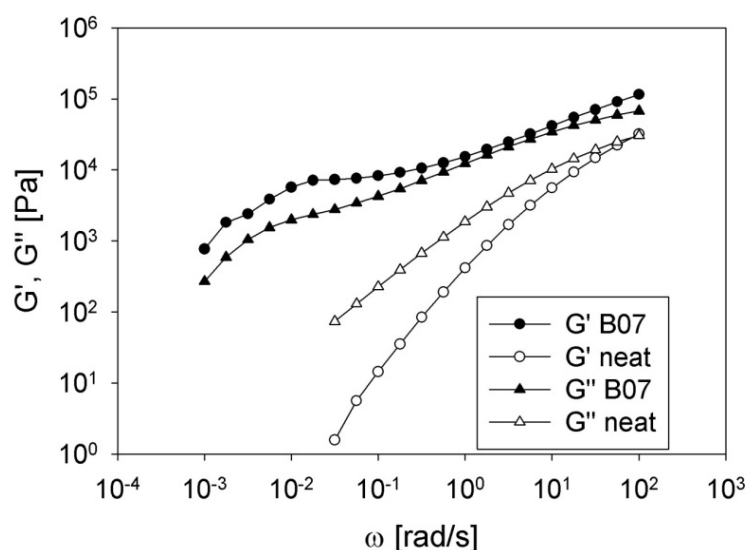


Figure 2.15: Storage and loss moduli (G' and G'') as a function of frequency at 188 °C for the neat iPP and B07 (annealed for 30 min). Both G' and G'' are higher in B07 than in the neat polymer. The formation of a percolated network of fibrils is responsible for the plateau in G' observed at low frequencies in B07. The physical nature of the network is unveiled by the viscous-like behavior visible in the lowest frequency range. This network contributes to slow down the relaxation times of the system.

Clearly, the transition from a melt to a suspension of DMDBS fibrils alters the values of both storage and loss modulus of iPP over at least five decades of frequencies. The phase separated system exhibits a G' higher than G'' in the entire experimental frequency window. Moreover, from ~ 1 to ~ 10 rad/s, G' and G'' display a power law dependence on the frequency (linear trend in a double logarithmic plot)^{29, 30} that, according to some authors, is the fingerprint of a fractal structure. Furthermore, in the phase separated system, G' shows a

plateau in the low frequency region that is associated with the formation of a percolated network³¹ of DMDBS fibrils. The combination of the rheological features described above is typically associated to a gel beyond the critical gel stage^{29, 32}. The viscous like response observed in the lowest frequency region highlights the physical nature of this gel. DMDBS fibrils are in contact but are not permanently (chemically) bonded and, for this reason, they can still slide over each other at very long experimental times. As a result, DMDBS network of fibrils slows down the relaxation of the melt with the introduction of new, long, relaxation modes.

2.3.5 Effect of flow on iPP-DMDBS blends near the gel transition

DMDBS phase separation changes the rheology of the system making relaxation slower. Therefore, we envisage that this transition influences the flow behavior of the system. In order to study the influence of shear flow on DMDBS network of fibrils, the blend B1 was selected. According to rheology, the onset of phase separation for this blend, in quiescent conditions, is at 195 °C. Interestingly, we found that, even at 210 °C, application of a strong shear flow of 60 s⁻¹ for 3 s causes immediate phase separation of the additive. In other words, shear enhances phase separation of DMDBS shifting the onset 15 °C above its ‘quiescent’ value. Rheological data concerning this flow induced phase separation are presented in Figure 2.16. Though the phase separation starts at higher temperatures with shear, the increase in the storage modulus is approximately the same as in the quiescent case. Furthermore, at the applied cooling rate (10 °C/min), the nucleation temperature of the polymer is not affected by shear. When the same shear is applied after formation of a network of DMDBS fibrils, at 188 °C for instance, the scenario is different. Here, as shown in Figure 2.17, flow causes a drop in the storage modulus, larger than one decade, that does not heal during cooling. The physical nature of DMDBS network is the cause of this drop. In fact, during shear, the fibrils are forced to slide over each other and tend to align parallel to the flow direction. As a consequence, the network breaks and the elastic modulus drops. Alignment of DMDBS fibrils causes a strong and anisotropic density fluctuation along the flow direction as depicted in Figure 2.18. This density fluctuation results in a streak of intensity in the equatorial region of SAXS images. In these circumstances, time resolved SAXS is a valuable technique also for studying the relaxation times of the fibrils.

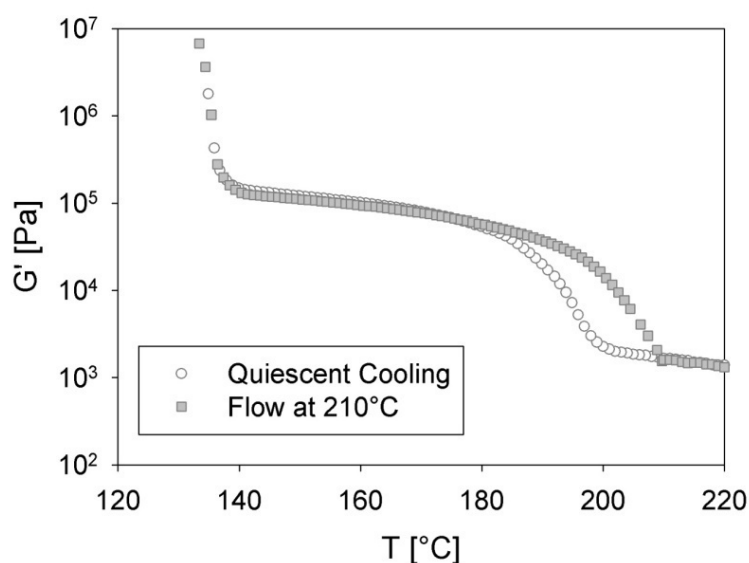


Figure 2.16: Temperature dependence for G' ($\omega=5$ rad/s) of the blend B1 with and without the application of a shear flow (60 s $^{-1}$ for 3 s) at 210 °C, in Region I of the phase diagram. Clearly, shear flow has the effect of enhancing the phase separation of the additive that, in this case, starts immediately after shearing. Nevertheless, after completion of the phase separation, the observed increase of G' is very close to the quiescent case. At lower temperatures, nucleation of the polymer occurs, unaffected by flow, at 138 °C.

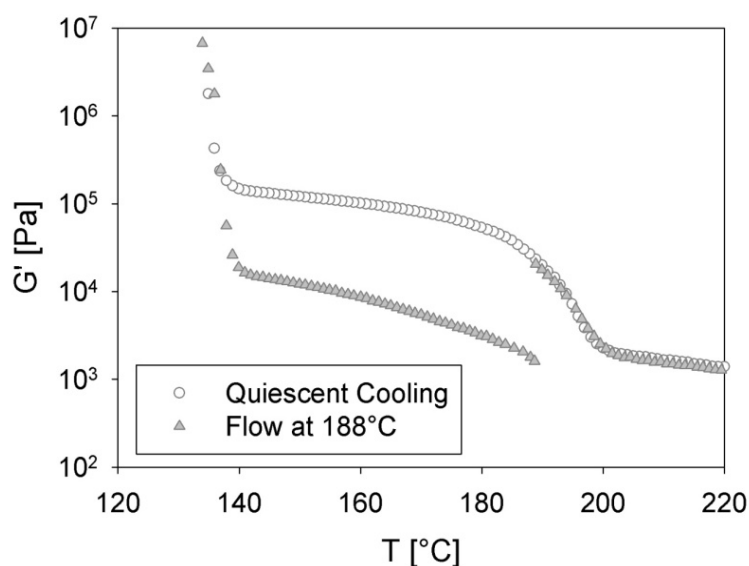


Figure 2.17: Temperature dependence for G' ($\omega=5$ rad/s) of the blend B1 with and without the application of a shear flow (60 s $^{-1}$ for 3 s) at 188 °C in Region II of the phase diagram, after DMDBS phase separation. Shear causes a large drop in G' that is not recovered even at lower temperatures. This drop can be explained with disconnection of the fibrillar network and alignment of the fibrils in the flow direction. Shear flow does not affect the nucleation of the polymer at lower temperatures.

As shown in Figure 2.19, the streak of intensity and therefore the alignment of the fibrils is retained without significant changes over the whole experimental time (>2000 s). On the time scales characterizing the use of these materials in processing, the alignment of DMDBS fibrils can be considered as permanent.

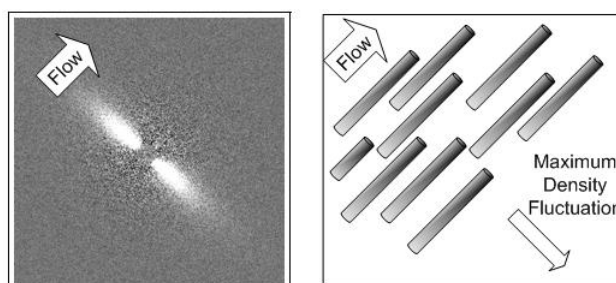


Figure 2.18: (Left) SAXS image showing a streak of intensity in the equatorial region. The image refers to the sample B1 after application of shear at 188 °C, in Region II. (Right) Schematic representation of DMDBS fibrils aligned parallel the flow direction. An arrow indicates the direction corresponding to the maximum density fluctuation. This direction is orthogonal to the shear direction and parallel to the equatorial streak in the SAXS pattern.

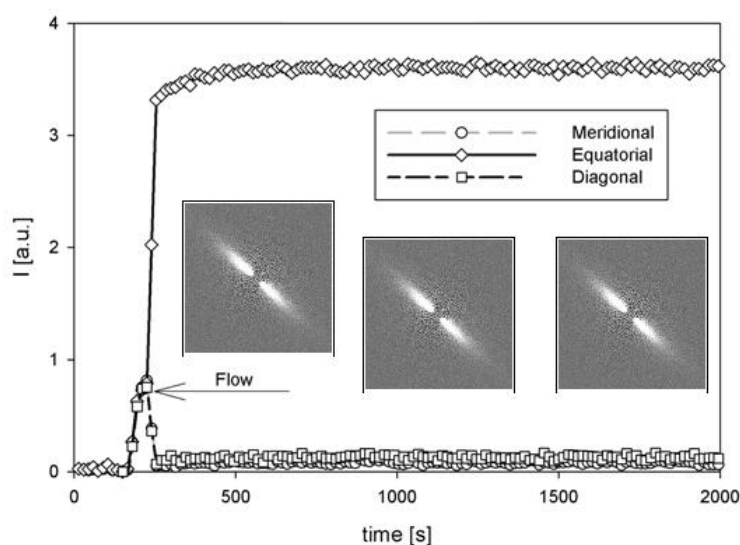


Figure 2.19: Time dependence of meridional, equatorial and diagonal intensity of the blend B1 at 188 °C after application of shear flow (60 s^{-1} for 3 s). When phase separation takes place, around 100 s, the scattered intensity, as expected, rises evenly in all directions. Therefore meridional, equatorial and diagonal intensities rise evenly. However, after application of shear flow, a streak of intensity appears in the equatorial region and, therefore, the intensity scattered in this region increases while it decreases in the meridional and diagonal regions. This situation arises due to alignment of DMDBS fibrils. The different intensity levels are retained for times longer than the experimental time without any significant changes. Inserted figures show SAXS images corresponding to increasing times.

2.3.6 Morphological implications of flow and DMDBS phase separation on the crystallization of iPP

In Section 2.3.2 the ability of DMDBS in nucleating iPP is described. Because of a favorable lattice matching, the energy barrier for heterogeneous nucleation on the surface of DMDBS fibrils is lower than the energy barrier for homogeneous nucleation. Therefore, most of the polymer ‘prefers’ to nucleate on the DMDBS fibrils.

In Section 2.3.5, the effect of shear on the network of DMDBS fibrils is described. For the blend B1, we found that a shear flow of 60 s^{-1} for 3 s, applied at a temperature a few degrees above the transition to Region II can enhance the phase separation of the additive. In contrast, if the same shear is applied a few degrees below the transition to Region II, the fibrils align parallel to the flow and the network is broken. Similar results are also obtained for the blends B03 and B07. The flow induced morphology of iPP-DMDBS blends arises from a combination of the physics described in Section 2.3.2 and Section 2.3.5.

The study of flow induced crystallization in iPP-DMDBS blends was carried out combining SAXS and a short term shear protocol. The short term shear protocol (with a shear of 60 s^{-1} for 3 s) was applied to the neat iPP and to the blends B03, B07 and B1 before and after phase separation of the additive. Afterwards, the polymer was allowed to crystallize by cooling to room temperature.

The effects of flow in Region I (prior to the crystallization of DMDBS) were tested by applying shear to B03 at 185 °C, to B07 at 195 °C and to B1 at 210 °C. Independent of the DMDBS concentration, shear in Region I can only enhance phase separation. Upon cooling, DMDBS fibrils form randomly oriented in space and the polymer, crystallizing on top of a randomly oriented substrate, displays an isotropic morphology. The morphologies obtained in these cases are similar to the crystallization in quiescent conditions.

In contrast, shear in Region II (after crystallization of DMDBS) aligns DMDBS fibrils parallel to the flow direction. By design, the lateral growth of polymer lamellae occurs orthogonally to the fibril axis. Therefore, once the fibrils are aligned, iPP lamellae grow in the direction orthogonal to the applied flow. With this templating mechanism, in the early stages of crystallization the orientation of the substrate is transformed into orientation of polymer lamellae. Shearing B03 at 150 °C, B07 at 178 °C and B1 at 180 °C yields oriented polymer morphologies after cooling below T_c .

In principle, the anisotropic polymer morphology, observed after applying shear in Region II, could also be ascribed to orientation of the polymer at these lower temperatures. To exclude this possibility, we benchmark the morphology by crystallizing the neat iPP after application of shear at 150 °C. This temperature is the lowest used for iPP-DMDBS blends and therefore the most favorable for obtaining an anisotropic morphology. In spite of that, after cooling below T_c , the neat polymer crystallizes with an isotropic pattern.

A visual summary of the performed experiments, including SAXS images at room temperature is given in Figure 2.20.

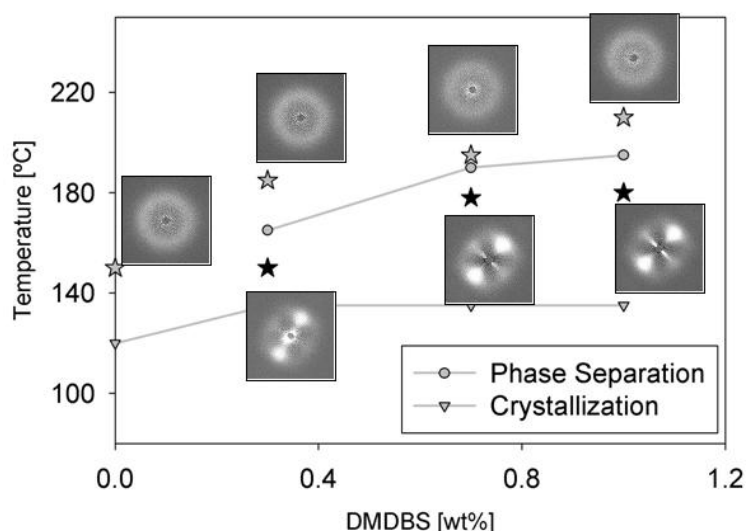


Figure 2.20: Phase diagram of iPP-DMDBS (from 0 to 1 wt% DMDBS) including SAXS images describing the morphology, at room temperature, after application of ‘short term shear’ protocol with shear temperatures indicated by the symbols (stars). When shear flow is applied above DMDBS phase separation (in Region I), isotropic polymer morphologies are obtained. In contrast, shear flow applied below DMDBS phase separation (in Region II) yields polymer morphologies with a high degree of anisotropy.

SAXS images of the polymer crystallized after application of shear in Region II show a clear separation of the intensities scattered in different azimuthal regions that corresponds to a high degree of lamellar orientation. The intensity scattered by oriented crystallites is $I_{or} = I_{Eq} + I_{Mer}$ where I_{Eq} and I_{Mer} are, respectively, the intensity scattered in the equatorial and meridional regions. An assessment of the degree of orientation of polymer lamellae, Φ , can be obtained by combining the intensities scattered in the different azimuthal regions: $\Phi = (I_{Eq} + I_{Mer}) / I_{Tot}$ where I_{Tot} is the total scattered intensity³³. The scattering in

the equatorial region contains a contribution from the oriented DMDBS fibrils, I_{DMDBS} . Therefore, a better definition for the degree of orientation of polymer lamellae is¹⁷:

$$\Phi = \frac{(I_{Eq} + I_{Mer}) - I_{DMDBS}}{I_{Tot} - I_{DMDBS}} \quad (2.4)$$

I_{DMDBS} is taken as the value assumed by the equatorial intensity immediately before the crystallization of the polymer. The values of Φ , calculated at room temperature after application of shear in Region II, increase with DMDBS concentration and range from 0.4 of B03 to 0.6 of B1, see Figure 2.21.

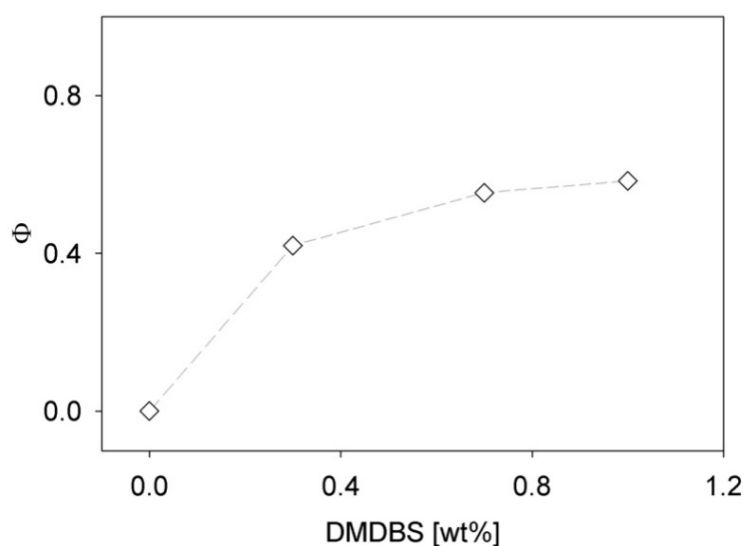


Figure 2.21: Orientation factor calculated with Equation (2.4) reference goes here⁴ as a function of DMDBS content measured at room temperature after the application of shear in Region II. The neat iPP showed no orientation therefore the corresponding value is set to 0. Samples containing DMDBS show increasingly high values of orientation.

Similar values were reported by Nogales et al.¹⁷ for experiments with a similar protocol carried out on a propylene/ethylene copolymer containing less than 1 wt% of DBS.

2.4 Conclusions

We studied the phase behavior of the binary system iPP-DMDBS for concentration of the additive ranging from 0 to 1 wt%. The results are in agreement with the monotectic model

already reported. When DMDBS phase separates, we addressed the formation of a percolated network of fibrils and the effects that this network has on the crystallization of the polymer. SAXS patterns are consistent with formation of DMDBS fibrils with a radius of ~ 4.5 nm and a length exceeding the experimental range ($L > 200$ nm). It is known that the surface of these fibrils hosts a large number of nucleation sites for iPP and, because of a favorable epitaxy matching, iPP molecules tend to nucleate on this substrate. The epitaxial relationship between iPP and DMDBS is such that polymer lamellae always grow in the radial direction starting from the surface of the fibrils. DMDBS assists nucleation of iPP reducing the energy barrier and, as a consequence, the crystallization temperature of the polymer raises as much as 19 °C. The growth of DMDBS fibrils within the molten iPP matrix gives rise to a physical network that changes the rheology of the system introducing long relaxation times. This change becomes more pronounced at higher DMDBS concentration and, as expected, affects the flow induced crystallization.

When no flow is applied, DMDBS fibrils form with a random orientation in space and, therefore, iPP lamellae grow following the same isotropic pattern. When flow is applied two situations are discussed:

1) If flow is applied before DMDBS phase separates, then the fibrils form in absence of strain and adopt the ordinary random orientation in space. For this reason, crystallization of iPP occurs with an isotropic morphology.

2) If flow is applied after DMDBS phase separation, the imposed deformation drives DMDBS fibrils parallel to the flow direction. When iPP nucleates, lamellae grow as usual with the *c* axis parallel to the fibrils axis, and therefore parallel to the flow direction. Oriented shish kebab morphologies are generated where the core is made of DMDBS and the kebabs of iPP. Polymer morphologies characterized by a high degree of anisotropy are obtained even though, in some cases, flow is applied well above the melting point of the polymer, i.e. in absence of undercooling.

Summarizing, we show that, when iPP nucleates, lamellar orientation is determined by the orientation of the DMDBS fibrils. This peculiarity can be used to template (assisted by epitaxy matching) the orientation of polymer lamellae. The phase separation of DMDBS can be seen as a switching mechanism for obtaining highly oriented iPP morphologies after application of flow at high temperatures. In summary, we conclude that when DMDBS is

present, thermo-mechanical history has a marked effect on iPP morphology. A critical condition exists for the transition from isotropic to oriented morphology: phase separation of DMDBS. The location of this critical condition in the phase diagram is set by the amount of DMDBS in the blend.

Phase separation/crystallization of DMDBS in iPP is thermoreversible. For this reason, the thermal history plays an important role. This is the subject of the following Chapter.

2.5 References

1. Schrauwen, B. A. G.; Breemen, L. C. A. v.; Spoelstra, A. B.; Govaert, L. E.; Peters, G. W. M.; Meijer, H. E. H. *Macromolecules* **2004**, 37, 8618-8633.
2. Kristiansen, M.; Tervoort, T.; Smith, P.; Goossens, H. *Macromolecules* **2005**, 38, 10461-10465.
3. Binsbergen, F. L. *Nature* **1966**, 211, 516-517.
4. Devaux, N.; Monasse, B.; Haudin, J. M.; Moldenaers, P.; Vermant, J. *Rheol. Acta* **2004**, 43, 210-222.
5. Kobayashi, T.; Hashimoto, T. *Bull. Chem. Soc. Jpn.* **2005**, 78, 218-235.
6. Blomehofer, M.; Ganzleben, S.; Hanft, D.; Schmidt, H. W.; Kristiansen, M.; Smith, P.; Stoll, K.; Mader, D.; Hoffmann, K. *Macromolecules* **2005**, 38, 3688-3695.
7. Zhu, P. W.; Edward, G. *Macromol. Mater. Eng.* **2003**, 288, 301-311.
8. Zhu, P. W.; Tung, J.; Edward, G. *Polymer* **2005**, 46, 10960-10969.
9. Thierry, A.; Fillon, B.; Straupe, C.; Lotz, B.; Wittmann, J. C. *Progr. Colloid Polym. Sci.* **1992**, 87, (31), 28-31.
10. Kristiansen, M.; Werner, M.; Tervoort, T.; Smith, P.; Blomehofer, M.; Schmidt, H. W. *Macromolecules* **2003**, (36), 5150-5156.
11. Fillon, B.; Lotz, B.; Thierry, A.; Wittmann, J. C. *Journal of Polymer Science: Part B: Polymer Physics* **1993**, 31, 1395-1405.
12. Shepard, T. A.; Delsorbo, C. R.; Louth, R. M.; Walborn, J. L.; Norman, D. A.; Harvey, N. G.; Spontak, R. J. *Journal of Polymer Science: Part B: Polymer Physics* **1997**, 35, 2617-2628.
13. Marco, C.; Ellis, G.; Gomez, M. A.; Arribas, J. M. *Journal of Applied Polymer Science* **2002**, 84, 2440-2450.
14. Nagarajan, K.; Levon, K.; Merson, A. S. *Journal of Thermal Analysis and Calorimetry* **2000**, 59, 497-508.
15. Dumitraş, M.; Friedrich, C. *J. Rheol.* **2004**, 48, (5), 1135-1146.
16. Fahrlander, M.; Fuchs, K.; Friedrich, C. *J. Rheol.* **2000**, 44, (5), 1103-1119.
17. Nogales, A.; Mitchell, G. R. *Polymer* **2005**, 46, 5615-5620.
18. Nogales, A.; Mitchell, G. R.; Vaughan, A. S. *Macromolecules* **2003**, 36, 4898-4906.
19. Somani, R. H.; Yang, L.; Hsiao, B. S.; Agarwal, P. K.; Fruitwala, H. A.; Tsou, A. H. *Macromolecules* **2002**, 35, 9096-9104.
20. Hindeleh, A. M.; Johnson, D. J. *J. Phys. D: Appl. Phys.* **1971**, 4, 259-263.

21. Wang, Z. G.; Hsiao, B. S.; Sirota, E. B.; Srinivas, S. *Polymer* **2000**, 41, 8825-8832.
22. Macosko, C., *Rheology : principles, measurements, and applications*. VCH: Weinheim, **1994**.
23. Pogodina, N. V.; Winter, H. H.; Srinivas, S. *Journal of Polymer Science: Part B: Polymer Physics* **1999**, 37, 3512-3519.
24. Wunderlich, B. *Macromolecular Physics*; Academic Press; New York **1980**.
25. Guinier, A.; Fournet, G. *Small-angle scattering of x-rays*; Chapman & Hall, London, **1955**.
26. Chen, E.; Weng, X.; Zhang, A.; Mann, I.; Harris, F. W.; Cheng, S. Z. D.; Stein, R.; Hsiao, B. S.; Yeh, F. *Macromol. Rapid. Commun.* **2001**, 22, 611-615.
27. Glatter, O.; Kratky, O. *Small Angle X-ray Scattering*; Academic Press **1982**.
28. Lipp, J.; Shuster, M.; Terry, A. E.; Cohen, Y. *Langmuir* **2006**, 22, (14), 6398 -640.
29. Winter, H. H.; Mours, M. *Advances in Polymer Science* **1997**, 134, 165-234.
30. Takenaka, M.; Kobayashi, T.; Saijo, K.; Tanaka, H.; Iwase, N.; Hashimoto, T.; Takahashi, M. *J. Chem. Phys.* **2004**, 121, (7), 3323-3328.
31. Coppola, S.; Acierno, S.; Grizzuti, N.; Vlassopoulos, D. *Macromolecules* **2006**, 39, 1507-1514.
32. Mours, M.; Winter, H. H. *Macromolecules* **1996**, 29, 7221-7229.
33. Somani, R. H.; Hsiao, B. S.; Nogales, A.; Srinivas, S.; Tsou, A. H.; Sics, I.; Balta-Calleja, F. J.; Ezquerro, T. A. *Macromolecules* **2000**, 33, 9385-9394.

Chapter 3*

Thermo-reversible DMDBS phase separation in iPP: effects on flow induced crystallization

The crystallization rate of isotactic polypropylene (iPP) is often enhanced with sorbitol-based nucleating agents like 1,3:2,4-bis(3,4-dimethylbenzylidene)sorbitol or DMDBS. In the concentration range from the eutectic point (~0.1 wt%) to 1 wt%, DMDBS crystallizes before the polymer and forms a network of fibrils. The surface of this network hosts a large number of tailored nucleation sites that favor the epitaxial nucleation of iPP. The formation of fibrils is a thermo-reversible liquid-solid phase separation occurring, on cooling, at a temperature T_{DMDBS}^c that depends on the composition. The melting point of DMDBS fibrils, T_{DMDBS}^m , depends also on the composition and is typically ~25 °C higher than T_{DMDBS}^c . We show that in the temperature window $T_{DMDBS}^c < T < T_{DMDBS}^m$ a percolated network of DMDBS fibrils is retained and that a shear flow causes alignment of the fibrils. At these high temperatures, iPP cannot crystallize. However, upon cooling, in the early stages of nucleation, the orientation of the fibrils (nucleating substrate) is transferred to the lamellae because of the epitaxial relation between iPP and DMDBS. With this templating mechanism, we obtained well oriented crystalline morphologies of iPP after a shear pulse (shear rate of 60 s^{-1} applied for 3 s) at 185 °C for 0.3 wt%, at 195 °C for 0.7 wt% and at 210 °C for 1 wt% of DMDBS.

3.1 Introduction

As stated in the previous Chapters, the crystallization rate of isotactic polypropylene (iPP) is often enhanced with nucleating agents¹⁻³. During heterogeneous nucleation, iPP nucleates at sites present on the surface of the nucleating particles. Therefore, particles with a high surface to volume ratio (S/V) are beneficial for nucleation. However, this is not the only requirement. Successful nucleating agents for iPP have a crystalline structure and lattice parameters that match those of the polymer (epitaxy matching). This was suggested by Binsbergen⁴ and later demonstrated by Lotz and coworkers⁵⁻⁷. A wide range of substances

* Partially reproduced from: Balzano L., et al. 'Thermo-reversible DMDBS phase separation in iPP: effects on flow induced crystallization', *Macromolecules* **2008** (Submitted)

that fulfill these requirements are used as nucleating agents for iPP. Examples are salts of aromatic carboxylic acids (for instance sodium benzoate)^{8, 9}, salts of phosphate esters (for instance NA-11)¹⁰ and sorbitol derivatives¹¹. The salts are insoluble in the polymer and, therefore, S/V is fixed by the particle shape. Moreover, their dispersion is limited by the high viscosity of the matrix. In contrast, sorbitol derivatives dissolve in the polymer melt and the (crystalline) nucleating particles are formed by phase separation, due to crystallization, upon cooling. Dissolution and re-crystallization provide a high degree of dispersion for these additives with a specific surface as high as 400m²/g¹². In this Chapter, we discuss some aspects of flow induced crystallization of iPP in presence of 1,3:2,4-bis(3,4-dimethylbenzylidene)sorbitol or DMDBS (formula shown in Figure 1.3), the latest of the family of sorbitol based nucleating agents. DMDBS is known to be a good clarifying agent for iPP at low concentrations, typically between ~0.1 wt% and ~1 wt%. This concentration range is the most interesting for applications and is considered for our investigation. In the previous Chapter, it was already discussed that the phase diagram is divided in three regions (see Figure 2.2). At high temperatures, iPP and DMDBS form a homogeneous solution (Region I). Upon cooling, DMDBS crystallizes and thus phase separates from the system (Region II) at a temperature T_{DMDBS}^C that depends on the composition. At lower temperatures, iPP also crystallizes (Region III). In the previous Chapter, it is also discussed that, the crystalline morphology of the polymer in Region III depends strongly on thermo-mechanical history. Crystallization after application of flow in Region I yields isotropic morphologies, similar to quiescent crystallization. In contrast, crystallization following application of flow in Region II yields highly oriented morphologies. The reason for this behavior lies in the fibrillar morphology of the crystallized DMDBS. Crystallization of these small molecules, driven by hydrogen bonding¹³⁻¹⁶, leads to a percolated network of nano-fibrils¹⁷ that alters the relaxation/flow behavior of the melt. A shear pulse can disconnect this network and induce a long lasting alignment of the fibrils. The result is an anisotropic distribution of the nucleation sites that has influence on the morphology of the polymer. In fact, for structural reasons, iPP lamellae always grow radially to DMDBS fibrils^{5, 18, 19}. Hence, if the fibrils are pre-aligned, the lateral growth of the lamellae occurs along one main direction (orthogonal to the common direction of the fibrils) and orientation is transferred from the nucleating particles to the polymer. This templating mechanism allows for creating oriented polymer morphologies

after deformations at high temperatures. Well oriented iPP morphologies were obtained (cooling to room temperature) after application of flow in Region II, at 150 °C for 0.3 wt% of DMDBS, at 178 °C for 0.7 wt% of DMDBS and at 188 °C for 1 wt% of DMDBS. So far, it seems that such a templating mechanism, based on the orientation of DMDBS fibrils, can work only for $T < T_{\text{DMDBS}}^{\text{c}}$. In the present Chapter, we show that its efficacy can be extended also in a temperature window above $T_{\text{DMDBS}}^{\text{c}}$, by making use of the thermoreversibility of DMDBS phase separation. It is well known that phase separation (crystallization) of DMDBS and network formation are thermoreversible^{11, 12, 20-22}. Upon heating, DMDBS fibrils melt and the network disappears. However, this occurs at a temperature, $T_{\text{DMDBS}}^{\text{m}}$, that is significantly higher than $T_{\text{DMDBS}}^{\text{c}}$. In other words, during heating, DMDBS fibrils are retained in a temperature window above $T_{\text{DMDBS}}^{\text{c}}$. We expect that application of flow in this temperature window has an influence on the final iPP morphology similar to flow application in Region II (i.e. that flow yields highly oriented iPP morphologies). Though it could be relevant for applications, the effect of flow at these high temperatures on iPP morphology, subject of the present Chapter, is unexplored so far.

3.2 Experimental method

3.2.1 Materials

The iPP used in this work is a commercial homopolymer grade from Borealis GmbH (Linz, Austria), labeled HD120MO, with molecular weight, M_w , of 365 kg/mol and a polydispersity, M_w/M_n , of 5.4. DMDBS (Millad 3988) was obtained in powder form from Milliken Chemicals (Gent, Belgium) and used as received.

3.2.2 Sample Preparation

The polymer, available in pellets, was ground below the glass transition temperature and then blended with DMDBS in a co-rotating twin screw mini-mixer (DSM, Geleen). The two compounds were allowed to mix for 10 minutes in a nitrogen rich atmosphere, at temperatures ranging from 230 to 250 °C (the higher the DMDBS concentration the higher

the compounding temperature). The material obtained was compression molded with a hot press into films of different thicknesses: 1mm for rheology and 200 μm for X-ray experiments. The molding temperature was 220 $^{\circ}\text{C}$ and the molding time was 3 min. The resulting films were quenched (~ 100 $^{\circ}\text{C}/\text{min}$) to room temperature and finally cut in disk-like samples. Following the same procedure, three blends of iPP with 0.3, 0.7 and 1 wt% of DMDBS were prepared. For convenience, these three blends are named B03, B07 and B1 respectively.

3.2.3 X-Ray Characterization

Small Angle X-ray Scattering (SAXS) was performed at beamline BM26/DUBBLE of the European Synchrotron Radiation Facility (ESRF) in Grenoble (France). Time resolved images were recorded on a two dimensional gas filled detector (512x512 pixels and 260 μm *260 μm pixel size) placed at approximately 6m from the sample. The wavelength adopted was $\lambda=1.24$ \AA . Scattering and absorption from air were minimized by a vacuum chamber placed between sample and detector. SAXS images were acquired with an exposure time of 5 s and corrected for the intensity of the primary beam, absorption and sample thickness. The scattered intensity was integrated and plotted against the scattering vector, $q = (4\pi / \lambda)\sin(\vartheta / 2)$ where ϑ is half of the scattering angle. The long period was calculated as $L_p = 2\pi / (q_{I_{MAX}})$, where $q_{I_{MAX}}$ is the q value corresponding to the maximum in the scattered intensity. Finally, an integrated intensity was defined as: $I_I = \int_{q_{\min}}^{q_{\max}} I(q) dq$ where q_{\min} and q_{\max} are the minimum and the maximum experimentally accessible q values respectively. Two dimensional SAXS images were also used for the characterization of anisotropic morphologies. For this purpose, it was necessary to define three azimuthal regions: 1. Meridional: corresponding to the flow direction in real space; 2. Equatorial: orthogonal to the meridional region; 3. Diagonal: connecting the equatorial and meridional regions in the azimuthal direction.

Shear flow experiments in combination with SAXS were carried out using a Linkam Shear Cell (CSS-450) modified with Kapton windows. To ensure reproducibility, prior to the

experiments, samples were always annealed at 230 °C for 3 min to erase the memory of any previous thermo-mechanical treatment.

3.2.4 Rheological Characterization

Rheological measurements were performed in the linear viscoelastic regime using a strain-controlled AR-G2 rotational rheometer (TA Instruments). In all cases a plate-plate geometry with a diameter of 8 mm was used. Appropriate values of strain were determined with amplitude sweep tests carried out at 5 rad/s over a broad range of strains (ranging from 0.01 to 100 %). During the study of phase transitions, large strains can enhance the process and/or affect the morphology. Therefore, these experiments are carried out with strains as low as 0.5 %.

3.2.5 DSC

The thermal effects of DMDBS phase separation was studied in quiescent conditions using Dynamic Scanning Calorimetry (DSC). Samples of approximately 2mg were placed into aluminum pans and tested in a nitrogen atmosphere using a Q1000 calorimeter (TA Instruments). The first step in the thermal treatment was always annealing at 230 °C for 3 min to erase earlier thermo-mechanical histories. To study re-crystallization and melting of DMDBS within the iPP matrix samples were cooled to 140 °C and then immediately heated back to 230 °C. Both cooling and heating rate were set to 10 °C /min. Before analyzing the peaks, a linear baseline was subtracted from the raw data as a function of the temperature.

3.3 Results and discussion

3.3.1 Thermoreversibility in the phase diagram

iPP-DMDBS mixtures, for compositions up to 1 wt%, show a monotectic phase diagram, on heating and on cooling, that can be divided in three regions as shown in Figure 2.2 and Figure 2.9. The phase diagrams on heating and on cooling are qualitatively similar, but the differences in the crystallization and melting temperatures of both iPP (T_{iPP}^c and T_{iPP}^m)

and DMDBS ($T_{\text{DMDBS}}^{\text{c}}$ and $T_{\text{DMDBS}}^{\text{m}}$) make them quantitatively different. The characteristic temperatures $T_{\text{DMDBS}}^{\text{c}}$, $T_{\text{iPP}}^{\text{c}}$, $T_{\text{iPP}}^{\text{m}}$ and $T_{\text{DMDBS}}^{\text{m}}$ depend on DMDBS concentration and more generally also on the thermal history of the system. In the following, we discard the study of the dependence on heating and cooling rates by fixing them both at 10 °C/min. Information to sketch the phase diagrams, on heating and on cooling, can be obtained with DSC and/or rheology. However, the study of flow effects on morphology, objective of this work, requires the use of SAXS and this technique can equally provide information to build the phase diagrams. Figure 3.1 illustrates SAXS intensity as a function of the temperature, on heating and on cooling, for the neat iPP and the three blends with DMDBS.

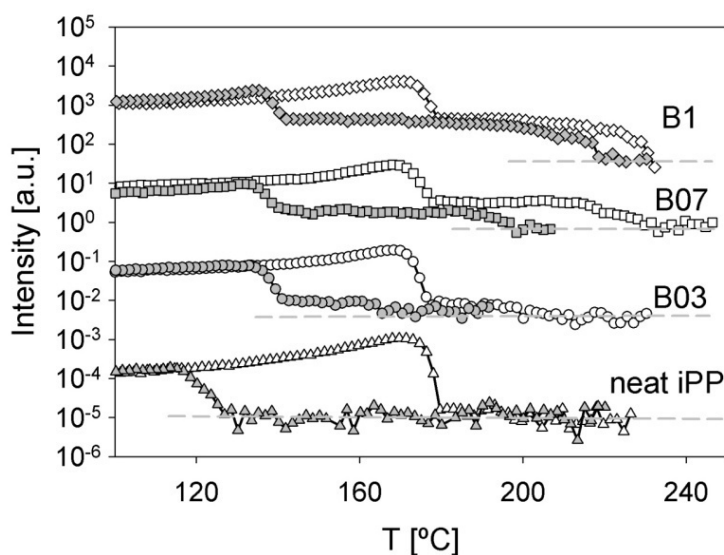


Figure 3.1: Integrated SAXS intensity as a function of the temperature during cooling (gray symbols) and during heating (white symbols) for the neat iPP, B03, B07 and B1. For visibility, curves are shifted in the vertical direction and reference (dashed) lines are added.

During cooling from Region I (filled symbols), the onset of crystallization of DMDBS is indicated by an increase in the scattered intensity. At a lower temperature, $T_{\text{DMDBS}}^{\text{c}}$, the scattered intensity approaches a plateau that indicates the completion of DMDBS phase separation. Next, at $T_{\text{iPP}}^{\text{c}}$, another, larger intensity raise indicates the nucleation of iPP. During heating from Region III (open symbols), iPP lamellae start melting at $T_{\text{iPP}}^{\text{m}}$, the density fluctuations reduce and the SAXS intensity drops. Nevertheless, the presence of DMDBS crystals keeps the intensity above the reference value that is approached only when DMDBS melts at $T_{\text{DMDBS}}^{\text{m}}$. In agreement with data already available in literature^{2, 12}, the characteristic

temperatures for the crystallization and melting of DMDBS in the iPP matrix, $T_{\text{DMDBS}}^{\text{c}}$ and $T_{\text{DMDBS}}^{\text{m}}$, show a strong dependence on the composition. In contrast, for the polymer, the crystallization (onset) temperature, $T_{\text{iPP}}^{\text{c}}$, is 127 °C for the non-nucleated case and 142°C for all blends while the melting temperature (completion), $T_{\text{iPP}}^{\text{m}}$, is 170 °C independent of composition. The phase diagrams, summarizing the transitions on heating and on cooling as a function of DMDBS concentration and temperature, are shown in Figure 3.2.

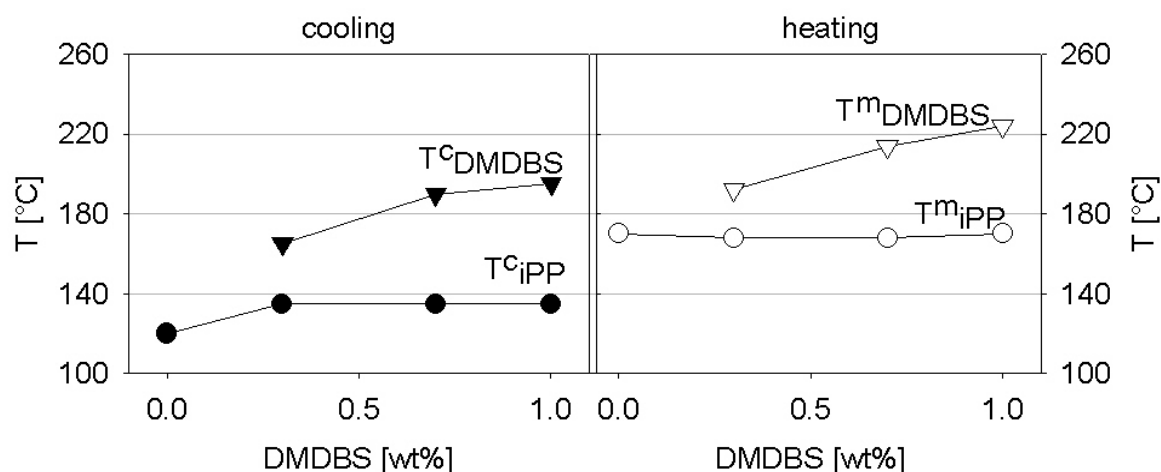


Figure 3.2: *iPP-DMDBS* phase diagrams obtained with SAXS on cooling (left) and on heating (right).

The difference between $T_{\text{DMDBS}}^{\text{c}}$ and $T_{\text{DMDBS}}^{\text{m}}$ is in the order of 25 °C. Although only small amounts of DMDBS (1 wt% is the highest) are used, the thermal effects associated to its phase separation and dissolution in the iPP matrix can also be resolved with DSC. The thermograms are reported in Figure 3.3. The shift of $T_{\text{DMDBS}}^{\text{c}}$ and $T_{\text{DMDBS}}^{\text{m}}$ with the composition is consistent with SAXS data and, as expected, a greater latent heat is measured at larger DMDBS contents (see also Table 3.1).

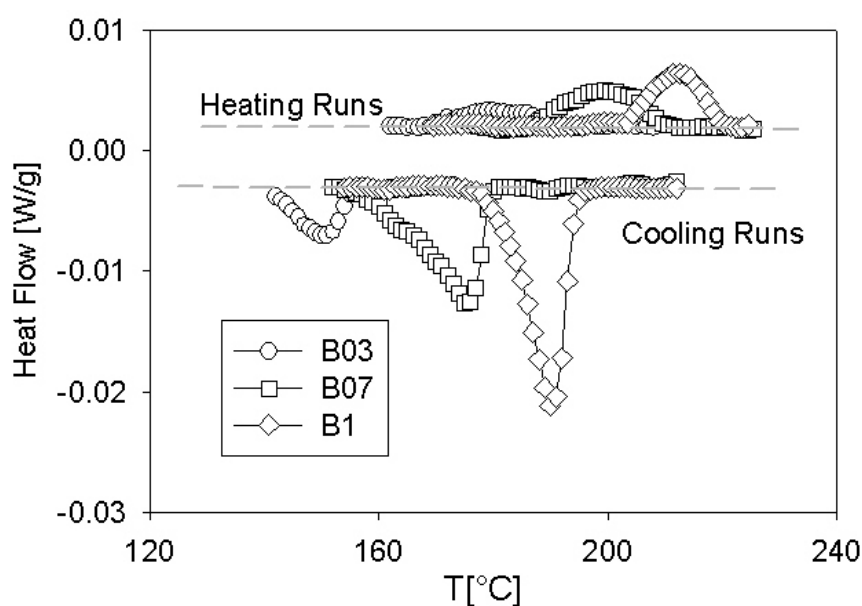


Figure 3.3: Thermal effects associated to the crystallization (phase separation) and melting (dissolution) of DMDBS within the iPP matrix. Higher DMDBS content correspond to larger thermal effects and higher transition temperatures. A summary of the relevant information is provided in Table 3.1.

Table 3.1: Calorimetric (DSC) data regarding DMDBS within an iPP matrix obtained analyzing the thermograms of Figure 3.3

	T_{DMDBS}^c [°C]	ΔH_c [J·g ⁻¹]	T_{DMDBS}^m [°C]	ΔH_m [J·g ⁻¹]
0.3 wt%	149	-0.14	179	0.017
0.7 wt%	175	-0.10	198.5	0.043
1 wt%	189	-0.045	212	0.046

The phase behavior of the system appears complicated by ‘thermal memory effects’. When heating from Region II to Region I, there is a range of temperatures, at $T > T_{\text{DMDBS}}^c$, where DMDBS crystals are still present. For this reason, depending on the thermal history, a sub area of Region I can be identified where, on heating, the system is still phase separated (Region I-PS), see Figure 3.4.

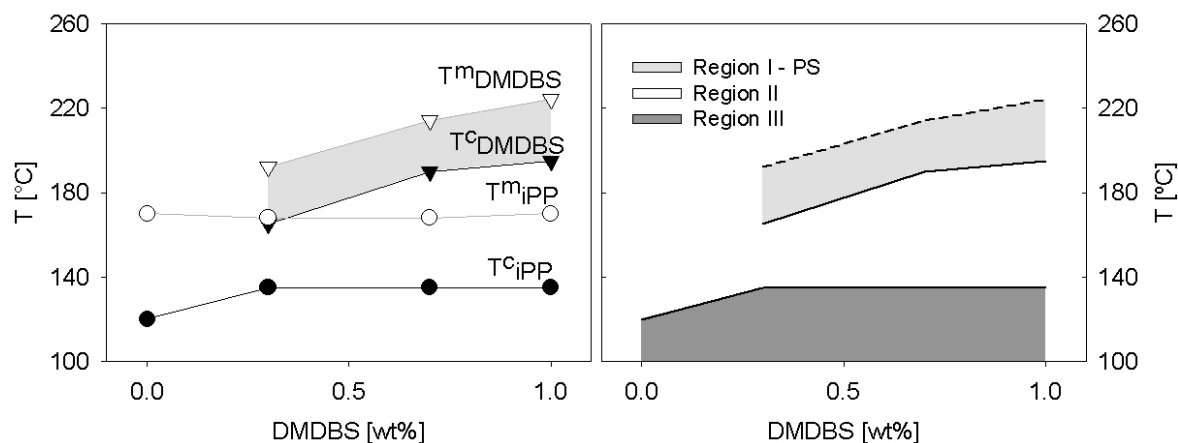


Figure 3.4: Left) Phase diagrams for iPP-DMDBS blends on heating and on cooling. Right) Phase diagram on cooling including Region I-PS. Note that Region I-PS is encountered only on heating from Region II.

The tridimensional network of DMDBS fibrils slows down the relaxation and this has a clear effect on the rheology of the system. This is shown in Figure 3.5 that reports the temperature dependence of the storage modulus (G') at 5 rad/s for B03, B07 and B01 during cooling from Region I to Region II (open symbols) and heating vice versa (filled systems).

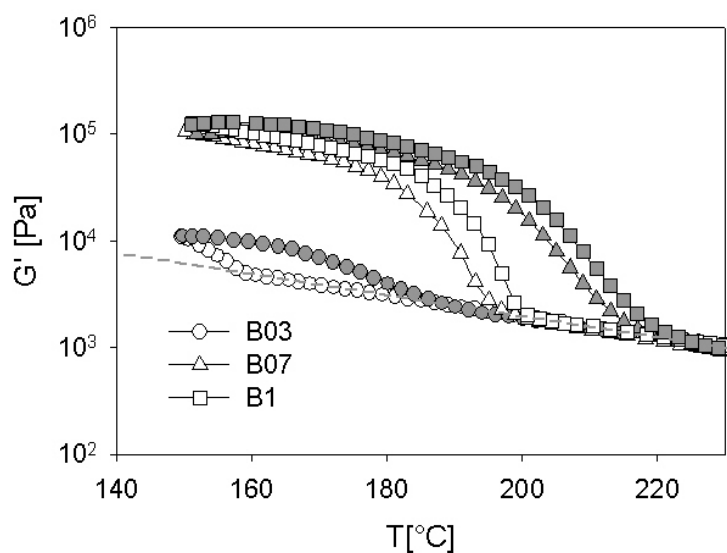


Figure 3.5: G' at 5rad/s as a function of the temperature on cooling (open symbols) and on heating (filled symbols) for B03, B07 and B1. Increasing the amount of DMDBS, both the crystallization and melting temperatures of the fibrils shift to higher values.

For the blends, during cooling, the storage modulus (G') increases rapidly when DMDBS phase separates, deviating from the linear behavior that is observed at high

temperatures. The mesh size of the DMDBS network is proportional to the concentration of DMDBS and, therefore, at higher DMDBS concentrations a larger increase in G' is found. In addition, increasing DMDBS concentration more network strands are made of bundles of elementary fibrils and this increases the stiffness of the network. During heating, the fibrils melt at a temperature higher than they form on cooling. When approaching this temperature, the contribution of the fibrils to the elastic modulus gradually vanishes. At high enough temperatures, the linear dependence of G' with temperature is restored meaning that, in line with SAXS and DSC, an homogeneous solution is attained.

Here, we discuss the use of SAXS, DSC and rheology to capture the changes associated with the phase separation and melting of DMDBS in iPP. These techniques probe different aspects and, therefore, a different sensibility is expected. To make a comparison, a degree of transformation ϕ can be defined per each technique. For SAXS:

$$\Phi_{SAXS}(T) = \frac{I(T) - I_{HT}^0}{I_{LT}^0 - I_{HT}^0} \quad (3.1)$$

I_{HT}^0 is the intensity at high temperature (in absence of scatterers) and I_{LT}^0 is the plateau intensity observed after completion of DMDBS phase separation and before the onset of iPP crystallization. For DSC:

$$\Phi_{DSC}(T) = \frac{\int_{T_s}^T W(\xi) d\xi}{\int_{T_s}^{T_e} W(\xi) d\xi} \quad (3.2)$$

where W is the heat flow, T_s and T_e are, respectively, a temperature before the onset and after the completion of DMDBS phase separation (before crystallization of the polymer). For rheology:

$$\Phi_{Rheo}(T) = \frac{G'(T) - G'_{HT}(T)}{G'_{LT}(T) - G'_{HT}(T)} \quad (3.3)$$

where $G'_{HT}(T)$ is a function, linear on a linear-log plot, obtained extrapolating the high temperature linear behavior of G' to low temperatures. $G'_{LT}(T)$ is similar as $G'_{HT}(T)$ and extrapolates at high temperatures the low temperatures linear behavior exhibited by G' (before the nucleation of iPP). The definitions of ϕ are also shown in Figure 3.6.

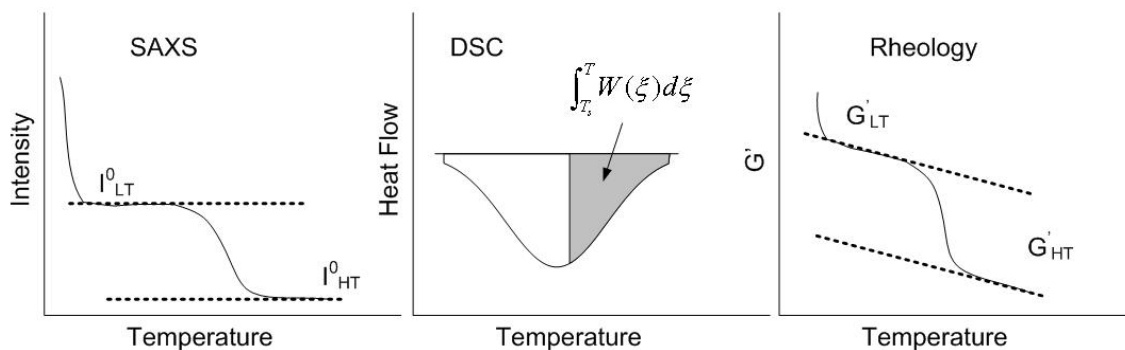


Figure 3.6: Definitions of the degree of transformation during DMDBS crystallization according to SAXS, DSC and Rheology. The symbols are defined in the text.

With these definitions, $\phi = 0$ means that there is no phase separation, while $\phi = 1$ means that the phase separation is complete. The degrees of transformation for B1, during DMDBS phase separation, are shown in Figure 3.7.

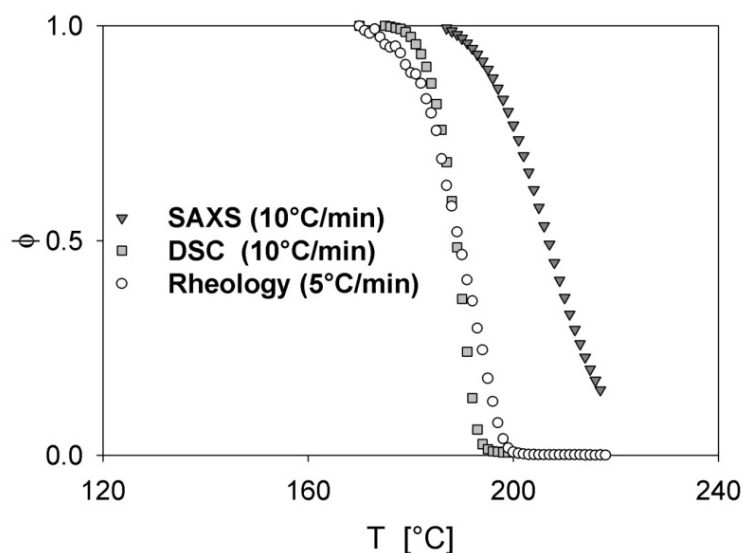


Figure 3.7: Changes in the degree of transformation for SAXS, DSC and Rheology for the blend B1 on cooling. The degrees of transformations are defined by Equations 1, 2 and 3.

At 10 °C/min, the onset of DMDBS phase separation is detected in SAXS at a temperature much higher than in DSC ($T_{\text{onset}}^{\text{SAXS}} \cong 218$ °C while $T_{\text{onset}}^{\text{DSC}} \cong 195$ °C). Thermal effects are detectable only when, according to SAXS, the phase separation is nearly complete (see also Figure 3.8).

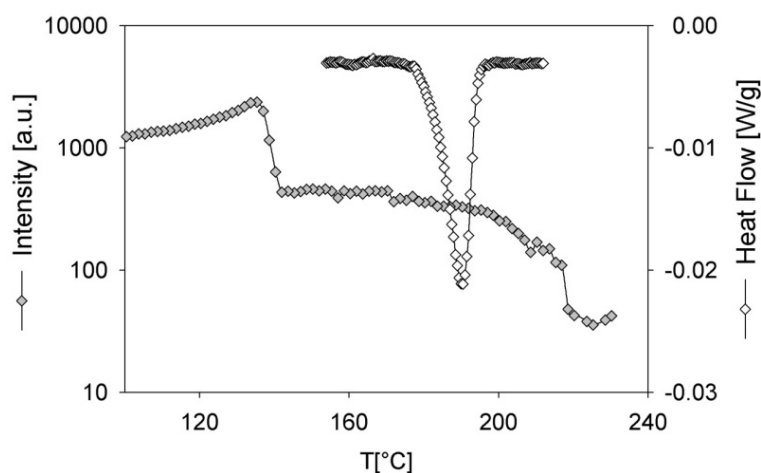


Figure 3.8: A comparison of SAXS and DSC during DMDBS phase separation for the blend B1 on cooling.

To assure a proper temperature control, rheology could only be performed with a cooling rate of 5 °C/min. Figure 3.7 (and also Figure 3.5) shows that the sensitivity of this technique with respect to the DMDBS phase separation is similar to DSC ($T_{\text{onset}}^{\text{Rheo}} \cong 200$ °C). Similar results were observed also for the other blends B03 and B07. On heating, melting of DMDBS fibrils is detectable first by DSC and then at last by SAXS, when $\phi_{\text{DSC}}^{\text{melting}}$ is approaching to zero.

3.3.2 Linear viscoelasticity of the system in Region I-PS

Rheological data complements SAXS and DSC information, showing that the contribution of DMDBS fibrils to the relaxation behavior of the system persists in Region I-PS. As show in Figure 3.5, in this area of the phase diagram, DMDBS fibrils raise the elastic modulus several times. For instance, at 205°C, the ratio between G' on heating and G' on cooling is nearly one decade for B07 and B1. A thorough understanding of the rheology of the system requires the investigation of a broad spectrum of frequencies²³. To this end, Figure 3.9 shows the frequency dependent rheological behavior of B07 at 205°C, in Region I and in Region I-PS and that of the neat polymer at the same temperature.

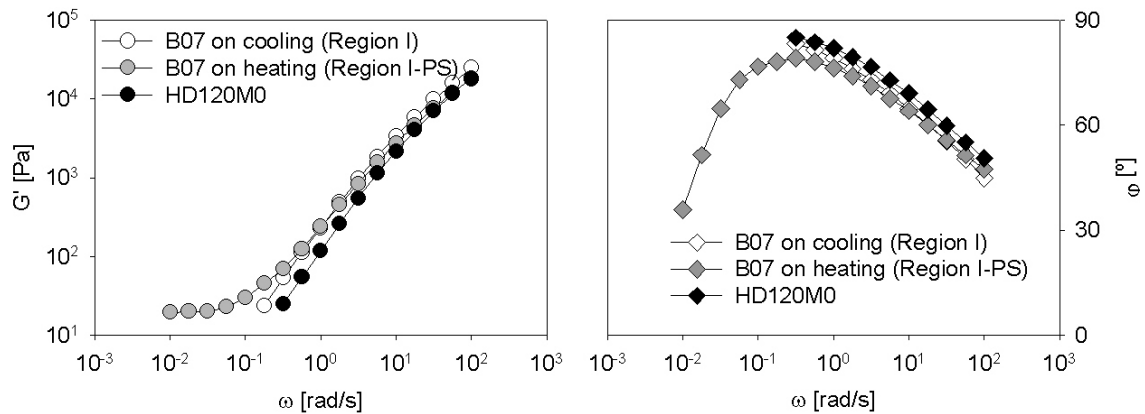


Figure 3.9: Left) G' as a function of frequency at 205 °C. The neat polymer is used as a reference to evaluate the changes in B07 measured at the same temperature but with two different thermal histories. In one case (whites symbols), B07 is measured after cooling from 230 °C (i.e. while it is in Region I). In the other case (gray symbols), the same blend is measured after being cooled to 150 °C, heated to 205 °C and annealed at this temperature for 30 min (i.e. while it is in stable conditions in Region I-PS). When in Region I-PS, a plateau appears in the low frequency range. This solid like behavior is the rheological fingerprint of the DMDBS fibrillar network in the polymer melt. Right) Phase angle as a function of the frequency. For B07 in Region I-PS a maximum appears signaling the crossover between viscous- and solid- like behaviors.

Some peculiarities are clearly visible. First of all, it is important to notice that, B07 is initially not in equilibrium at 205 °C and, during the first 10 min, a slow melting of the fibrils takes place causing a major drop in the rheological properties: G' at 5 rad/s drops from ~ 8000 Pa to ~ 1500 Pa and then stabilizes. Therefore, to ensure a stable system, the measurement was performed after an annealing of 30 min at 205 °C. Despite the partial melting of the fibrils taking place before the measurement, a plateau appears for $\omega < 0.1$ rad/s implying that part of the DMDBS network is still connected and contributes to the rheology with a solid-like behavior in the low frequency region. The transition between a viscous- and a solid- like behavior is marked by the maximum in the phase angle, ϕ , at ~ 0.3 rad/s.

3.3.3 Crystallization on cooling after flow in Region I-PS

As it was mentioned in the Introduction paragraph, the epitaxial relation between iPP and DMDBS causes the radial growth of lamellae on the fibrils. As a consequence, the crystalline morphology of iPP always reflects the orientation of the DMDBS fibrils. The top row of Figure 3.10 shows room temperature SAXS images of samples crystallized after a

shear pulse (60 s^{-1} for 3 s) at $185 \text{ }^\circ\text{C}$ for B03, at $195 \text{ }^\circ\text{C}$ for B07 and at $210 \text{ }^\circ\text{C}$ for B1, i.e. in Region I of the phase diagram. In all these cases, iPP exhibits an isotropic morphology similar to crystallization in quiescent conditions. In fact, DMDBS fibrils are not present at the moment of the shear; they form at a lower temperature and, without deformations, they grow with random orientations. In contrast, the bottom row of Figure 3.10 shows SAXS images at room temperature after to the application of a similar shear pulse (60 s^{-1} for 3 s) in Region II ($150 \text{ }^\circ\text{C}$ for B03, at $178 \text{ }^\circ\text{C}$ for B07 and $188 \text{ }^\circ\text{C}$ for B1). Here, iPP exhibits a highly oriented morphology. In fact, shear is applied after the DMDBS network is established and, so, induces alignment of the DMDBS fibrils. In the early stages of iPP crystallization, with epitaxial nucleation, the orientation of the fibrils is transferred to the polymer lamellae. Interestingly, the flow conditions in Region I, corresponding to the top row of Figure 3.10 ($185 \text{ }^\circ\text{C}$ for B03, $195 \text{ }^\circ\text{C}$ for B07 and $210 \text{ }^\circ\text{C}$ for B1), fall also within Region I-PS. Therefore, these flow conditions are taken as a crucial example to demonstrate the importance of thermal history in the crystallization of these materials after shear.

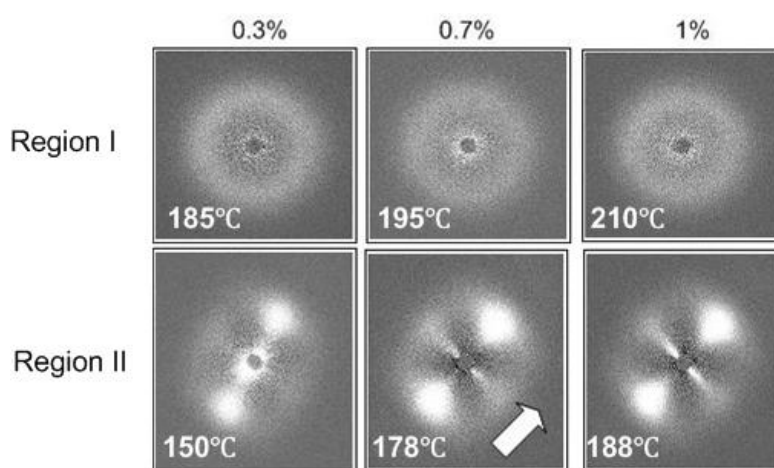


Figure 3.10: Two dimensional SAXS images recorded at room temperature for B03, B07 and B1 after the application of a shear (60 s^{-1} for 3 s) at the temperature indicated in the frame. The flow direction is indicated by the arrow. Shear in Region I (i.e. on a solution) yields isotropic iPP morphologies. Shear in Region II (i.e. on a phase separated system) aligns DMDBS fibrils setting the ground for the development of a well oriented polymer morphology.

In Section 3.3.1 it was shown that, despite the high temperature, DMDBS fibrils can still be present in Region I-PS. As a consequence, also in Region I-PS, the fibrils can be aligned with flow, setting the necessary conditions for an oriented polymer morphology. A suitable thermo-mechanical history to demonstrate this is shown in Figure 3.11.

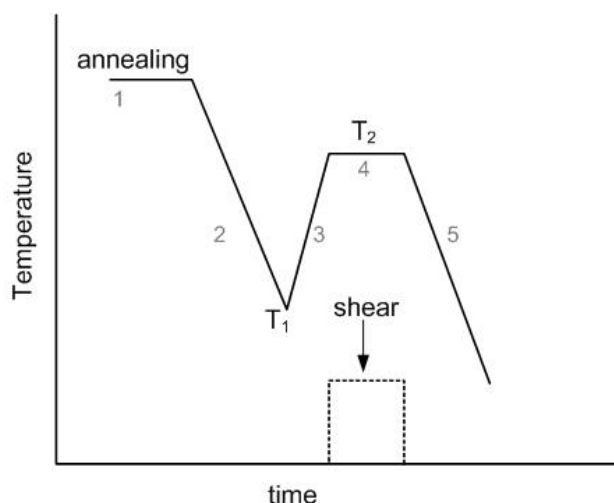


Figure 3.11: Schematic drawing of the thermal history designed to obtain oriented iPP morphologies after shear application at exceedingly high temperatures. A shear pulse (60 s^{-1} for 3 s) is applied during stage 4. The design values of T_1 and T_2 for B03, B07 and B1 are shown in Table 3.2.

It includes five steps: 1. annealing in Region I, 2. cooling at T_1 in Region II, 3. heating to T_2 in Region I-PS, 4. application of a shear pulse of 60 s^{-1} for 3 s and finally 5. cooling to room temperature. All samples are annealed in the same conditions (230 °C for 3 min) while the temperatures T_1 and T_2 are chosen depending on DMDBS concentration (see Table 3.2).

Table 3.2: Summary of the temperatures where shear is applied in the experiments of Figure 3.10 (flow in Region I and Region II) and of the choices made for the thermal history of Figure 3.11.

	Flow in Region I		Flow in Region II		Parameters for flow in Region I-PS	
	T [°C]	iPP morphology at room temperature	T [°C]	iPP morphology at room temperature	T_1 [°C]	T_2 [°C]
B03	185	isotropic	150	oriented	150	185
B07	195	isotropic	178	oriented	178	195
B1	210	isotropic	188	oriented	188	210

SAXS confirms that shearing iPP-DMDBS blends at T_2 induces the alignment of DMDBS fibrils and, ultimately, creates an oriented polymer morphology. This is illustrated in Figure 3.12 that displays SAXS intensity for the blend B1 experiencing the protocol of Figure 3.11.

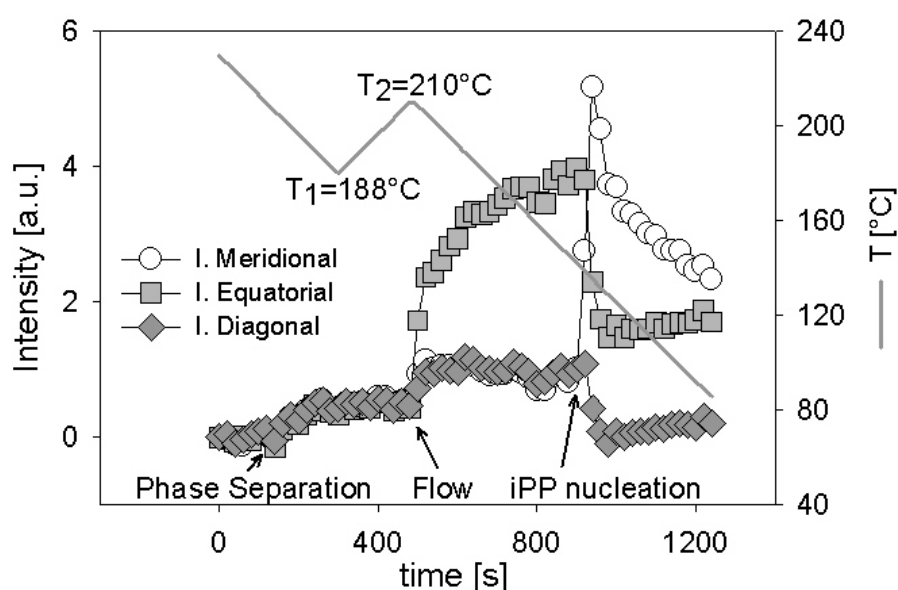


Figure 3.12: SAXS intensity for meridional, equatorial and diagonal part of the two dimensional images as a function of time and temperature for the blend B1 subjected to shear (60 s^{-1} for 3 s) at $210 \text{ }^\circ\text{C}$.

For B1, $T_{\text{DMDBS}}^c = 195 \text{ }^\circ\text{C}$. Therefore, cooling to $T_1=188 \text{ }^\circ\text{C}$ causes phase separation of DMDBS. As a consequence, the scattered intensity rises evenly in all the azimuthal areas. In the following step, heating to $T_2=210 \text{ }^\circ\text{C}$, the intensity remains constant (for B1 $T_{\text{DMDBS}}^m = 224 \text{ }^\circ\text{C}$) indicating that the fibrils do not melt. With a shear pulse (60 s^{-1} for 3 s) at this temperature, DMDBS fibrils align with flow and lead to an equatorial streak in the SAXS images (see Figure 3.13). The equatorial streak raises the intensity scattered at the equator I_{eq} . Simultaneously, also the intensities scattered in the meridional and diagonal regions (I_{mer} and I_{diag}) raise, suggesting that flow promotes an extra phase separation with growth of randomly oriented fibrils. However, according to the lever rule, complete DMDBS phase separation is not possible at this high temperature and proceeds during the following cooling. The increase in I_{eq} rather than in I_{mer} and I_{diag} indicates that the growth of flow-oriented fibrils is favored over the growth of randomly oriented fibrils. At $\sim 140 \text{ }^\circ\text{C}$, iPP nucleates and the growth of stack of lamellae perpendicular to DMDBS fibrils takes place producing lobes in the SAXS meridional region. Epitaxially grown lamellae mitigate the density fluctuation between DMDBS and the matrix, hence the intensity scattered in equatorial and diagonal regions decreases. As shown in Figure 3.13, this protocol yields an iPP morphology with a high degree of orientation despite the fact that flow was applied at a temperature as high as

210 °C. Similar results are also obtained when B03 and B07 are sheared in Region I-PS, at 185 and 195 °C respectively.

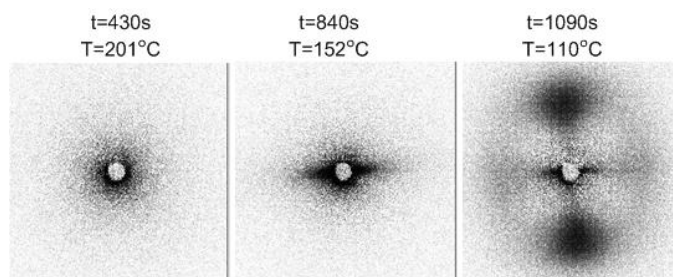


Figure 3.13: Time-temperature sequence of SAXS images for the blend B1 in the experiment illustrated in Figure 3.12. After shear application to the fibrillar network, the fibrils align and a streak of intensity appears at the equator. Crystallization of *i*PP at lower temperatures produces the meridional lobes. The flow direction is vertical

Figure 3.14 gives a summary of the SAXS images at room temperature for all the blends investigated, together with the location of the flow conditions in the phase diagram.

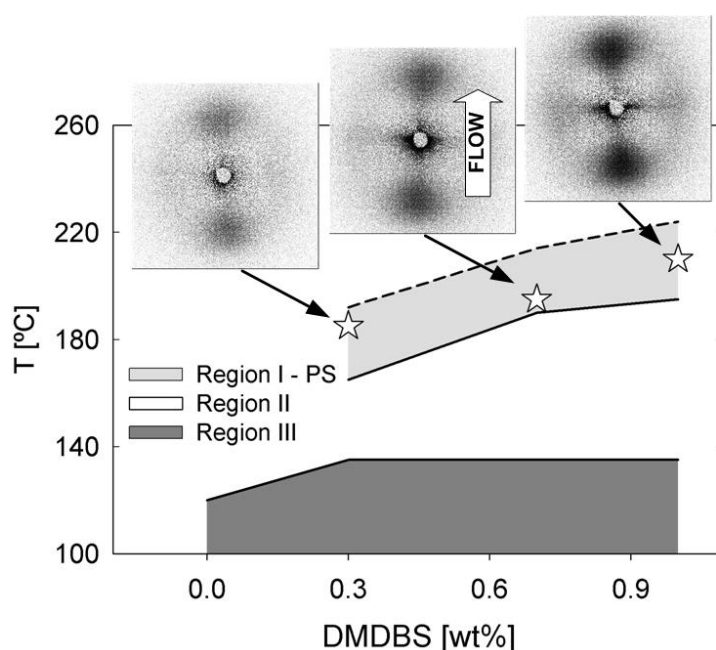


Figure 3.14: *i*PP-DMDBS phase diagram reporting the SAXS images corresponding to the room temperature morphology of *i*PP after application of shear (60 s^{-1} for 3 s) in the conditions indicated by the star-like symbols.

Additional information on the morphology of the polymer is given by the long periods displayed in Figure 3.15.

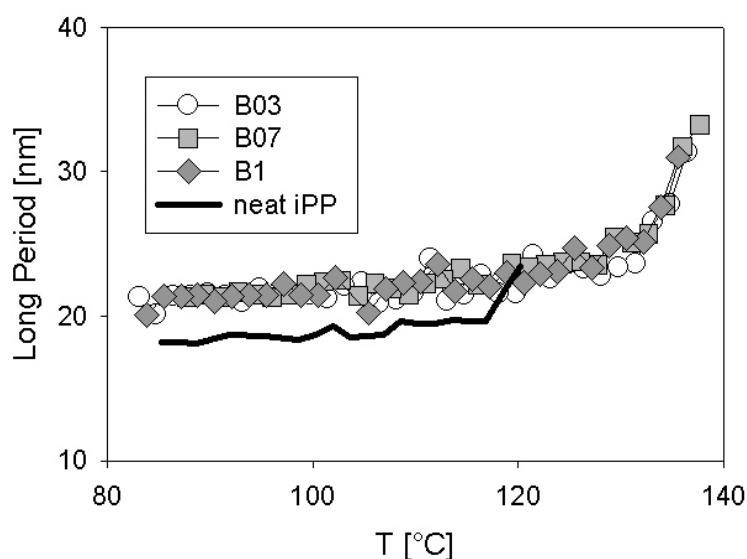


Figure 3.15: Long periods measured for B03, B07 and B1 in the final cooling of experiments where shear flow is applied in Region I-PS. Taking the neat polymer crystallized in quiescent conditions as a reference, an increase in the long period of ~ 4 nm is observed. Similar increase is reported for crystallization of the blends in quiescent conditions, suggesting that flow has no influence in the long period.

At low temperatures, iPP-DMDBS blends show a long period of ~ 22 nm that is 4 nm more than the value for quiescent crystallization of the neat polymer. Similar values are also obtained crystallizing the blends under quiescent conditions. This means that the long period is essentially governed by the presence of DMDBS and that the effect of flow is negligible. The higher long periods of the blends are due to the shift in the iPP crystallization temperature that leads to the formation of thicker crystals.

3.4 Conclusions

In Chapter 2, we demonstrated that, in iPP-DMDBS blends, oriented iPP morphologies can be obtained with a thermo-mechanical history based on two steps: 1) pre-alignment of DMDBS fibrils at high temperature with shear and 2) subsequent epitaxial crystallization of the polymer at low temperature. The first step (alignment of DMDBS fibrils) limited the application of this process at temperatures lower than the phase separation of the additive ($T < T_{\text{DMDBS}}^c$). In this Chapter, we proved that this limit can be exceeded. In fact, the thermo-reversibility of iPP-DMDBS phase separation can be used to obtain highly

oriented iPP morphology in combination with shear even at $T > T_{\text{DMDBS}}^{\text{c}}$. In fact, after the DMDBS network of fibrils is established with a cooling to a temperature below $T_{\text{DMDBS}}^{\text{c}}$, the system can be heated up (roughly) to $T_{\text{DMDBS}}^{\text{c}} + 25$ without consequences on the DMDBS network. Shearing the network (60 s^{-1} for 3 s) in this temperature window induces alignment of the DMDBS fibrils, similar to what observed at $T < T_{\text{DMDBS}}^{\text{c}}$. Next, upon cooling, in the early stages of crystallization, because of the epitaxial relation between iPP and DMDBS, the orientation is transferred from the fibrils to the polymer lamellae. In this way, we showed that from understanding the phase behavior of iPP-DMDBS blends, on cooling and on heating, it is possible to design thermo-mechanical histories that yield well oriented iPP morphologies after shear at very high temperatures (for instance $210 \text{ }^{\circ}\text{C}$ for 1 wt% of DMDBS). Interestingly, when small amount of DMDBS are present, flow can still govern the morphology of the polymer in a high temperature window where relaxation times are short.

In the Chapters 2 and 3, the nucleating/templating effects of DMDBS fibrils towards iPP lamellae is discussed. In the next Chapter, we show that nucleating fibrils with aspect ratio similar to DMDBS fibrils and perfect epitaxial matching can be generated *in situ* when flow is combined with an appropriate choice of the molecular weight distribution present in the melt.

3.5 References

1. Kristiansen, M.; Tervoort, T.; Smith, P.; Goossens, H. *Macromolecules* **2005**, *38*, 10461-10465.
2. Kristiansen, M.; Werner, M.; Tervoort, T.; Smith, P.; Blomehofer, M.; Schmidt, H. W. *Macromolecules* **2003**, (36), 5150-5156.
3. Gahleitner, M.; Wolfschwenger, J.; Bachner, C.; Bernreitner, K.; Neißl, W. *Journal of Applied Polymer Science* **1996**, *61*, 649-657.
4. Binsbergen, F. L. *Polymer* **1970**, *11*, (5), 253-267.
5. Thierry, A.; Fillon, B.; Straupe, C.; Lotz, B.; Wittmann, J. C. *Progr. Colloid Polym. Sci.* **1992**, *87*, (31), 28-31.
6. Fillon, B.; Lotz, B.; Thierry, A.; Wittmann, J. C. *Journal of Polymer Science: Part B: Polymer Physics* **1993**, *31*, 1395-1405.
7. Alcazar, D.; Ruan, J.; Thierry, A.; Lotz, B. *Macromolecules* **2006**, *39*, 2832-2840.
8. Zhu, P. W.; Tung, J.; Edward, G. *Polymer* **2005**, *46*, 10960-10969.
9. Beck, H. N. *Journal of Applied Polymer Science* **1967**, *11*, (5), 673 - 685.
10. Marco, C.; Ellis, G.; Gomez, M. A.; Arribas, J. M. *Journal of Applied Polymer Science* **2002**, *84*, 1669-1679.

11. Marco, C.; Ellis, G.; Gomez, M. A.; Arribas, J. M. *Journal of Applied Polymer Science* **2002**, 84, 2440-2450.
12. Shepard, T. A.; Delsorbo, C. R.; Louth, R. M.; Walborn, J. L.; Norman, D. A.; Harvey, N. G.; Spontak, R. J. *Journal of Polymer Science: Part B: Polymer Physics* **1997**, 35, 2617-2628.
13. Wilder, E. A.; Spontak, R. J.; Hall, C. K. *Molecular Physics* **2003**, 101, (19), 3017-3027.
14. Kobayashi, T.; Hashimoto, T. *Bull. Chem. Soc. Jpn.* **2005**, 78, 218-235.
15. Thierry, A.; Straupe, C.; J.; W.; Lotz, B. *Macromol Symp* **2006**, 241, 103-110.
16. Takenaka, M.; Kobayashi, T.; Saijo, K.; Tanaka, H.; Iwase, N.; Hashimoto, T.; Takahashi, M. *J. Chem. Phys.* **2004**, 121, (7), 3323-3328.
17. Lipp, J.; Shuster, M.; Terry, A. E.; Cohen, Y. *Langmuir* **2006**, 22, (14), 6398 -640.
18. Nogales, A.; Olley, R. H.; Mitchell, G. R. *Macromol Rapid Comm* **2003**, 24, (8), 496-502.
19. Nogales, A.; Mitchell, G. R.; Vaughan, A. S. *Macromolecules* **2003**, 36, 4898-4906.
20. Smith, J. M.; Katsoulis, D. E. *Journal of material chemistry* **1995**, 5, (11), 1899-1903.
21. Fahrlander, M.; Fuchs, K.; Friederich, C. *Journal of Rheology* **2000**, 44, (5), 1103-1119.
22. Fräßdorf, W.; Fahrländer, M.; Fuchs, K.; Friedrich, C. *Journal of Rheology* **2003**, 47, (6), 1445-1454.
23. Dumitraş, M.; Friedrich, C. *J. Rheol.* **2004**, 48, (5), 1135-1146.
24. Binsbergen, F. L. *Nature* **1966**, 211, 516-517.
25. Pennings, J.; Kiel, A. M. *Kolloid ZZ Polym* **1965**, 205, 160.
26. Seki, M.; Thurman, D. W.; Oberhauser, J. P.; Kornfield, J. A. *Macromolecules* **2002**, 35, 2583-2594.
27. Kumaraswamy, G.; Kornfield, J. A.; Yeh, F.; Hsiao, B. S. *Macromolecules* **2002**, 35, 1762-1769.
28. Yamazaki, S.; Watanabe, K.; Okada, K.; Yamada, K.; Tagashira, K.; Toda, A.; Hikosaka, M. *Polymer* **2005**, 46, 1685-1692.
29. Hobbs, J. K.; Humphris, A. D. L.; Miles, M. J. *Macromolecules* **2001**, 34, 5508-5519.
30. Lieberwirth, I.; Loos, J.; Petermann, J.; Keller, A. *Journal of Polymer Science: Part B: Polymer Physics* **2000**, 38, 1183-1187.
31. Garcia Gutierrez, M.; Alfonso, G. C.; Riekel, C.; Azzurri, F. *Macromolecules* **2004**, 37, 478-485.
32. Heeley, E. L.; Fernyhough, C. M.; Graham, R. S.; Olmsted, P. D.; Inkson, N. J.; Embery, J.; Groves, D. J.; McLeish, T. C. B.; Morgovan, A.; Meneau, F.; Bras, W.; Ryan, A. J. *Macromolecules* **2006**, 39, (15), 5058 -5071.
33. Ogino, Y.; Fukushima, H.; Matsuba, G.; Takahashi, N.; Nishida, K.; Kanaya, T. *Polymer* **2006**, 47, 5669-5677.
34. Kimata, S.; Sakurai, T.; Nozue, Y.; Kasahara, T.; Yamaguchi, N.; Karino, T.; Shibayama, M.; Kornfield, J. A. *Science* **2007**, 316, (5827), 1014 - 1017.
35. Swartjes, R. H. M.; Peters, G. W. M.; Rastogi, S.; Meijer, H. E. H. *International Polymer Processing* **2003**, 18, (1), 53-66.
36. Baert, J.; Van Puyvelde, P. *Polymer* **2006**, 47, (16), 5871-5879.
37. Janeschitz-Kriegl, H.; Eder, G. *Journal of Macromolecular Science, Part B* **2007**, 46, (3), 591 - 601.
38. Hsiao, B. S.; Yang, L.; Somani, R. H.; Avila-Orta, C. A.; Zhu, L. *Physical Review Letters* **2005**, 94, 117802.
39. Somani, R. H.; Yang, L.; Zhu, L.; Hsiao, B. S. *Polymer* **2005**, 46, 8587-8623.

40. Keller, A.; Kolnaar, H. W. H., *Flow induced orientation and structure formation*. VCH: New York, **1997**; Vol. 18.
41. Dukovski, I.; Muthukumar, M. *Journal of Chemical Physics* **2003**, 118, (14), 6648-6655.
42. Souane, R.; Isel, F.; Peruch, F.; Lutz, P. J. C. R. *Chimie* **2002**, 5, 43.
43. Ballard, D. G. H.; Cheshire, P.; Longman, G. W. *Polymer* **1978**, 19, 379-385.
44. Doi, M.; Edwards, S. F., *The theory of polymer dynamics*. Clarendon Press: Oxford, 1986.
45. Pogodina, N. V.; Winter, H. H.; Srinivas, S. *Journal of Polymer Science: Part B: Polymer Physics* **1999**, 37, 3512-3519.
46. Coppola, S.; Balzano, L.; Gioffredi, E.; Maffettone, P. L.; Grizzuti, N. *Polymer* **2004**, 45, 3249-3256.
47. Zuidema, H.; Peters, G. W. M.; Meijer, H. E. H. *Macromolecular Theory and Simulations* **2001**, 10, (5), 447 - 460.
48. Swartjes, F. H. M.; Peters, G. W. M.; Rastogi, S.; Meijer, H. E. H. *International Polymer Processing* **2003**, XVIII, (1), 53-66.
49. Nogales, A.; Hsiao, B. S.; Somani, R. H.; Srinivas, S.; Tsou, A. H.; Balta-Calleja, F. J.; Ezquerro, T. *Polymer* **2001**, 42, 5247-5256.
50. Heeley, E. L.; Maidens, A. V.; Olmsted, P. D.; Bras, W.; Dolbnya, I. P.; Fairclough, J. P. A.; Terril, N. J.; Ryan, A. J. *Macromolecules* **2003**, 36, 3656-3665.
51. Heeley, E. L.; Morgovan, A.; Bras, W.; Dolbnya, I. P.; Gleeson, A. J.; Ryan, A. J. *Phys. Chem. Comm.* **2002**, 5, 158-160.
52. Ryan, A. J.; Fairclough, J. P. A.; Terril, N. J.; Olmsted, P. D.; Poon, W. C. K. *Faraday Discussions* **1999**, 112, (13-29).
53. Devaux, N.; Monasse, B.; Haudin, J. M.; Moldenaers, P.; Vermant, J. *Rheol. Acta* **2004**, 43, 210-222.
54. McHugh, A. J. *Polym. Eng. Sci.* **1982**, 22, (15-26).
55. van Meerveld, J.; Peters, G. W. M.; Hutter, M. *Rheol Acta* **2004**, 44, 119-134.
56. Dealy, J. M.; Larson, R. G., *Structure and Rheology of Molten Polymers*. Hanser Gardner Pubns: Cincinnati, 2006.
57. Muthukumar, M. *Advances in Chemical Physics* **2004**, 128.
58. Hsieh, Y.; Hu, X. *Journal of Polymer Science: Part B: Polymer Physics* **1997**, 35, (4), 535-723.

Chapter 4*

Crystallization and dissolution of flow induced precursors

We make use of a specially synthesized linear high density polyethylene (HDPE) with a bimodal molecular weight distribution (MWD) to demonstrate that it is possible to produce a suspension of extended chain shish crystals only in a molten polymer matrix. Such a suspension can be generated at high temperatures, above but close to the equilibrium melting temperature of the unconstrained extended chain crystals ($T_m^0 = 141.2$ °C) and requires stretch of the longest chains of the MWD. After the application of a shear flow of 120 s^{-1} for 1 s at 142 °C, X-ray scattering suggests the presence of a large number of metastable needle-like precursors with limited or no crystallinity. Precursors that are too small dissolve on a timescale that correlates perfectly with the reptation time of the longest polymer molecules. Whereas, precursors that exceed a critical size crystallize forming extended chain shishes.

4.1 Introduction

Considerable efforts have been made to correlate structure developments in semicrystalline polymers and well defined flow conditions. Experiments prove that the final morphology is often imposed by structures (crystalline or not) present in the melt at the early stages of the crystallization. Structures developed at the early stages are referred to as *precursors* and are problematic to study, because of their small dimensions and fast dynamics. However, improving techniques like in-situ small and wide angle X-ray scattering (SAXS and WAXD) and ex-situ microscopy together with increasingly sophisticated simulations are contributing to a more thorough understanding of the physics behind the early stages of crystallization.

Here, some peculiar aspects of the early stages of flow induced crystallization (FIC) are discussed. One of the seminal works for FIC is by Binsbergen¹. He studied FIC in

* Partially reproduced from: Balzano, L. et al. 'Crystallization and dissolution of flow induced precursors', *Physical Review Letters* **2007** (Accepted)

isotactic polypropylene (iPP) by means of cross polarized optical microscopy. In the course of cooling, after the application of ‘heavy strains’ at 180 °C, he observed the onset of birefringent elongated crystallites at temperatures as high as 172 °C where, in quiescent conditions, no crystallization is observed. Similar birefringence was also observed by Pennings in stirred PE solutions ². This morphology was called *shish kebab* (see Figure 4.1 for a schematic drawing) and originates from the crystallization of polymer chains stretched during flow.

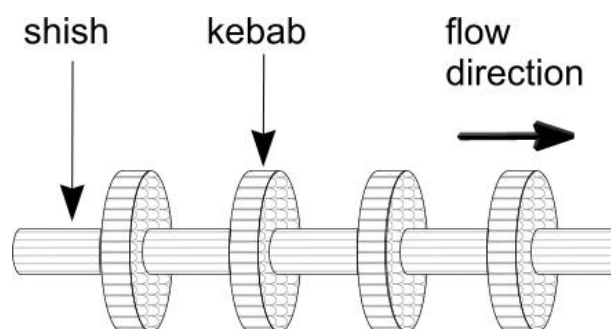


Figure 4.1: Schematic drawing of a shish-kebab crystallite

The structure of shish kebabs consists of an extended chain crystal core, the shish, that supports disk-like folded chain lamellae, the kebabs. The nature of shish kebabs in polyolefin melts and the conditions under which they form have been studied by several groups ³⁻¹⁴. To unveil the microscopic morphological peculiarities of shish kebabs, Hsiao and coworkers used a special blend consisting of 98 wt% of non crystallizable low molar mass polyethylene (PE) copolymer and of 2 wt% of crystallizable ultra high molar mass PE (UHMWPE) ¹⁵. After shearing this blend at 128 °C at a fairly high rate ($\dot{\gamma} = 60 \text{ s}^{-1}$), they observed, with SAXS, the instantaneous formation of shishes followed by a diffusion controlled ($\sim t^{-1/2}$) growth of kebabs. Ex-situ scanning electron microscopy (SEM), showed multiple shishes crossing the same kebabs, a remarkable morphological feature observed for the first time. Hsiao and coworkers also considered the molecular mechanism underlying shish kebab formation ¹⁶. Based on the work of Keller and coworkers ¹⁷, they hypothesize that for a given molar mass (relaxation time), depending on the shear rate $\dot{\gamma}$, the possible chain conformation is coiled or stretched and the ‘coil to stretch’ transition is sharp. Chains having molar mass M above a critical value M^* are stretched and they instantaneously crystallize into the extended chain structure forming shishes. In contrast, chains with $M < M^*$ relax immediately and

cannot be stretched. This low molar mass portion of chains nucleates folding on the outer surface of the shishes and gives rise to the kebabs. The hypothesis of a critical molar mass M^* for chain stretch works in explaining the effects of polydispersity in the molecular weight distribution (MWD) on FIC. At a given molecular weight, the number of chains undergoing stretch, for a given shear rate, is larger in a broad MWD rather than in a narrow MWD. For this reason, as confirmed by experiments, the presence of a high molar mass tail enhances shish kebab formation. Nevertheless, hypothesizing a critical M^* for chain stretch in an entangled polymer melt has some limitations. In fact, in this model, *all* chains with $M > M^*$ should stretch during flow and crystallize in the extended chain form (shish) but molecular dynamics simulations by Muthukumar and coworkers¹⁸ describe a different scenario. According to these authors, a chain in the high molar mass fraction can still retain a coiled conformation during flow. In fact, because of the presence of entanglements, the conformations of neighboring chains are related to each other and, ultimately, the stretch of a high molar mass chain can be blocked by surrounding unstretched chains. Furthermore, recently, Kornfield and coworkers showed the presence of low molar mass molecules within shishes using special blends of low molar mass iPP and deuterated high molar mass iPP¹¹. Their experiments highlight the need for well defined samples in FIC studies.

4.2 Experimental method

4.2.1 Synthesis of a bimodal HDPE

Recent advances in catalyst science allow for a controlled ‘one pot’ synthesis of linear high density polyethylene (HDPE) having a bimodal MWD. The low and the high molar mass components (respectively L-MW and H-MW) of the MWD are generated at the same time from two different pre-catalysts immobilized on the same MgCl_2 based support. In this way a *nascent* blend of the two molar masses is produced with molecular scale mixing. The ratio between H-MW and L-MW can be chosen beforehand changing the relative amount of the two catalysts. An Iron based pre-catalyst, $\{2,6-[(2\text{-chloro-4,6-dimethyl})\text{N}=\text{C}(\text{Me})_2\text{C}_5\text{H}_3\text{N}]\text{FeCl}_2$ or pre-CatFe, was prepared according to a known procedure¹⁹, and a Chromium based pre-catalyst, 1-(8-quinolyl)indenyl]CrCl₂ or pre-CatCr,

was obtained from Basell Polyolefins. 0.18 micromoles of pre-CatFe and 1 micromole of pre-CatCr were co-immobilized onto a $\text{MgCl}_2/\text{AlEt}_n(\text{OEt})_{3-n}$ support by mixing individual solutions of both precatalysts in dichloromethane with 100-120 mg of the support. The slurry of the support together with the precatalysts was kept overnight at room temperature until the supernatant solution became colourless, indicating complete immobilization of the precatalysts.

Polymerization was carried out in a 1 l Premex autoclave. At 50 °C and with an ethylene pressure of 5 bar, 100 mg of the catalyst, mixed in approx. 100 ml of light petroleum, were injected to 400 ml of light petroleum containing the desired amount of cocatalyst. Afterwards, polymerization was carried out at constant pressure for 1hr with a stirring rate of ~1000 rpm. Finally, after venting the reactor, 20 ml of acidified ethanol was added and stirring was continued for 30 min. The polymer was recovered by filtration, washed with water and ethanol and dried in vacuum overnight at 70 °C. To prevent degradation, 0.5 wt% of the antioxidant Irganox 1010 was added to the polymer.

4.2.2 X-ray characterization

The FIC behavior after the application of a shear flow, i.e. structural and morphological developments, was characterized using X-ray scattering. WAXS was performed at the beamline ID11 of the ESRF (Grenoble, France) with a wavelength $\lambda=0.495$ Å and SAXS at the beamline BM26 of the ESRF with $\lambda=1.24$ Å. After integration of the WAXS data, crystallinity was calculated as the ratio between the intensity scattered by the crystals and the total scattered intensity. Shear flow was applied by means of a Linkam Shear Cell CSS-450, where, to avoid unwanted scattering, the original glass of the windows was replaced by kapton.

4.3 Results and discussion

4.3.1 Rheological characterization

The molecular weight distribution of the sample was determined with gel permeation chromatography (GPC), see Figure 4.2.

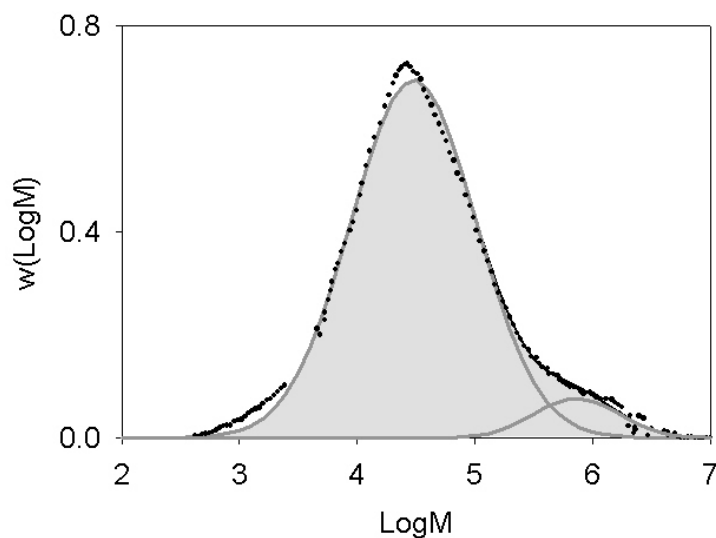


Figure 4.2: Fit of the GPC data with two log-normal distributions (shaded area). The thick lines represent the individual distributions.

Quantitative information, given in Table 4.1, was obtained fitting the experimental data with the weighted sum of two log-normal distribution functions.

Table 4.1: GPC and DSC characterization of the bimodal blend.

GPC							DSC (10 °C/min)		
LMW [g/mol]	LMW M_w/M_n	Z_{LMW}	HMW [g/mol]	HMW M_w/M_n	Z_{HMW}	wt% HMW	T_m [°C]	T_c [°C]	Crystallinity at room temperature
$5.5 \cdot 10^4$	3.4	67	$1.1 \cdot 10^6$	2.3	1338	7	134	118	76%

The deconvolution procedure allows for the identification of two main populations of chains: low molecular weight (LMW) chains with $M_w = 5.5 \cdot 10^4$ g/mol and polydispersity index $M_w/M_n=3.4$ and 7 wt% of high molecular weight chains (HMW) with $M_w = 1.1 \cdot$

10^6 g/mol and $M_w/M_n=2.3$. The critical concentration for overlap of HMW chains C^* can be estimated with:

$$C^* = \frac{M_w}{\frac{4}{3}\pi \langle R_g^2 \rangle^{3/2} \rho N_A} \quad (4.1)$$

where $\langle R_g^2 \rangle^{1/2} = 0.46M_w^{1/2}$ ²⁰, ρ is the density and N_A is the Avogadro number. Using the data of Table 4.1, it is found that $C^* = 0.5$ wt%, i.e. much less than the actual concentration. This implies a significant degree of HMW-HMW chains overlaps (entanglements).

The basic dynamics of polymer molecules in the melt is well described by the theory of Doi and Edwards²¹. According to this theory, due to the steric effect of the neighboring chains, each molecule is confined in a ‘tube’ whose contour describes the molecular conformation. The molecular conformation in the melt is an important issue in the study of the flow induced crystallization (FIC) of a polymer^{5, 22-31}. A tube at rest resembles a random coil, but it can be deformed, oriented and stretched by external stresses. The chain conformation can be assessed introducing two time scales³²: the chain retraction time τ_s corresponding to relaxation time of molecular stretch and the reptation time τ_D corresponding to the relaxation time of molecular orientation. If one neglects polydispersity:

$$\tau_s = \tau_e Z^2 \quad (4.2)$$

$$\tau_D = 3\tau_e Z^3 \left(1 - \frac{1.51}{\sqrt{Z}}\right)^2 \quad (4.3)$$

For PE, the entanglement equilibration time τ_e is $7 \cdot 10^{-9}$ s at 190 °C³³. Assuming $M_e = 828$ g/mol³³, the number of entanglements per chain $Z = M_w/M_e$ is $Z_{LMW} = 67$ for the short chains and $Z_{HMW} = 1338$ for the long chains. Using Equation (4.2) and (4.3) and assuming an Arrhenius type of temperature dependence (with $E_a = 36$ kJ/mol), the relaxation times τ_s and τ_D can be calculated for both LMW and HMW at all temperatures. The measured frequency dependent mechanical response of the molten bimodal blend at 140 °C is shown in Figure 4.3 ($\tau_D^{HMW} \cong 140$ s and $\tau_D^{LMW} \cong 0.01$ s). Two main relaxation processes, associated to reptation of LMW and HMW chains, are expected at frequencies of the order of $\omega_{LMW} = 1/\tau_D^{LMW}$ and $\omega_{HMW} = 1/\tau_D^{HMW}$ (note that $\omega_{LMW} > \omega_{HMW}$). At $\omega > \omega_{LMW}$ ($> \omega_{HMW}$) the networks of both LMW and HMW chains are addressed and an

elastic-like response (plateau in G') is expected. However, in the experimental frequency window this behavior cannot be observed as $\omega_{LMW} = 1/\tau_D^{LMW} \cong 100 \text{ s}^{-1}$. For $\omega_{HMW} < \omega < \omega_{LMW}$, the rheology is a convolution of the reptation of LMW chains and of the elasticity of the network of HMW chains. The mark of the long relaxation times of HMW chains is visible at very low frequencies ($\sim 10^{-3} \text{ s}^{-1}$), when a change in the slopes of G' and G'' indicates the onset of a plateau ('diluted' plateau of HMW chains). Finally, when $\omega < \omega_{HMW} \cong 0.007 \text{ s}^{-1}$, both LMW and HMW chains reptate and a terminal behavior is expected. However, the data of Figure 4.3 suggest that the terminal behavior may occur for $\omega < 10^{-3} \text{ s}^{-1}$, i.e. outside the experimental window and at a frequency lower than expected. This discrepancy can be justified with the polydispersity of the HMW chains.

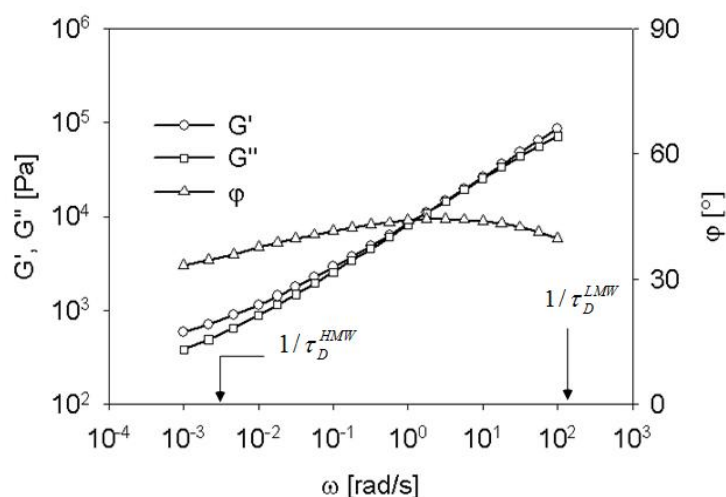


Figure 4.3: Moduli and phase angle for the molten bimodal blend at 140 °C. The applied strain is 10 % that is within the linear viscoelastic window.

The large difference between Z_{LMW} and Z_{HMW} causes large differences in the relaxation times of HMW and LMW molecules and, ultimately, can reduce the relaxation times of HMW molecules (!). In fact, LMW molecules, acting as a plasticizer, change G_N^0 of the HMW chains according to:

$$G_N^0 = \left(G_N^0\right)_{melt} \phi^d \quad \text{with } 2.1 < d < 2.3 \quad (4.4)$$

ϕ is the concentration of HMW chains. A reduction of G_N^0 corresponds to an increase in M_e and therefore to a reduction of the relaxation times because of less entanglements per chain. The bimodal blend is re-examined as a solution of HMW PE in a solvent of LMW PE and, as such, LMW molecules dilute HMW molecules. This dilution increases M_e of HMW chains

and, in turn, reduces τ_D^{HMW} . In a melt of entangled molecules, dilution is a dynamic process based on the limited lifetime of some entanglements. The tube of a HMW molecule is defined by entanglements from both LMW and HMW molecules. The life time of the LMW defined constraints are equal to the disengagement time of LMW chains τ_D^{LMW} . During the time τ_{diam}^{HMW} needed for the HMW test chain to reptate a distance equal to the tube diameter, the LMW entanglements can be released (constraint release). In that case, they do not count as an entanglement for the test chain. As a result of these constraint releases, the tube diameter a increases or, equivalently, the number of entanglements (averaged in the time τ_{diam}^{HMW}) decreases. This constraints release mechanism, called ‘dynamic tube dilution’ or DTD, becomes important when $\tau_D^{LMW} < \tau_{diam}^{HMW}$. The dimensionless ratio:

$$Gr = \tau_{diam}^{HMW} / \tau_D^{LMW} \sim Z_{HMW} / Z_{LMW}^3 \quad (4.5)$$

is called Struglinksii-Graessley number and, for PE, it was established that DTD takes place when Gr exceeds $Gr_c = 0.06$ ³³. For the bimodal HDPE blend investigated in this work $Gr \cong 0.005$ that is far smaller than Gr_c . Hence, DTD is excluded and relaxation times are calculated with Equations (4.2) and (4.3). The values of τ_D and τ_s , for H-MW and L-MW chains, at 142 °C, are useful for the following discussion and are reported in Table 4.2.

Table 4.2: Relaxation times calculated with Equations (4.2) and (4.3) at 142°C.

	τ_D [s]	τ_s [s]
L-MW	0.01	$9 \cdot 10^{-6}$
H-MW	140	0.04

4.3.2 Thermodynamics of flow induced precursors

The anisotropic precursors of shish kebabs are metastable bundles of molecules stretched by the flow. Their life time strongly depends on their size and the temperature. It seems reasonable to assume that flow induced precursors (FIPs) are cylindrical. The free energy associated to the formation of a single (crystalline) FIP with a length L and a diameter D can be written as:

$$\Delta G_{tot}(L, D) = -\left(\frac{\pi D^2}{4} L\right) |\Delta g| + 2\left(\frac{\pi D^2}{4}\right) \sigma_{end} + \pi D L \sigma_{lat} \quad (4.6)$$

with $\Delta g = g_c - g_m^{shear}$ being the specific free energy difference between the crystalline state (g_c) and the sheared melt (g_m^{shear}) while σ_{end} and σ_{lat} are the free energies of the end and lateral surfaces. The spontaneous growth of a precursor can take place only when it reduces the free energy ($\Delta G_{tot} < 0$), hence, after some critical dimensions are exceeded. The critical dimensions L_{cr} and D_{cr} can be obtained from the maximum of ΔG_{tot} with respect to L and D. The condition $\partial \Delta G_{tot} / \partial D = \partial \Delta G_{tot} / \partial L = 0$ yields:

$$D_{cr} = 4\sigma_{lat} / |\Delta g| \quad (4.7)$$

$$L_{cr} = 4\sigma_{end} / |\Delta g| \quad (4.8)$$

For PE, $\sigma_{end} / \sigma_{lat} \sim 10^{34}$ and, therefore, thermodynamical stability is assured for:

$$L_{cr} / D_{cr} > 10 \quad (4.9)$$

A precursor with $L > L_{cr}$, $D > D_{cr}$ and satisfying the condition (4.9) can grow into a shish, whereas, it dissolves into the melt if these conditions are not fulfilled. Note that the value 10 in (4.9) should be considered only as an order of magnitude. Like any other melting process, the characteristic dissolution or life time (t_{FIP}^*) of subcritical FIPs depends on their size and morphology (i.e. fiber- or lamellae- like³⁵). Because of a (partial) extended chain structure, FIPs can be rather stable and it is reported that for polymers like PE, iPP, iPB-1 and PS, they can survive for hours at temperatures near the melting point of spherulites. Nevertheless, t_{FIP}^* decreases dramatically with increasing temperature. According to Janeschitz-Kreigl and coworkers³⁶ and to Alfonso and coworkers³⁷, t_{FIP}^* as a function of the temperature is well described by an Arrhenius law. The study of the dissolution of precursors could provide information on their nature and, therefore, new insights in the early stages of FIC. However, not much is known about the effect of size and morphology on t_{FIP}^* . In fact, (quoting Janeschitz-Kriegl³⁶) ‘most of the experiments were carried out at temperatures below the melting point of spherulites where FIPs are practically stable from the moment of their creation’. Exceptions are listed in Table 4.3 which reveals that FIPs have been observed at very high temperatures, for different materials and for a broad variety of flow conditions. However, only in few cases^{37, 38} the dynamics of FIPs are related to a well defined temperature: the equilibrium melting temperature T_m^0 . In all the other cases, the ‘nominal’ melting point T_m of the material is used as a reference. The downside of this choice is that T_m

depends strongly on the experimental conditions. Moreover, a clear method for determining t_{FIP}^* is often missing and only coarse values are given.

4.3.3 Flow induced precursors just above the equilibrium melting temperature

According to classical thermodynamics⁴⁸, the driving force for nucleation is the reduction of the Gibbs free energy (G): $\Delta G < 0$. For quiescent conditions, crystallization leads to folded chain lamellae and the corresponding free energy change is $\Delta G_q = G_{\text{lamellae}} - G_{\text{melt}} = \Delta H(1 - T / T_m^0)$ where ΔH (negative value) is the latent heat and T_m^0 the equilibrium melting temperature of the folded chain crystals. The thickness (l) of folded chain crystals is inversely proportional to the undercooling ($l \sim 1 / (T_m^0 - T)$) and can be predicted with the Gibbs-Thomson equation: $l = -2\sigma_e / \Delta H(1 - T / T_m^0)$, σ_e is the fold surface energy. For PE, the equilibrium melting temperature for unconstrained extended chain crystals is $T_m^0 = 141.2$ °C and no chain folding is possible above this temperature. This means that, for $T \geq T_m^0$, where there is no driving force in quiescent conditions, kebabs cannot be formed. However, an extra driving force for nucleation can be introduced applying flow to the system. After cessation of flow, according to the Doi-Edwards (DE) model²¹, a chain is confined in a virtual tube that limits its conformations. The random coil conformation can be attained again only by reptation of the chain out of the tube. At every time, the fraction μ of the chain that is still in the tube is given by the *memory function*:

$$\mu(t; \tau_D) = \frac{8}{\pi^2} \sum_{p \text{ odd}} \frac{1}{p^2} \exp\left(-p^2 \frac{t - t_0}{\tau_D}\right) \quad (4.10)$$

Flow reduces the possible chain conformations promoting chain orientation and stretch, thus increasing the free energy of the melt. The capability of the flow of inducing orientation and stretch of the chains can be quantified defining two Deborah numbers³²: $De_{or} = \tau_D \dot{\gamma}$ and $De_{str} = \tau_s \dot{\gamma}$ that measure the ratio between flow and relaxation rates at chain and segmental level respectively. Chain orientation is achieved when De_{or} exceeds unity while chain stretch when De_{str} exceeds unity.

Grizzuti and coworkers²³ accounted for the extra driving force due to flow introducing an additive term (ΔG_f) in the free energy change: $\Delta G = \Delta G_q + \Delta G_f$. With this definition, the equilibrium temperature rises to $T_m^{flow} = T_m^0(1 + \Delta G_f / \Delta H)$ and crystallization becomes possible even above T_m^0 . However, as already mentioned, for these conditions no chain folding can take place and only extended chain crystals can be formed if the driving force is large enough. Figure 4.4 shows X-ray scattering data after application of shear with $\dot{\gamma} = 120 \text{ s}^{-1}$ for 1 s at 142 °C.

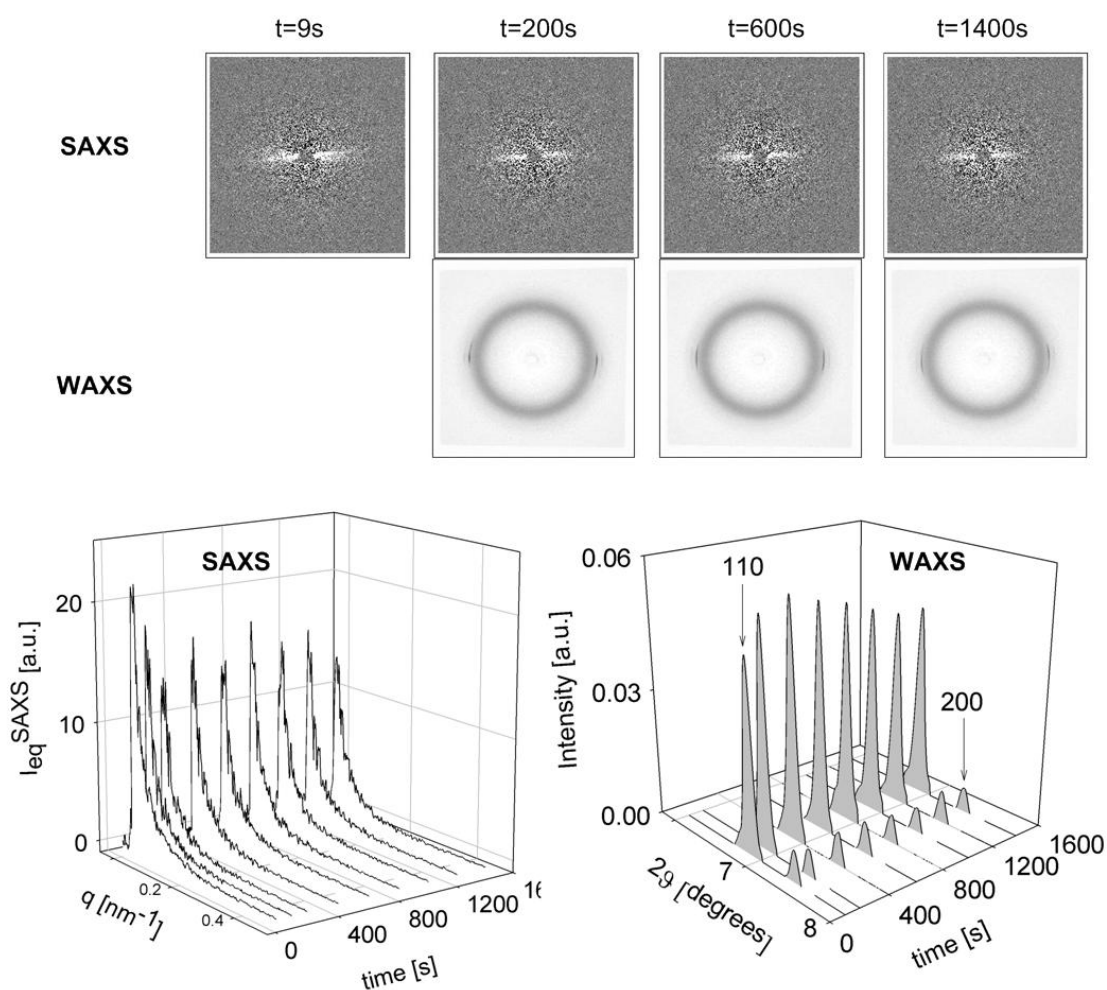


Figure 4.4: SAXS and WAXD data recorded after the application of a shear of 120 s^{-1} for 1 s at 142 °C. In the two-dimensional scattering images shown at the top, the flow direction is vertical. For the WAXD intensity, the scattering of the amorphous component was subtracted and only the crystalline peaks are visible

Table 4.3: Literature survey on flow induced precursors at high temperatures.

Reference	Material	Molar Mass	T _m	Flow	T _{flow}	Technique(s)	Observations	Life Precursors	time
Binsbergen (1966) ¹	iPP		165°C	Shear	180°C	OM	Birefringent nucleation lines		
Titomanlio et al. (1990) ³⁹	HDPE	M _w =395.000	129°C	Capillary flow (d=1 to 1.5mm, L=5 to 60mm)	142°C	Measure of pressure drop	Increase of Δp		
Chai et al. (1995) ⁴⁰	HDPE		~135°C	Shear	140°C	Raman	All-trans sequences induced by shear	Several hours	
Goschel et al. (2000) ⁴¹	iPP	M _w =365.000 M _w /M _n =5.45	165°C	Contraction flow	170°C	WAXD	Crystalline peaks		
Garcia Gutierrez et al. (2004) ⁸	iPS	M _w =939.000 M _w /M _n =6.4	T _m ⁰ =243°C	Fiber pullout (shear)	260°C	SAXS and WAXD	Shish-kebab morphology with low degree of crystallinity	<40min	
Sakellarides et al. (1987) ⁴²	HDPE	MFI=0.15	133°C	Extensional	140°C	OM	Fibrils	Long time periods	
Kumaraswamy et al. (1999) ⁴³	iPP	M _w =300.000 M _w /M _n =7÷8	172°C	Shear	175°C	SALS OM	Upturn in birefringence (in situ). Formation of a skin layer (ex situ)	Few seconds at 175°C and increases at lower T. Shear induced structures are stable at 160°C	
Isayev et al. (1995) ⁴⁴	iPP	M _w =351.000 M _w /M _n =4.3	165°C	Flow through a slit-die	210°C	OM	Formation of an oriented layer cooling after flow at 210°C	~50 s at 210°C ~100s at 200°C	
Somani et al. (2002) ³⁵	iPP	M _n =92.000 M _w =368.000 M _z =964.000	162°C	Shear	175°C	SAXS and WAXD	Formation of non crystalline shish-kebabs	>120min	

Azzurri et al. (2005) ³⁷	iPB-1	$M_n=37,000 \div 125,000$ $M_w = 116,000 \div 850,000$ $M_w/M_n=3.1 \div 6.8$	138°C	Fiber pullout (shear)	130÷150 °C	OM	Formation of cylindrical morphologies on cooling after shear	Several hours depending on molar mass and T. Arrhenius-type of T dependence
Janeschitz-Krieger et al. (2007) ³⁶	iPP		~170°C	Shear	190÷210 °C	SALS	Thread precursors like	~60 s at 190°C >10s above 200°C Arrhenius type dependence on T.
Keum et al. (2007) ³⁸	PE	Bimodal with LMW: $M_w=110,000$ $M_w/M_n=9$ HMW: $M_w=5,500,000$ $M_w/M_n=9$	$T_m^0=145.2$ °C	Shear	142°C	SAXS and WAXD	Shishes without kebabs	>45 min. Shishes partially relax after flow but grow subsequently
Kanaya et al. (2007) ⁴⁵	iPS	$M_w=400,000$ $M_w/M_n=2$	223°C	Shear	250 and 270°C	Depolarized Light Scattering and POM	Streak-like scattering from long flow oriented structures	

Furthermore see the review [46] and the theoretical predictions in [47].

Such a shear is efficient in orienting and stretching H-MW chains as $De_{or}^{H-MW} = 1.6 \cdot 10^4$ and $De_{str}^{H-MW} = 4.5$, while it can hardly orient and surely not stretch L-MW chains as $De_{or}^{L-MW} = 1.5$ and $De_{str}^{L-MW} = 0.01$. Immediately after cessation of shear ($t=0$), SAXS images show an equatorial streak where the intensity decreases continuously with scattering angle. This indicates the formation of needle-like precursors aligned in the shear direction. This scattering pattern is retained for the full experimental time (1600 s). Simultaneously, WAXD images show the fingerprint of an orthorhombic lattice (with 110 and 200 reflections) having a high degree of orientation. Interestingly, the integrated intensity of the SAXS equatorial streak, I_{eq}^{SAXS} , and the calculated WAXD crystallinity, X^{WAXD} , are not correlated during the initial transient of ~ 160 s. As shown in Figure 4.5, I_{eq}^{SAXS} builds up quickly reaching a maximum at $t_{max} = 6$ s and then decreases exponentially while X^{WAXD} builds up gradually to the stationary value of 0.4 %.

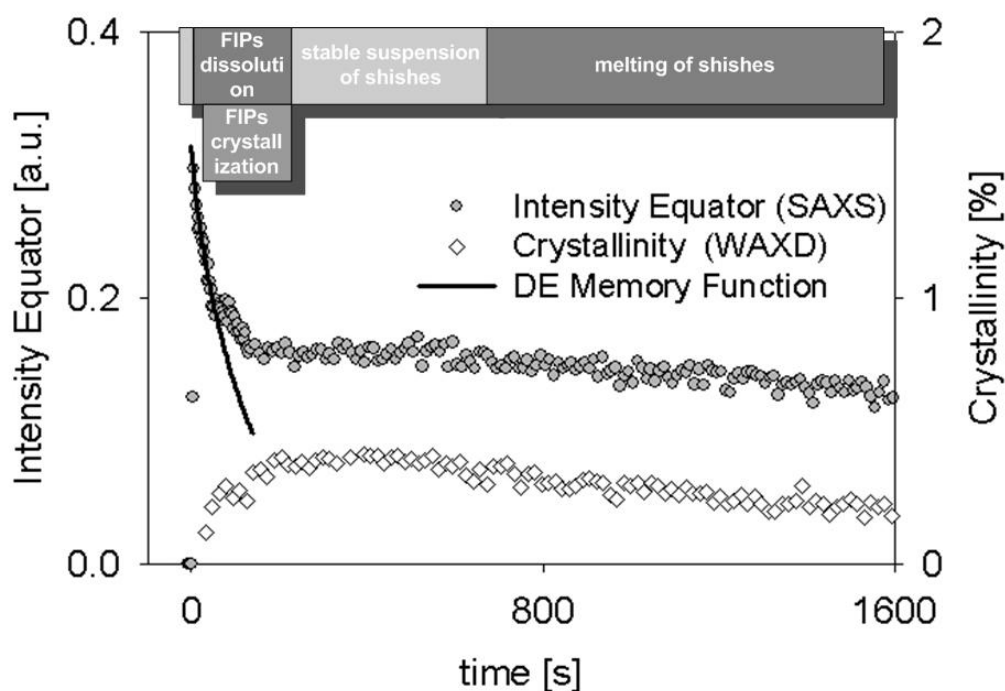


Figure 4.5: I_{eq}^{SAXS} and X^{WAXD} as a function of time after step shear at 142 °C. The initial drop of I_{eq}^{SAXS} can be fitted with the memory function of the Doi-Edwards (DE) model, the fit is represented by the continuous line.

These experimental evidences suggest the formation of a polydisperse set of needle-like precursors that, initially, are characterized by undetectable crystallinity. The stability of precursors is related to their size (see Equation (4.9)). Those exceeding some critical dimensions are stable and have time to refine their structure to a proper crystal lattice, forming shishes and increasing the crystallinity. On the other hand, those that are smaller than the critical dimension dissolve, decreasing I_{eq}^{SAXS} and do not contribute to crystallinity. In the first 60 s, as shown in Figure 4.5, the drop of I_{eq}^{SAXS} is well described with the Doi-Edwards *memory function*:

$$I_{eq}^{SAXS}(t) = S_y \cdot \mu(t, \tau_D^{H-MW}) \quad (4.11)$$

where $\tau_D^{H-MW} = 140 \text{ s}$, obtained from Equation (4.3), is the only time constant. The vertical shift factor S_y is necessary because of the arbitrariness of the intensity scale and is the only fit parameter. The good correlation between data points and Equation (4.11) strongly suggests that dissolution of the subcritical precursors involves reptation of H-MW chains. This also means that stretched H-MW chains are the precursor's backbones.

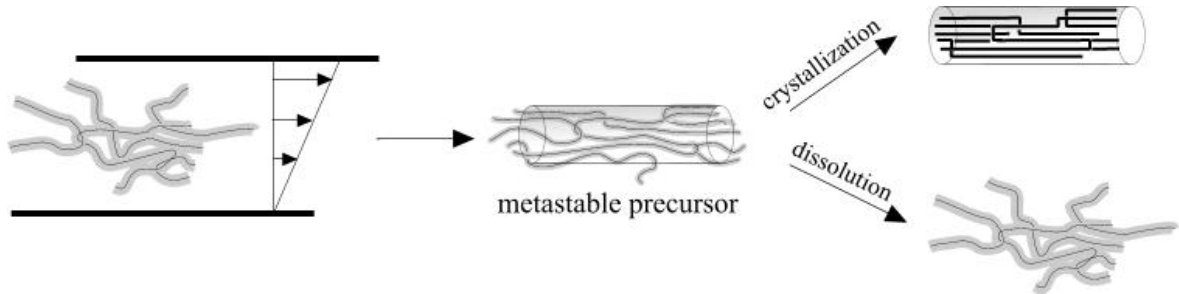


Figure 4.6: Crystallization or dissolution of flow-induced precursors depends on their size. The thick gray line represents the tube containing the chain.

For times longer than 60 s, dissolution of precursors slows down dramatically and at $\sim 200 \text{ s}$ a steady state is approached: both I_{eq}^{SAXS} and X^{WAXD} remain constant indicating the presence of stable and crystalline shishes. The Bragg spacings corresponding to the 110 and 200 crystalline peaks are $d_{110} = 4.14 \text{ \AA}$ and $d_{200} = 3.86 \text{ \AA}$ and they are independent of time.

Therefore, the unit cell parameters $a = 2d_{200} = 7.6 \text{ \AA}$ and $b = \left[(d_{110})^{-2} - (2d_{200})^{-2} \right]^{-1/2} = 4.9 \text{ \AA}$ are also independent of time. These values are consistent with data for PE available in the

literature⁴⁹. The apparent lateral dimension δ_{hkl} of shishes in the hkl direction can be estimated with the Scherrer equation⁵⁰:

$$\delta_{hkl} = \frac{0.9\lambda}{B_{hkl} \cos \theta_{hkl}} \quad (4.12)$$

where θ_{hkl} is half of the scattering angle and B_{hkl} the angular breadth (in radians) of the hkl reflection. The values obtained for the 110 and 200 reflections are shown as a function of the time in Figure 4.7 and are scattered around $\delta_{110} \cong 21$ nm and $\delta_{200} \cong 31$ nm.

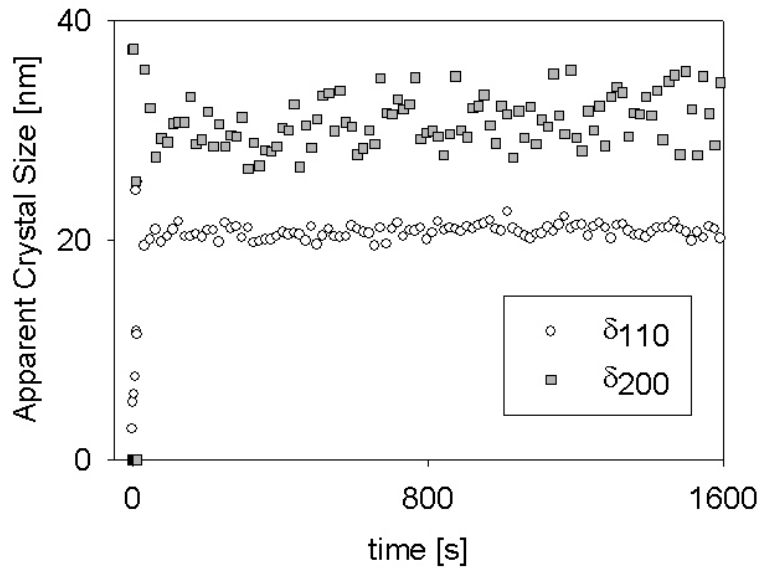


Figure 4.7: Apparent lateral size of the shishes in the 110 and 220 direction at 142 °C after a shear of 120 s^{-1} for 1 s.

The stability of the suspension of shishes is, however, limited to ~ 400 s because of the high temperature. Both I_{eq}^{SAXS} and X^{WAXD} start to slowly decrease when $t \cong 600$ s indicating that the crystalline shishes slowly melt. The average diameter of the shishes can be estimated as $D_{shish} = \delta_{200}$. The average length of the shishes can be estimated with Ruland's method⁵¹⁻⁵³ that analyzes the changes of the azimuthal breadth of the SAXS equatorial streak as a function of q . This analysis provides a value of $L_{shish} \cong 260$ nm. In average, $L_{shish}/D_{shish} \cong 8$ indicating that the aspect ratio of the precursors is indeed critical (see Equation (4.9)). For this reason, many shishes do not meet the stability requirements and start a slow melting at $t \cong 600$ s, resulting in a slow decrease of I_{eq}^{SAXS} and of X^{WAXD} . However, in

this process, δ_{200} (and D_{shish}) remains unaffected suggesting that, in these conditions, melting of the shishes occurs at the end surfaces.

4.4 Conclusions

In this Chapter, we show that by applying shear flow to a bimodal HDPE melt it is possible to generate a suspension of *only* extended chain shishes. This is feasible at a high temperature as high as 142 °C, just above the equilibrium melting temperature of folded chain lamellae. In these conditions, shear can induce a large amount of needle-like FIPs causing a clear mark in the SAXS (equatorial streak of intensity). At the same time nucleation of the kebabs is suppressed because of the high temperature. At such a high temperature, many FIPs do not meet the size requirements for stability and dissolve in the melt. Remarkably, their dissolution time scale (measurable with SAXS) matches the time scale for the reptation of HMW molecules. This link between dissolution of subcritical FIPs and HMW chain dynamics suggests that the early FIPs are made essentially of HMW chains. Needle-like FIPs meeting the stability requirements crystallize with an orthorhombic lattice giving rise to a suspension of crystalline shishes only. However, with the applied flow conditions (120 s^{-1} for 1 s), at 142 °C, the aspect ratio of the shishes is critical and after 600 s they start slow melting from the end surfaces.

In this Chapter, the formation of precursors and their crystallization into extended chain shishes is discussed. In the following Chapter, we show that these extended chain crystals can be used as nucleating substrate. Because of their exact epitaxy matching and flow alignment, shishes generated at high temperature can template the crystallization of high oriented polymer morphologies.

4.5 References

1. Binsbergen, F. L. *Nature* **1966**, 211, 516-517.
2. Pennings, J.; Kiel, A. M. *Kolloid ZZ Polym* **1965**, 205, 160.
3. Seki, M.; Thurman, D. W.; Oberhauser, J. P.; Kornfield, J. A. *Macromolecules* **2002**, 35, 2583-2594.

4. Kumaraswamy, G.; Kornfield, J. A.; Yeh, F.; Hsiao, B. S. *Macromolecules* **2002**, *35*, 1762-1769.
5. Yamazaki, S.; Watanabe, K.; Okada, K.; Yamada, K.; Tagashira, K.; Toda, A.; Hikosaka, M. *Polymer* **2005**, *46*, 1685-1692.
6. Hobbs, J. K.; Humphris, A. D. L.; Miles, M. J. *Macromolecules* **2001**, *34*, 5508-5519.
7. Lieberwirth, I.; Loos, J.; Petermann, J.; Keller, A. *Journal of Polymer Science: Part B: Polymer Physics* **2000**, *38*, 1183-1187.
8. Garcia Gutierrez, M.; Alfonso, G. C.; Riekkel, C.; Azzurri, F. *Macromolecules* **2004**, *37*, 478-485.
9. Heeley, E. L.; Fernyhough, C. M.; Graham, R. S.; Olmsted, P. D.; Inkson, N. J.; Embery, J.; Groves, D. J.; McLeish, T. C. B.; Morgovan, A.; Meneau, F.; Bras, W.; Ryan, A. J. *Macromolecules* **2006**, *39*, (15), 5058 -5071.
10. Ogino, Y.; Fukushima, H.; Matsuba, G.; Takahashi, N.; Nishida, K.; Kanaya, T. *Polymer* **2006**, *47*, 5669-5677.
11. Kimata, S.; Sakurai, T.; Nozue, Y.; Kasahara, T.; Yamaguchi, N.; Karino, T.; Shibayama, M.; Kornfield, J. A. *Science* **2007**, *316*, (5827), 1014 - 1017.
12. Swartjes, R. H. M.; Peters, G. W. M.; Rastogi, S.; Meijer, H. E. H. *International Polymer Processing* **2003**, *18*, (1), 53-66.
13. Baert, J.; Van Puyvelde, P. *Polymer* **2006**, *47*, (16), 5871-5879.
14. Janeschitz-Kriegl, H.; Eder, G. *Journal of Macromolecular Science, Part B* **2007**, *46*, (3), 591 - 601.
15. Hsiao, B. S.; Yang, L.; Somani, R. H.; Avila-Orta, C. A.; Zhu, L. *Physical Review Letters* **2005**, *94*, 117802.
16. Somani, R. H.; Yang, L.; Zhu, L.; Hsiao, B. S. *Polymer* **2005**, *46*, 8587-8623.
17. Keller, A.; Kolnaar, H. W. H., *Flow induced orientation and structure formation*. VCH: New York, **1997**; Vol. 18.
18. Dukovski, I.; Muthukumar, M. *Journal of Chemical Physics* **2003**, *118*, (14), 6648-6655.
19. Souane, R.; Isel, F.; Peruch, F.; Lutz, P. J. C. R. *Chimie* **2002**, *5*, 43.
20. Ballard, D. G. H.; Cheshire, P.; Longman, G. W. *Polymer* **1978**, *19*, 379-385.
21. Doi, M.; Edwards, S. F., *The theory of polymer dynamics*. Clarendon Press: Oxford, 1986.
22. Pogodina, N. V.; Winter, H. H.; Srinivas, S. *Journal of Polymer Science: Part B: Polymer Physics* **1999**, *37*, 3512-3519.
23. Coppola, S.; Balzano, L.; Gioffredi, E.; Maffettone, P. L.; Grizzuti, N. *Polymer* **2004**, *45*, 3249-3256.
24. Zuidema, H.; Peters, G. W. M.; Meijer, H. E. H. *Macromolecular Theory and Simulations* **2001**, *10*, (5), 447 - 460.
25. Swartjes, F. H. M.; Peters, G. W. M.; Rastogi, S.; Meijer, H. E. H. *International Polymer Processing* **2003**, XVIII, (1), 53-66.
26. Nogales, A.; Hsiao, B. S.; Somani, R. H.; Srinivas, S.; Tsou, A. H.; Balta-Calleja, F. J.; Ezquerro, T. *Polymer* **2001**, *42*, 5247-5256.
27. Heeley, E. L.; Maidens, A. V.; Olmsted, P. D.; Bras, W.; Dolbnya, I. P.; Fairclough, J. P. A.; Terril, N. J.; Ryan, A. J. *Macromolecules* **2003**, *36*, 3656-3665.
28. Heeley, E. L.; Morgovan, A.; Bras, W.; Dolbnya, I. P.; Gleeson, A. J.; Ryan, A. J. *Phys. Chem. Comm.* **2002**, *5*, 158-160.
29. Ryan, A. J.; Fairclough, J. P. A.; Terril, N. J.; Olmsted, P. D.; Poon, W. C. K. *Faraday Discussions* **1999**, *112*, (13-29).
30. Devaux, N.; Monasse, B.; Haudin, J. M.; Moldenaers, P.; Vermant, J. *Rheol. Acta* **2004**, *43*, 210-222.

31. McHugh, A. J. *Polym. Eng. Sci.* **1982**, 22, (15-26).
32. van Meerveld, J.; Peters, G. W. M.; Hutter, M. *Rheol Acta* **2004**, 44, 119-134.
33. Dealy, J. M.; Larson, R. G., *Structure and Rheology of Molten Polymers*. Hanser Gardner Pubns: Cincinnati, 2006.
34. Wunderlich, B., *Thermal analysis of polymeric materials*. Springer-Verlag: Berlin, 2005.
35. Somani, R. H.; Yang, L.; Hsiao, B. S. *Physica A* **2002**, 304, 145-157.
36. Janeschitz-Kriegl, H.; Eder, G. *Journal of Macromolecular Science, Part B* **2007**, 46, 591-601.
37. Azzurri, F.; Alfonso, G. C. *Macromolecules* **2005**, 38, 1723-1728.
38. Keum, J. K.; Zuo, F.; Hsiao, B. S. *Journal of Applied Crystallography* **2007**, 40, 48-51.
39. Titomanlio, G.; Marrucci, G. *AIChE* **1990**, 36, (1), 13.
40. Chai, C. K.; Dixon, N. M.; Gerrard, D. L.; Reed, W. *Polymer* **1995**, 36, (3), 661-663.
41. Goschel, U.; Swartjes, F. H. M.; Peters, G. W. M.; Meijer, H. E. H. *Polymer* **2000**, 41, 1541-1550.
42. Sakellarides, S. L.; McHugh, A. J. *Rheol Acta* **1987**, 26, 64-77.
43. Kumaraswamy, G.; Issaian, A. M.; Kornfield, J. A. *Macromolecules* **1999**, 32, 7537-7547.
44. Isayev, A. I.; Chan, T. W.; Shimojo, K.; Gmerek, M. *Journal of Applied Polymer Science* **1995**, 55, (807-819).
45. Kanaya, T.; Takayama, Y.; Ogino, Y.; Matsuba, G.; Nishida, K. *Lect. Notes Phys.* **2007**, 714, 87-96.
46. Kumaraswamy, G. *Journal of Macromolecular Science, Part C: Reviews* **2005**, 45, 375-397.
47. Ziabicki, A.; Alfonso, G. C. *Macromol. Symp.* **2002**, 185, 211-231.
48. Muthukumar, M. *Advances in Chemical Physics* **2004**, 128.
49. Hsieh, Y.; Hu, X. *Journal of Polymer Science: Part B: Polymer Physics* **1997**, 35, (4), 535-723.
50. Cullity, B. D.; Stock, S. R., *Elements of X-ray diffraction*. Prentice Hall: Upper Saddle River, 2001.
51. Ruland, W. *Journal of Polymer Science: Part C* **1969**, 28, 143-151.
52. Keum, J. K.; Somani, R. H.; Zuo, F.; Burger, C.; Sics, I.; Hsiao, B. S.; Chen, H.; Kolb, R.; Lue, C. *Macromolecules* **2005**, 38, 5128-5136.
53. Yang, L.; Somani, R. H.; Sics, I.; Hsiao, B. S.; Kolb, R.; Fruitwala, H.; Ong, C. *Macromolecules* **2004**, 37, 4845-4859.

Chapter 5*

Precursors, crystallization and melting in sheared bimodal HDPE melts

In a crystallizable polymer melt, flow can induce metastable precursors of crystallization with very low or no crystallinity. These flow induced precursors (FIPs) can control the subsequent developments of the crystalline morphology. FIPs are active in the early stages of crystallization, enhancing the kinetics and promoting the formation of oriented shish kebabs. To study the formation of FIPs in shear flow, we make use of a specially synthesized blend of low and high molecular weight (LMW and HMW) linear HDPE. Remarkably, we found that, at 142 °C, just above the equilibrium melting temperature T_m^0 , shearing the melt can induce needle-like precursors that are clearly detectable with X-ray scattering. At this high temperature, only FIPs with an extended chain structure are stable and can crystallize, forming a suspension of shishes without kebabs. The other FIPs (with folded chain structure or with extended chain structure but too small to grow) have a limited lifetime and relax back to the melt state. The timescale of relaxation of these subcritical precursors matches the disengagement time of the HMW fraction, suggesting that the early FIPs are HMW rich. Analysis of the flow conditions indicate that FIPs arise with the stretching of the network formed by the mutually entangled HMW molecules, but only if a critical strain is exceeded. FIPs and shishes generated with shear at 142 °C can be used as seeds for the nucleation of the rest of the molecules. On cooling, the onset of bulk crystallization can shift up to 132 °C depending on the flow conditions. Bulk crystallization starts with nucleation of kebabs at high temperature and, if molten material is still available, proceeds, at lower temperature with homogeneous nucleation of randomly oriented lamellae that decrease the degree of orientation of the crystalline morphology. For certain flow conditions, sufficient shishes are created to template a fully oriented morphology without homogeneous nucleation of randomly oriented lamellae. Shish-kebabs exhibit an enhanced thermal stability. The crystallization of kebabs is reversible and melting of kebabs restores a suspension of shishes that, eventually, melt at a higher temperature.

* Partially reproduced from: L. Balzano et al. 'Precursors, crystallization and melting in sheared bimodal HDPE melts', *Macromolecules* **2008** (Submitted)

5.1 Introduction

As shown in the earlier Chapters, flow plays an important role in the morphological developments¹⁻⁵. Flow promotes the formation of anisotropic crystalline structures with a cylindrical symmetry that are called *shish-kebabs*⁶⁻⁸. In the simplest case, shish-kebabs are made of a single fibrillar crystal bearing periodically spaced disk-like lamellae⁹⁻¹¹, but more complex arrangements have also been observed¹². The formation of shish-kebabs starts with anisotropic precursors that, depending on the conditions, can grow or dissolve back to the melt state. Shish-kebabs can be beneficial for the mechanical properties of the material. Ultra high molecular weight polyethylene (UHMWPE) with a shish-kebab morphology can have a Young's modulus up to 100 GPa¹³. Shish-kebabs exhibit also an enhanced thermal stability and can be superheated well above the melting point of spherulites. For example, for certain conditions, shish-kebabs can melt at temperatures as high as 160 °C for PE¹⁴, as high as 190 °C for isotactic polypropylene (iPP)¹⁵ and as high as 255 °C for isotactic polystyrene (iPS)¹⁶.

The enhancement of mechanical properties and thermal stability caused by the formation of shish-kebabs was extensively studied in the last decades. From the initial observations by Pennings¹⁷ on stirred PE solutions and by Binsbergen¹⁸ on iPP melts, it was already clear that they arise from the crystallization of polymer chains stretched by the flow. Stretched chains have a high segmental orientation that allows them to crystallize faster than coiled chains and form fibrillar crystals. Keller and coworkers³ rationalized the formation of shish-kebabs linking it to the molecular weight (M_w) and to the polydispersity of the melt. At a strain rate $\dot{\gamma}$, molecules with a molar mass M above a critical value M^* can undergo stretch, while all the others relax rapidly and retain a coiled configuration. From the coexistence of coiled and stretched chains in the melt, two different structural events in the formation of shish-kebabs were identified: 1) extended chain crystallization of the stretched molecules leading to shishes and 2) epitaxial (heterogeneous) crystallization of the coiled molecules leading to kebabs. Recently, simulations of the groups of Frenkel¹⁹ and Muthukumar²⁰ confirmed this mechanism. In both cases, a shish was 'artificially' introduced in a simulation box filled with relatively short coiled chains. Time resolved snapshots revealed that the shish acts as a nucleating substrate promoting the epitaxial crystallization of short chains that gives rise to the kebabs. Experimental evidence for (flow induced) formation of shishes followed by the growth of kebabs is given by several groups^{6, 21-24}. However, the formation of shishes

and the epitaxial crystallization of kebabs have not been studied separately because the time interval, separating these two processes, is often too short. Experimental conditions to achieve a clear separation between the formation of shishes and of kebabs were identified recently²⁵.

In this Chapter, we discuss the effects of the external conditions (temperature and flow) on the formation of FIPs and the role that FIPs play in the bulk crystallization of the polymer. We also address some features of the melting of shish-kebabs. It has been suggested that high molecular weight molecules enhance the formation of FIPs²⁶⁻²⁹. Therefore, for our investigation, we selected a linear HDPE with bimodal molecular weight distribution, synthesized via a new chemical route.

The Chapter is organized to show the transformation of FIPs into crystalline structures starting from high to low temperatures.

5.2 Experimental method

5.2.1 Material preparation

The preparation of the bimodal HDPE investigated in this Chapter is described in the material section of Chapter 4.

5.3 Characterization

5.3.1 Rheology

The linear viscoelastic properties of the bimodal HDPE blend in the melt were measured with frequency sweep experiments using an AR-G2 rheometer (TA Instruments) equipped with 8 mm disks. The experiments were performed in a N₂-rich environment after annealing the samples for 5 min at 200 °C. A strain of 1 % assured a strain-independent response (linear viscoelasticity)³⁰.

5.3.2 Small Angle X-Ray Scattering (SAXS).

Crystallization of the bimodal HDPE samples was followed at morphological scale (roughly from 10 to 100 nm) with SAXS. Time resolved experiments were performed using synchrotron radiation at the beamlines ID02 and BM26/DUBBLE of the ESRF (Grenoble, France). Two dimensional images were recorded and corrected for the transmitted beam and for the scattering of the empty sample holder. Afterwards, the scattered intensity was plotted against the modulus of the scattering vector $q = |\tilde{q}| = (4\pi/\lambda)\sin(\vartheta/2)$ where λ is the wavelength and 2ϑ the scattering angle. The spatial periodicity of polymer lamellae was estimated from the *long period* $L_p = 2\pi/q_{I_{max}}$, where $q_{I_{max}}$ is the value of q corresponding to the first maximum in the intensity profile. The integrated intensity as a function of ξ (temperature or time) is defined as $I(\xi) = \int_{q_{min}}^{q_{max}} I(q; \xi) dq$ where q_{min} and q_{max} are the minimum and maximum accessible q values, respectively. The characterization of anisotropic crystal morphologies requires the definition of three scattering regions in the azimuthal direction: the *equatorial* region, orthogonal to the chain axis; the *meridional* region parallel to the chain axis and the *diagonal* region in between the equatorial and meridional regions.

5.3.3 Wide Angle X-Ray Scattering (WAXS or WAXD).

Time resolved structural changes during crystallization were followed with high resolution WAXD at the beamline ID11 of the ESRF (Grenoble, France). Two-dimensional images were recorded and corrected for spatial distortion and for the scattering of the empty sample holder. Afterwards, the intensity was plotted against the scattering angle 2ϑ . The intensity profiles were normalized for the total scattered intensity $I_{WAXD}^{tot}(\xi) = \int_{2\vartheta_{min}}^{2\vartheta_{max}} I_{WAXD}(2\vartheta; \xi) d(2\vartheta)$. The WAXD crystallinity index X^{WAXD} was calculated after deconvolution of the intensity scattered by the amorphous (I_A) and by the crystalline phase (I_C) using standard procedures^{27, 29, 31}: $X^{WAXD} = 100 \cdot I_C / (I_C + I_A)$. After determining the angular positions 2ϑ of the scattering peaks, the Bragg distances d were calculated with Bragg's law: $n\lambda = 2d \cdot \sin\vartheta$. The unit cell parameters a and b of the orthorhombic unit cell of PE were determined according to: $a = 2d_{200}$ and $b = [(d_{110})^{-2} - (2d_{200})^{-2}]^{-1/2}$ where d_{110} and d_{200} are the Bragg distances corresponding to the 110 and 200 reflections. For oriented samples, the degree of orientation of the crystals was defined as

the Hermans' orientation factor of the c-axis: $F_H = (3\langle \cos^2 \beta_c \rangle - 1)/2$ where β is the azimuthal angle. $\langle \cos^2 \beta_c \rangle$ can be calculated using Wilchinsky's method³² from the 110 and 200 reflections: $\langle \cos^2 \beta_c \rangle = 1 - 0.565 \cdot \langle \cos^2 \beta_{200} \rangle - 1.435 \cdot \langle \cos^2 \beta_{110} \rangle$ and $\langle \cos^2 \beta \rangle = \int_0^{\pi/2} I(\beta) \cos^2 \beta \sin \beta \, d\beta / \int_0^{\pi/2} I(\beta) \sin \beta \, d\beta$. The c-axis of the crystallized molecules is parallel to the flow direction when $F_H = 1$, randomly oriented when $F_H = 0$ and orthogonal to the flow direction when $F_H = -0.5$.

5.3.4 Shear experiments

Shear experiments were performed in combination with X-ray using a Linkam Shear Cell CSS-450. To reduce unwanted scattering, the glass of the original windows of this cell was replaced by kapton. Before performing the experiments, samples (disks with thickness ~200 microns) were annealed for 3 min at 200 °C in order to erase the memory of previous thermo-mechanical histories.

5.4 Results and discussion

5.4.1 Flow induced precursors above the equilibrium melting temperature

Precursors are considered to be (partially) disordered bundles of macromolecules with typical dimensions of few nanometers. They can be formed after deformation of the melt, even at very high temperatures and, in some cases, also above the equilibrium melting temperature T_m^0 , as shown in Chapter 4. In this paragraph, we provide evidence of the formation of FIPs with shearing well above T_m^0 and we discuss their role in structure formation during cooling. The reader is reminded that, for PE, $T_m^0 = 141.2 \text{ °C}$ ³³. A pulse of shear (120 s^{-1} for 1 s), followed by cooling (10 °C/min) to room temperature, is applied to the bimodal HDPE melt at three different temperatures: 160, 200 and 240 °C. WAXD crystallinity and orientation, for these three experiments are compared with the values of a no-flow experiment in Figure 5.1.

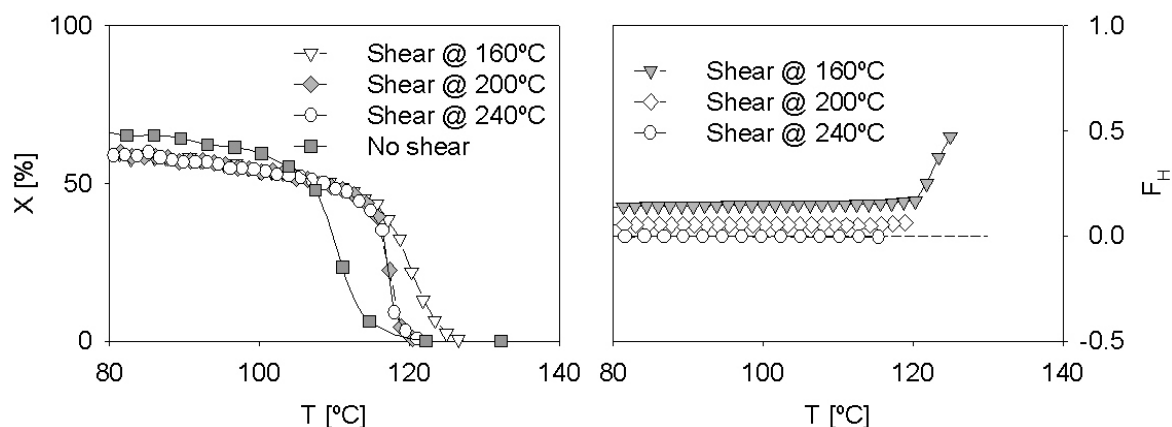


Figure 5.1: WAXD crystallinity (left) and orientation factor (right) during cooling (10 °C/min) after shear well above T_m^0 .

For the quiescent experiment the increase in crystallinity, indicating nucleation in the melt, occurs at 115 °C and isotropic structures develop. When the melt is sheared at 160 °C , nucleation occurs at higher temperature, 124 °C , with a high degree of orientation ($F_H \sim 0.5$). The high nucleation temperature together with the absence of crystallinity before nucleation suggests that shearing induces non-crystalline FIPs that act as a nucleating substrate for the rest of the molecules. The high orientation in the early stages indicates that these FIPs have a pronounced anisotropy and nucleate shish-kebabs. At lower temperatures, orientation decreases because of the nucleation of isotropic structures in the relaxed part of the melt. When shear is applied at 200 or 240 °C , because of lower relaxation times and of more demanding thermodynamical conditions, less FIPs with a more disordered structure are generated. This leads to clear distinction with shearing at 160 °C in the bulk crystallization of the melt. Nucleation occurs at a lower temperature, $\sim 119\text{ °C}$, and less oriented crystals are formed. Actually, after shearing at 240 °C , no orientation is observed although the nucleation temperature remains higher than in the no-flow case (point nucleation). The reduced ability of nucleation can be ascribed to both a reduced aspect ratio and to a lower concentration of FIPs. WAXD patterns, at two different temperatures (121 and 90 °C), corresponding to the experiments with shear at 160 , 200 and 240 °C are shown in Figure 5.2.

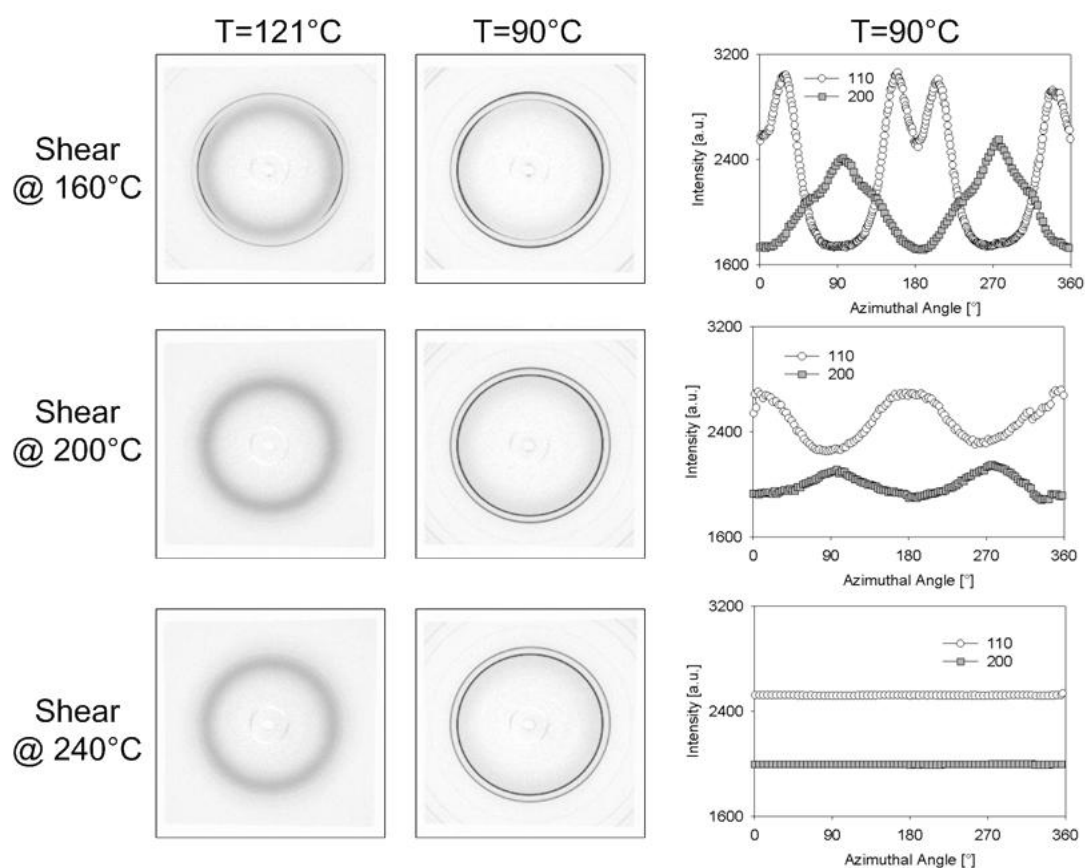


Figure 5.2: WAXD patterns at two different temperatures (left and middle) and azimuthal distributions of the intensities (right) after shear well above T_m^0 .

In all cases, the scattering fingerprint of the orthorhombic PE is clearly visible. Analysis of the azimuthal distribution of the intensity of the 110 and 200 reflections unveils interesting structural details. After shearing at 160 °C, the azimuthal offset between the maxima of the 110 and 200 reflections suggests that FIPs are overgrown by twisted kebabs (see Figure 5.3a), resembling lamellae within spherulites.

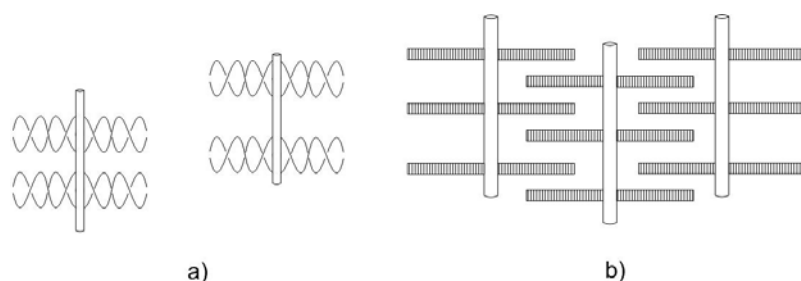


Figure 5.3: a) Shishes with twisted kebabs. b) Zip-fastener structures with interlocking of kebabs

The twist arises from tilting of the chains and it is only possible when shish kebabs are widely spaced, i.e. their concentration is low. A similar scenario is also observed after shearing at 200 °C. However, in this case it is not possible to resolve two distinct peaks around the equator ($\beta=0, 180^\circ$). When shear is applied at 240 °C, isotropic crystallization leads to uniform azimuthal distribution of the intensities. In this case, lamellae arrange in spherulites and exhibit random orientations.

5.4.2 Stable and relaxing precursors above the equilibrium melting temperature

In Chapter 4, we have seen that FIPs can crystallize and grow into shish-kebabs or dissolve in the melt depending on the conditions. Similar to a usual melting process, the dissolution of FIPs can provide information on their nature. However, most of the literature in this area focuses on the transformation from FIPs to shish-kebabs and the data available concerning dissolution and lifetime of FIPs is scarce and scattered (see Table 4.3). Because of a bimodal molecular weight distribution, the HDPE selected for the present investigation has a remarkable tendency in generating precursors under shear. This feature can be used to generate a suspension of extended chain crystals (shish) *only* with shear just above T_m^0 . In these conditions, FIPs with a folded chain structure are less stable and rapidly dissolve. In other words, approaching the melting point of the material, structure formation becomes more selective towards highly stable extended chain FIPs and the formation of kebabs is suppressed. Information on the dynamics of the precursors can be obtained from the time evolution of the SAXS equatorial intensity (I_{eq}^{SAXS}) and crystallinity (X^{WAXD}). FIPs smaller than the critical dimensions dissolve rapidly, while FIPs exceeding the critical dimensions crystallize and become stable (see Paragraph 4.3.3).

Molecules with the highest molar mass enhance the formation of FIPs. Having the longest relaxation times, they are easy to orient and stretch and retain these configurations longer than the other molecules. This may lead to the idea that shishes are mostly formed of high molar mass molecules. However, this conclusion is not confirmed by the experiments of Kornfield and coworkers³⁴ that, on the contrary, pointed out that the HMW chains are not overrepresented in the shishes. A scenario emerges where the formation of FIPs starts with a bundle of (oriented and stretched) HMW chains. This bundle propagates in the flow direction

incorporating both LMW and HMW chains. However, it seems clear that the early FIPs are HMW rich. Such a hypothesis can be verified with X-ray scattering, analyzing the time scale of the dissolution kinetics of subcritical FIPs. These bundles of chains are too small to crystallize and grow, and their development stops in the early stages, when they are HMW rich. It is reasonable to imagine that the dissolution of these small FIPs occurs with the reptation of the constituent HMW chains. An important remark is that De describes only the most probable situation. The reality is more complex²⁰; despite the high De , HMW chains can retain a random coil configuration because of entanglements with surrounding chains that are unaffected by flow.

5.4.3 Flow induced shishes below the equilibrium melting temperature: the influence of temperature

To study the effect of temperature on FIC, samples were isothermally crystallized at three different temperatures (123, 133 and 137 °C) after the application of a shear of 30 s^{-1} for 2 s at that temperature. Results are presented in Figure 5.4 and Figure 5.5.

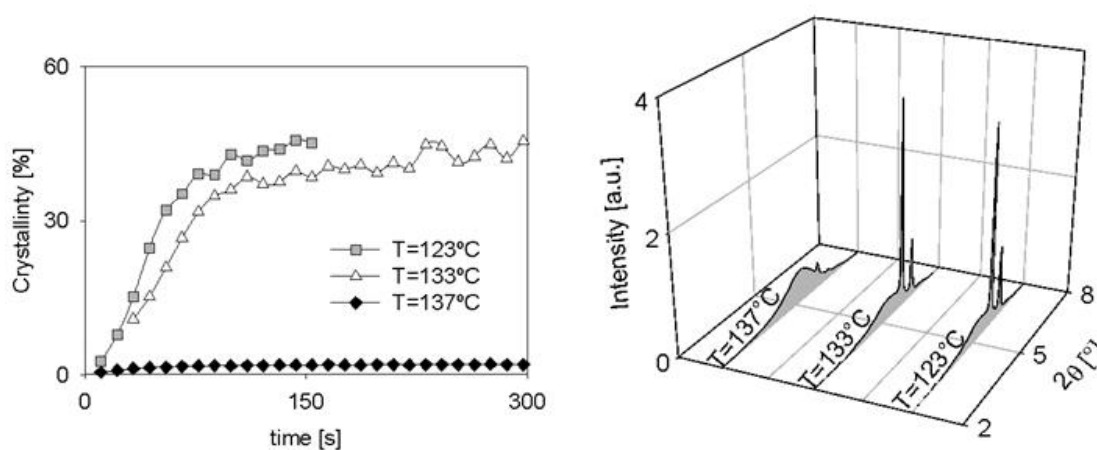


Figure 5.4: Left) WAXD crystallinity after a shear of 30 s^{-1} for 2 s at different temperatures. Right) WAXD integrated intensity as a function of the scattering angle at different temperatures at $t=140 \text{ s}$.

The critical dimensions L_{cr} and D_{cr} (Equations (4.6) and (4.7)) increase with increasing temperature (decreasing undercooling) and make nucleation more sporadic. Approaching the melting point, only rare density fluctuations can give rise to growing nuclei and this explains the dramatic drop of X^{WAXD} observed in Figure 5.4. Simultaneously, at

higher temperatures (but still below T_m^0), despite the lower De , a higher orientation develops (Figure 5.5).

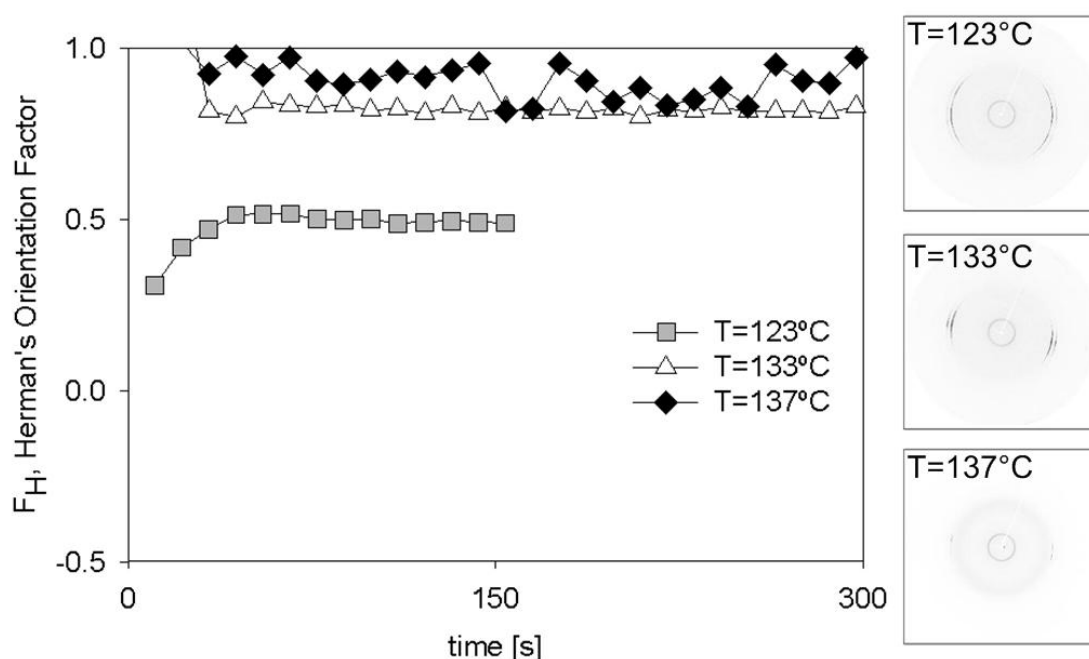


Figure 5.5: Hermans' orientation factor and selected WAXD images (at $t=140$ s) at different temperatures after a shear of 30 s^{-1} for 2 s.

This suggests that the formation of the initial bundles of HMW chains is governed by the enhanced chain mobility. The reduction of relaxation times with temperature plays a less important role. These conclusions are in line with the findings of other researchers^{6, 35, 36}. Finally, it is remarkable that the application of a shear of 30 s^{-1} for 2 s at 123, 133 and 137 °C yields always WAXD patterns (Figure 5.5) indicating the formation of straight, untwisted, kebabs (Figure 5.3b). This suggests that the distance between neighboring shish-kebabs is small (i.e. their number is high). Keller and coworkers demonstrated that, in these conditions, shish-kebabs impinge and form zip fastener structures⁹. Interlocking of kebabs in this morphology provides an extra mechanism for transferring (delocalizing) stress among neighboring chains. As a result, the mechanical properties of the material are further improved.

5.4.4 Flow induced shishes below the equilibrium melting temperature: the influence of flow conditions

The transformation of FIPs in shish-kebabs after the application of shear is studied isothermally at 137 °C, close but below the melting point. To assure a fair comparison between different flow conditions shear rate $\dot{\gamma}$ and shear time t_s are varied holding the total strain γ ($=\dot{\gamma} \cdot t_s$) constant. The experiments are performed in combination with WAXD to determine crystallinity and orientation factors and with SAXS to analyze the morphology. Some results, relevant to the discussion, are shown in Figure 5.6. For all the explored flow conditions, shish-kebabs with untwisted kebabs are formed. Apparently, shear rate is more effective than shear time in enhancing nucleation since higher shear rates corresponds to higher crystallinity. Furthermore, increasing $\dot{\gamma}$, the orientation factor increases as well. Shortly after shear, when crystallinity is very low (less than 1 %), an equatorial streak of intensity in SAXS suggests the formation of FIPs with a high degree of anisotropy. Some of them immediately crystallize and are overgrown by stacks of lamellae (kebabs) that give rise to meridional lobes in the SAXS. When the lamellar overgrowth takes place, the crystallinity raises accordingly, until a steady state is reached. As shown by the lines in Figure 5.6, the time dependence of the crystallinity is well described by the following kinetic equation:

$$X^{WAXD}(t) = X_0 \cdot [1 - \exp(-t / \lambda)] \quad (5.1)$$

X_0 is crystallinity at the steady state and λ is a characteristic time. The values of X_0 and λ , obtained fitting (5.1) to the data, are reported in Table 5.1 together with the De numbers for HMW chains. Both the increase of X_0 and the decrease of λ with the flow rate are a consequence of the flow enhanced nucleation rate. In fact, flow promotes nucleation and more nuclei fill the space in a shorter time span. For all flow conditions, De_{or}^{HMW} is always much higher than unity and indicates a prominent orientation of HMW molecules. In addition, when De_s^{HMW} approaches unity an equatorial streak in the SAXS indicates the formation of shishes. Besides the degree of crystal orientation, also other details of the morphology are affected by the flow. For instance, after 300 s, the average long period L_p is 88 nm for a shear of 60 s⁻¹ for 1s while it decreases to 81 nm for a shear of 15 s⁻¹ for 4 s suggesting the formation of thinner crystals in the latter case.

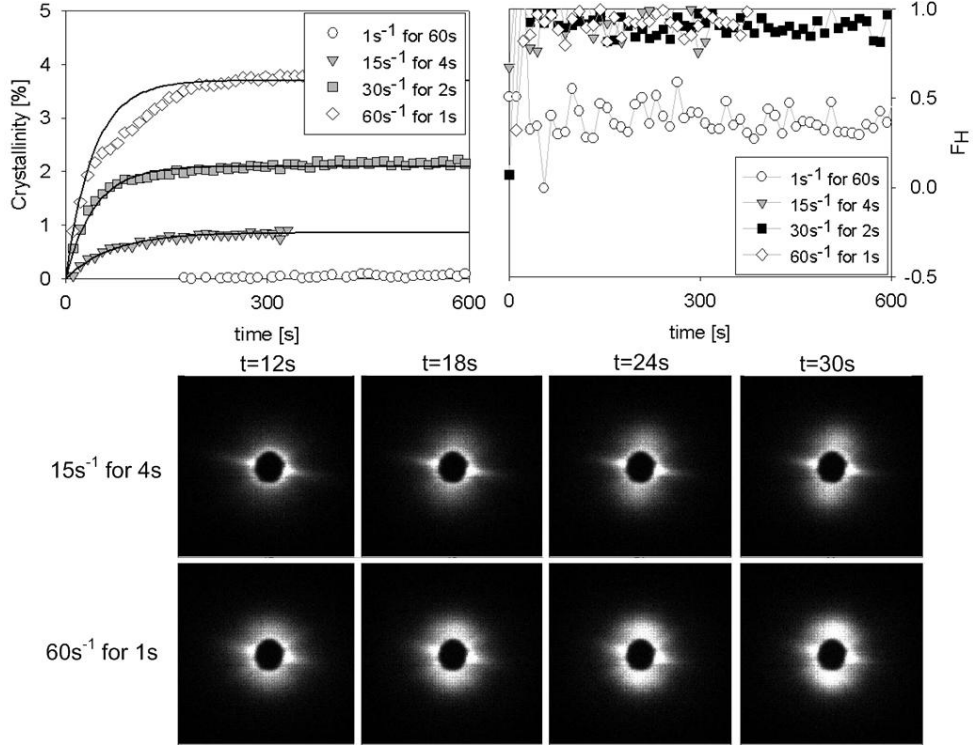


Figure 5.6: Top) WAXD crystallinity and orientation as a function of time at 137 °C after a shear with 60 strain units. Bottom) Selected SAXS images corresponding to the experiments shown on top.

Table 5.1: Deborah numbers for HMW molecules and fit parameters for the Equation (5.1) at 137 °C.

	HMW De_s	HMW De_o	X_0 [%]	λ [s]
$1s^{-1} / 60s$	0.04	170	0.06	>100s
$15s^{-1} / 4s$	0.68	2500	0.86	67.8
$30s^{-1} / 2s$	1.37	5000	2.1	42.8
$60s^{-1} / 1s$	2.73	10000	3.7	41

Similar to what is observed at 142 °C, with the formation of needle-like FIPs, I_{eq}^{SAXS} rises quickly to a maximum and then decreases (see Figure 5.7). However, in this case the drop of I_{eq}^{SAXS} is relatively small and does not correlate with τ_D^{HMW} . Due to the lower temperature, the early FIPs are more stable than at 142°C and their lifetimes $t_{FIP}^* \gg \tau_D^{HMW}$. Moreover, the drop of I_{eq}^{SAXS} could also be (partially) explained with the presence of the kebabs that decrease the density fluctuation between the shishes and the melt.

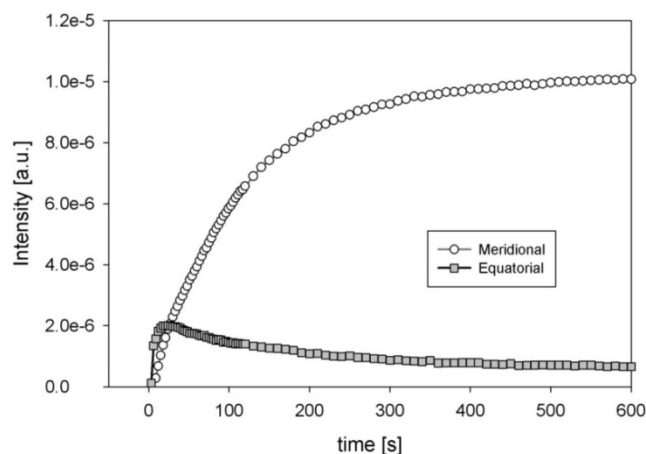


Figure 5.7: Integrated meridional and equatorial SAXS intensities at 137 °C after a shear of 15 s^{-1} for 4 s.

5.4.5 Separating shish creation from the kebab crystallization

We are now going to show how shishes nucleate the bulk of the polymer. In Chapter 4, the formation of crystalline shishes with shear flow at 142 °C is discussed. Just like nucleating agents, shishes generated at this high temperature can be used as a heterogeneous substrate for the nucleation of the rest of the molecules at a lower temperature. An exact lattice matching and a good state of dispersion make shishes the perfect nucleating agent. In this paragraph, we discuss the increase in the crystallization temperature and the changes in the morphology induced by shishes generated with shear at 142 °C. Different flow conditions are investigated and the cooling starts immediately after flow. Figure 5.8 shows SAXS images taken at 142 °C shortly after the application of shear. The corresponding De number for HMW molecules are given in Table 5.2. The scattering fingerprint of needle-like FIPs and shishes is clear, independently of shear rate, when $\gamma=100$. In all the other cases, in the accessible q range, no changes are observed in the scattering patterns immediately after flow.

Table 5.2: Deborah numbers for HMW chains in shear at 142 °C.

	2 s^{-1}	5 s^{-1}	10 s^{-1}	25 s^{-1}	50 s^{-1}	100 s^{-1}
HMW De_s	0.07	0.2	0.4	0.9	1.8	3.5
HMW De_0	260	650	1300	3250	6500	13000

The scattering patterns of Figure 5.9 suggest the presence of a threshold strain γ_{\min} for shish formation. Below γ_{\min} , regardless of $\dot{\gamma}$, the stretch ratio of the HMW molecules would be insufficient to form shishes. This idea is consistent with the findings of van Meerveld et al.³⁷. However, the absence of an equatorial streak in SAXS does not, necessarily, imply the absence of FIPs and shishes. The equatorial streak is absent also when the concentration of FIPs and shishes is (too) low. This is proven, during cooling, by the growth of lamellae (kebabs) with a high degree of orientation (see Figure 5.9), suggesting the presence of an anisotropic nucleating substrate (FIPs or shishes). According to the simulations of Frenkel and coworkers¹⁹, even a single stretched molecule can nucleate parallel lamellae. Surprisingly, in the range of conditions explored in this Chapter, the overall degree of lamellar orientation is found to depend mainly on γ . Very similar orientations are observed at a given γ , independently of $\dot{\gamma}$. While, much more pronounced differences are observed varying γ (or varying t_s) at a given $\dot{\gamma}$. Figure 5.9 demonstrates that the influence of shear flow on PE morphology is substantial and can be dramatic in some cases. For instance, at $\gamma=100$, starting from $\dot{\gamma} = 25 \text{ s}^{-1}$, isotropic scattering is hardly detectable. For these conditions, all lamellae grow with the c-axis parallel to the shishes (i.e. parallel to the flow direction) yielding a very high level of anisotropy. The emergence of a second order reflection at the meridian of SAXS (see patterns in Figure 5.9) indicates that kebabs are distributed along the flow direction with high regularity. At room temperature, their spacing is 23 nm. Morphology evolution during bulk crystallization is discussed for the case of cooling after a pulse of 100 s^{-1} for 1 s at 142 °C, see Figure 5.10. At high temperature, the SAXS equatorial intensity is higher than the meridian and diagonal due to the scattering of FIPs and shishes. During cooling, L_{cr} and D_{cr} become smaller and, small FIPs, bound to dissolve at 142 °C, can crystallize (*thermal* nucleation) increasing the equatorial intensity. Simultaneously, also the meridian intensity increases but, no maximum can be observed in the intensity profile above $T \cong 130^\circ\text{C}$, suggesting uncorrelated objects in the melt. In other words, because of thermal nucleation, small (point-like) FIPs are transformed in stable nuclei. These small FIPs can tumble during shear and, therefore, have random orientations. Moreover, the orientation of these small FIPs is lost already at a relatively small lateral growth.

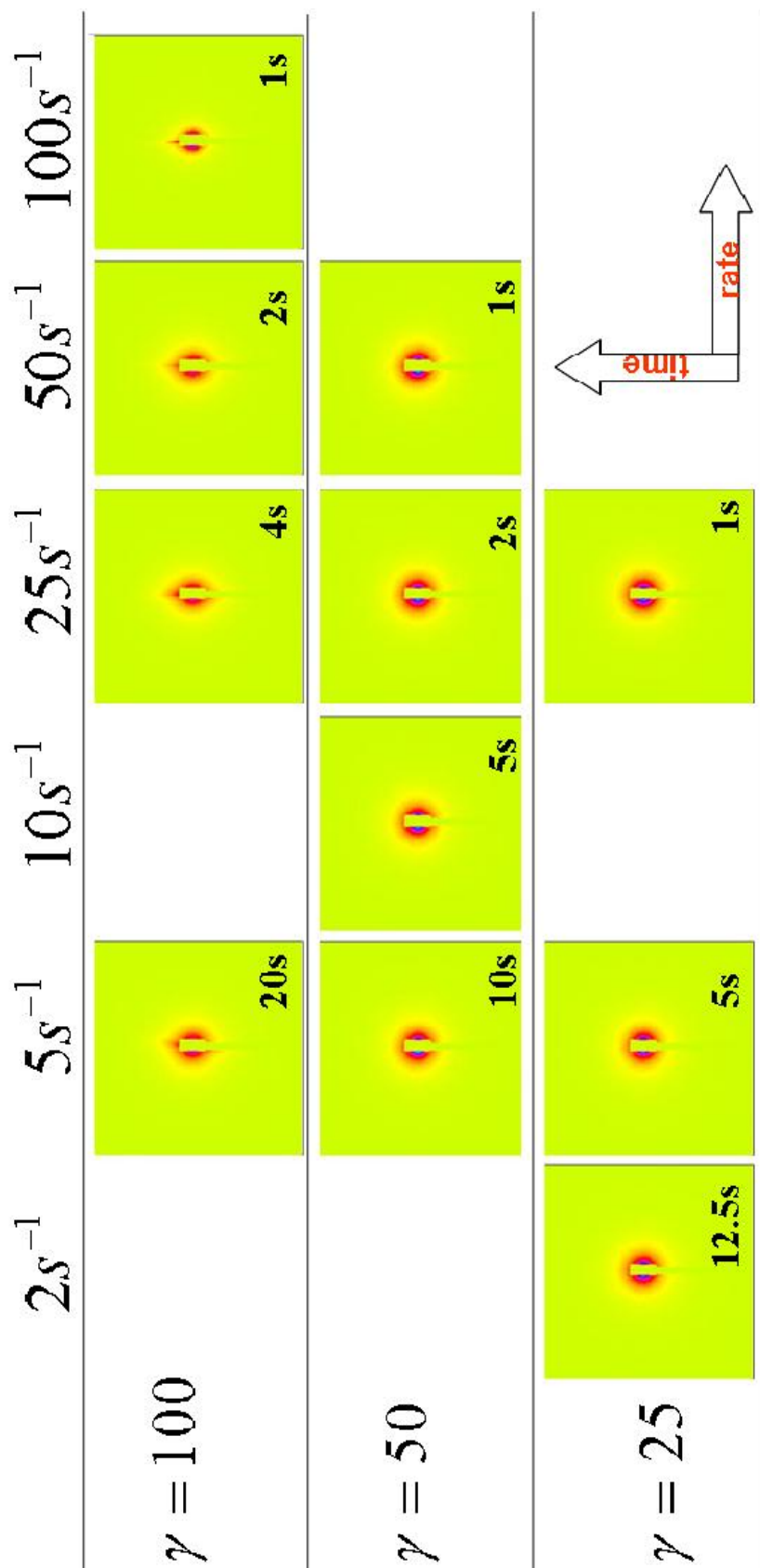


Figure 5.8: SAXS images few seconds after the application of shear at 142 °C. The flow direction is horizontal. The shear time is indicated in each image.

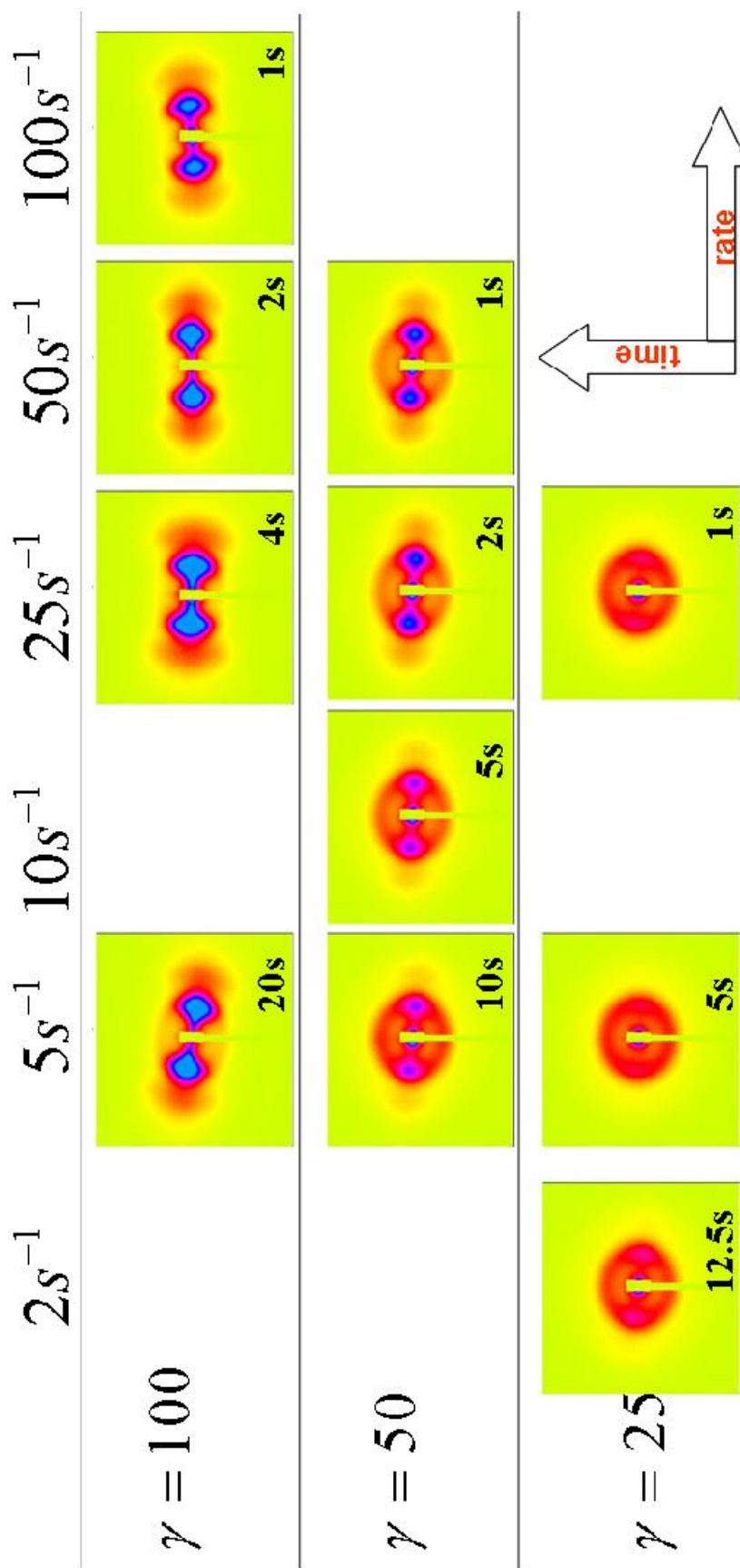


Figure 5.9: SAXS images at room temperature after the application of shear at 142 °C. The flow direction is horizontal. The shear time is indicated in each image.

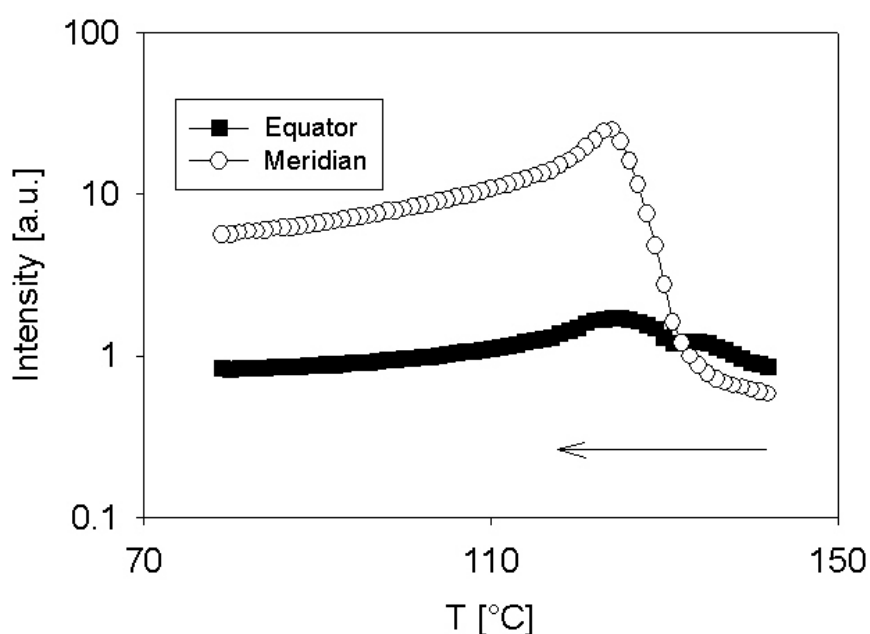


Figure 5.10: SAXS equatorial and meridional integrated intensities as a function of temperature after shear at 142 °C (cooling rate is 5 °C/min).

At $T \cong 133$ °C, large scale (secondary) nucleation starts. First, the heterogeneous nucleation of kebabs on the surface of shishes causes an increase in $I_{\text{mer}}^{\text{SAXS}}$ and, next, at lower temperatures, some isotropic nucleation in the bulk of the sample causes an increase in $I_{\text{eq}}^{\text{SAXS}}$ as well. Particularly interesting is the case of mixed morphologies where spherulites coexist with shish-kebabs. In these cases, it is possible to distinguish between the high temperature nucleation of kebabs from the low temperature nucleation of spherulites. An example is the experiment shown in Figure 5.11 (cooling after 10 s^{-1} for 5 s at 142 °C).

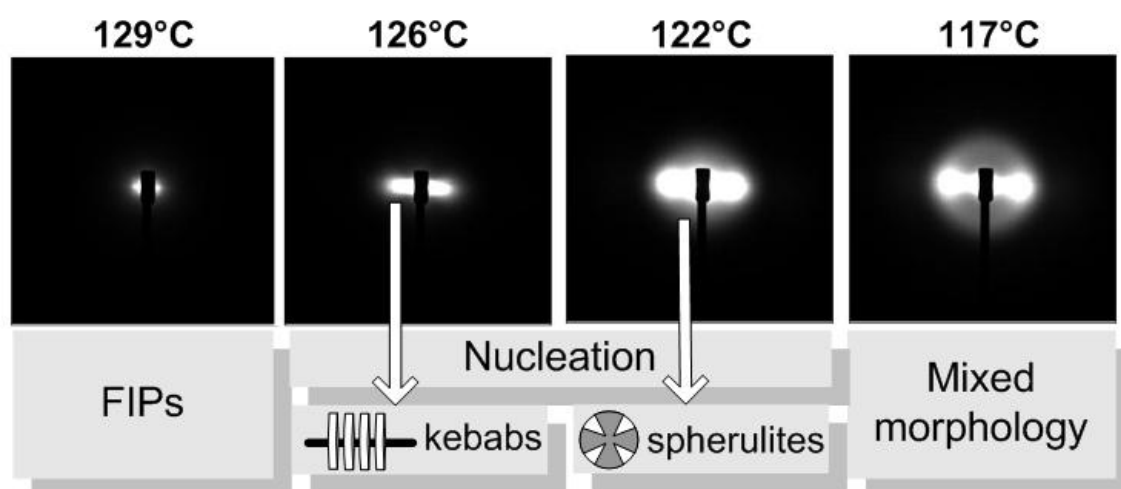


Figure 5.11: Salient SAXS images during crystallization on cooling after shear at 142 °C.

5.4.6 Crystallization onset temperature after short term shear

As for nucleating agents, the nucleation ability of shishes can be estimated comparing the temperatures where heterogeneous nucleation occurs during cooling. We found that the onset temperature of the kebabs $T_{\text{onset}}^{\text{K}}$ depends on the flow conditions at 142 °C. For the flow conditions described in the previous paragraph, $T_{\text{onset}}^{\text{K}}$ varies from ~125 °C to ~132 °C, as reported in Figure 5.12.

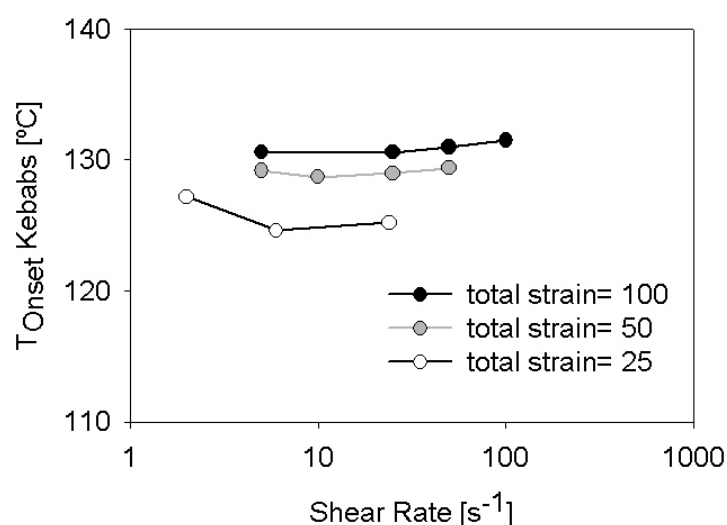


Figure 5.12: Onset temperature for the nucleation of kebabs on cooling (5 °C/min) after shear at 142 °C.

Similar to the morphological orientation, $T_{\text{onset}}^{\text{K}}$ depends mostly on γ rather than on $\dot{\gamma}$ and on t_s . Consistent with the SAXS data, $T_{\text{onset}}^{\text{K}}$ exhibits the highest values at $\gamma=100$, where a large amount of shishes (~0.4 %) is formed, and the lowest values at $\gamma=25$, where less shishes are formed. The nucleating ability of a substrate can be seen as the product between the quality (efficiency) of the nucleation sites and their number. The quality of nucleation sites is given by matching of the lattice parameters of the substrate and the crystallizing polymer (epitaxy)³⁸⁻⁴¹ and, in this case, is not an issue because of the common unit cell of shishes and kebabs. In addition, it seems reasonable to assume that epitaxy matching does not depend on the flow conditions. In contrast, the quantity of the nucleation sites is determined by aspect ratio ($\propto 1/D_{\text{shish}}$) and concentration of the shishes and both depend on the flow conditions. The individual effects are difficult to separate because a better nucleation ability (higher values of $T_{\text{onset}}^{\text{K}}$) is associated with more nucleation sites that can be achieved both at

the same concentration increasing the aspect ratio and with the same aspect ratio increasing the concentration.

5.4.7 Melting of shish kebabs

Heterogeneous crystallization of kebabs on shishes yields a well organized and oriented morphology. Because of the high nucleation temperature, kebabs grow thicker than ordinary lamellae. For these reasons shish-kebabs exhibit an enhanced thermal stability. To illustrate the melting of shish kebabs, Figure 5.13 shows SAXS intensities as a function of the temperature during heating of a sample crystallized after a shear of 100 s^{-1} for 1 s at $142 \text{ }^\circ\text{C}$.

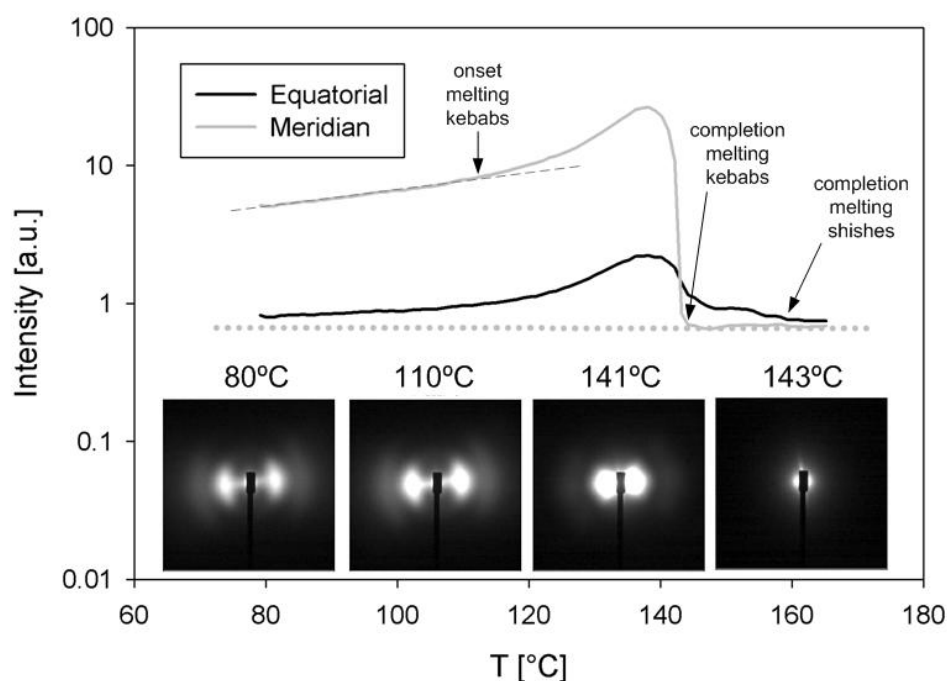


Figure 5.13: SAXS equatorial and meridional integrated intensities as a function of temperature heating a sample with fully oriented morphology crystallized on cooling after a shear of $100 \text{ s}^{-1}/1\text{s}$ at $142 \text{ }^\circ\text{C}$.

At $\sim 115 \text{ }^\circ\text{C}$, melting of the kebabs (folded chain crystals) starts and it is completed abruptly when they are superheated to $\sim 142 \text{ }^\circ\text{C}$. Shishes, with their extended chain structure, are more stable than spherulites and melt gradually, surviving up to $\sim 157 \text{ }^\circ\text{C}$. Interestingly, immediately after melting of the kebabs, the scattering fingerprint of shishes becomes again visible in the SAXS. This indicates that, if the temperature is not too high, shishes generated with shear at $142 \text{ }^\circ\text{C}$ retain their morphology after melting the kebabs. This behavior is

similar to that of some nucleating agents. Kebabs that can melt leaving intact the shishes were already observed and termed *macrokebabs* by Keller³. During cooling, after heating up to 148 °C, high temperature nucleation of kebabs is still observed, see Figure 5.14.

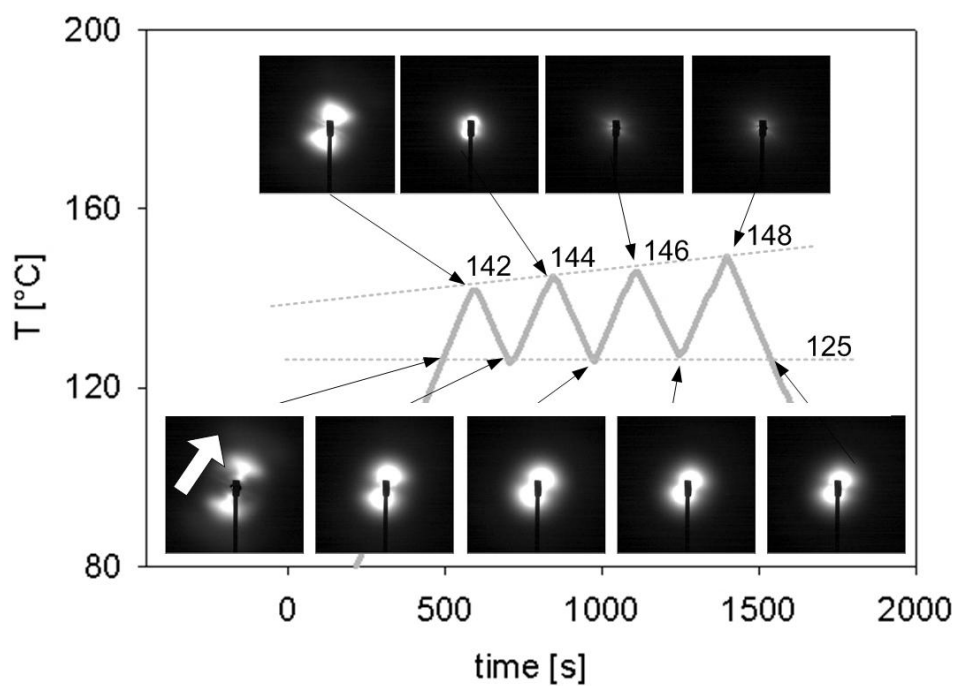


Figure 5.14: SAXS images during heating and cooling runs around the melting point of the material.

This suggests that melting of the shishes begins with losing order at small length scales. As a consequence, chain stretch rapidly vanishes and disrupts the structure of the shishes. However, as suggested by some rheological observations⁴², the long range order, on the length scale of the whole molecule, can still be retained. Apparently, the long lasting orientation of HMW chains is sufficient for the epitaxial nucleation of kebabs. On heating from room temperature, independently of the shear history at 142 °C, kebabs always melt at ~ 142 °C, i.e. a few degrees higher than spherulites do. In this respect, it is interesting to follow the melting of a sample with a mixed morphology. For instance, Figure 5.15 reports SAXS images of the melting of a sample crystallized after a shear of 5 s^{-1} for 10 s at 142 °C.

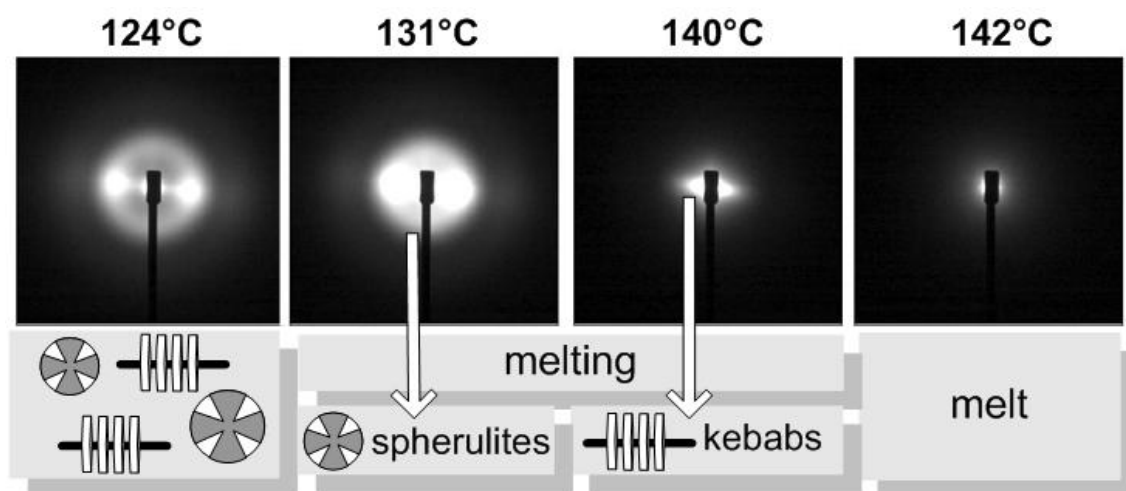


Figure 5.15: Sequence of SAXS images describing morphological changes during melting of a sample with a fully oriented morphology.

At low temperatures, this sample shows a morphology that is a combination of oriented and isotropic distributed lamellae suggesting the coexistence of shish kebabs and spherulites. Upon heating, the isotropic scattering coming from spherulites disappears first at 140 °C. The meridional lobes coming from kebabs disappear later, at 142 °C. Shishes were not observed in SAXS during the crystallization of this sample and correspondingly are not observed on heating after melting of the kebabs.

5.5 Conclusions

In this Chapter, we studied the mechanism of formation and melting of shish kebabs in a sheared bimodal HDPE melt. The results indicate that flow induced precursors (FIPs) play a crucial role in structural and morphological developments during crystallization. FIPs are metastable structures with very low or no crystallinity that arise with stretching of the longest chains in the melt. FIPs can be formed at temperatures surprisingly high compared with T_m^0 and, depending on the conditions, can grow into crystals or dissolve in the melt. When FIPs are formed at very high temperatures, for instance 160 or 200 °C, they are undetectable with SAXS and WAXD but still show strong influence on the crystallization of the polymer. On cooling, FIPs increase the nucleation temperature and promote orientation at structural and morphological levels. The formation of needle-like FIPs and shishes demands stretch of the HMW chains. But this is not the only requirement. Shearing at 142 °C, we

found that the total strain plays a clear role. It seems that a critical strain should be exceeded to obtain a large quantity of shishes. On cooling, needle-like FIPs and shishes formed at 142 °C act as nucleating agents. They can raise the nucleation temperature to up 132 °C and template the morphology of the polymer. With time resolved SAXS, it is possible to differentiate between the high temperature epitaxial nucleation of kebabs and the nucleation of lamellae randomly assembled in spherulites, at lower temperatures. We observe that ~0.4 % of shishes is sufficient to produce a fully oriented morphology on cooling. Such a conclusion is consistent with our findings on iPP melts containing fibrils formed from the nucleating agent DMDBS where a similar small amount (~0.5 wt%) of pre-aligned DMDBS fibrils is sufficient to induce, on cooling, a fully oriented polymer morphology.

Shish kebabs obtained on cooling after shear at 142 °C are well organized and this gives them an enhanced thermal stability. At morphological level, melting is a sequence of events symmetrical to crystallization. In fully oriented morphologies, kebabs melt before shishes and yield again SAXS patterns with equatorial scattering only. In mixed morphologies, spherulites melt before kebabs and, similar to the crystallization process, no equatorial scattering is observed.

In this Chapter, the transformation of FIPs into extended chain crystals and the nucleating ability of these crystals is addressed. FIPs are partially disordered bundles of molecules with undetectable crystallinity. In fast short term shear, a question arises whether FIPs are generated during or after cessation of flow. In the following Chapter, an attempt has been made to answer this question.

5.6 References

1. Schrauwen, B. A. G.; Breemen, L. C. A. v.; Spoelstra, A. B.; Govaert, L. E.; Peters, G. W. M.; Meijer, H. E. H. *Macromolecules* **2004**, *37*, 8618-8633.
2. Gahleitner, M.; Wolfschwenger, J.; Bachner, C.; Bernreitner, K.; Neißl, W. *Journal of Applied Polymer Science* **1996**, *61*, 649-657.
3. Keller, A.; Kolnaar, H. W. H., *Flow induced orientation and structure formation*. VCH: New York, **1997**; Vol. 18.
4. Meijer, H. E. H.; Govaert, L. E. *Prog. Polym. Sci.* **2005**, *30*, 915-938.
5. Ward, I. M.; Sweeney, J., *An introduction to the mechanical properties of solid polymers*. John Wiley & Sons: Weinheim, **2004**.

6. Kumaraswamy, G.; Issaian, A. M.; Kornfield, J. A. *Macromolecules* **1999**, 32, 7537-7547.
7. Janeschitz-Kriegl, H.; Ratajski, E.; Stadlbauer, M. *Rheol Acta* **2003**, 42, 355.
8. Devaux, N.; Monasse, B.; Haudin, J. M.; Moldenaers, P.; Vermant, J. *Rheol. Acta* **2004**, 43, 210-222.
9. Bashir, Z.; Odell, J. A.; Keller, A. *Journal of Materials Science* **1984**, 19, 3713-3725.
10. Hill, M. J.; Barham, P. J.; Keller, A. *Colloid & Polymer Sci.* **1980**, 258, 1023-1037.
11. Barham, P. J.; Keller, A. *Journal of Materials Science* **1985**, 20, 2281-2302.
12. Hsiao, B. S.; Yang, L.; Somani, R. H.; Avila-Orta, C. A.; Zhu, L. *Physical Review Letters* **2005**, 94, 117802.
13. Smith, P.; Lemstra, P. J.; Pijpers, J. P. L.; Kiel, A. M. *Colloid & Polymer Sci.* **1981**, 259, 1070-1080.
14. Hsieh, Y.; Ju, J. *Journal of Applied Polymer Science* **1994**, 53, 347-354.
15. Loos, J.; Schimanski, T.; Hofman, J.; Peijs, T.; Lemstra, P. J. *Polymer* **2001**, 42, 3827-3834.
16. Liu, T.; Lieberwirth, I.; Petermann, J. *Macromol. Chem. Phys.* **2001**, 202, (14), 2921-2925.
17. Pennings, J.; Kiel, A. M. *Kolloid ZZ Polym* **1965**, 205, 160.
18. Binsbergen, F. L. *Nature* **1966**, 211, 516-517.
19. Hu, W.; Frenkel, D.; Mathot, V. B. F. *Macromolecules* **2002**, 35, 7172-7174.
20. Dukovski, I.; Muthukumar, M. *Journal of Chemical Physics* **2003**, 118, (14), 6648-6655.
21. Keum, J. K.; Burger, C.; Zuo, F.; Hsiao, B. S. *Polymer* **2007**, 48, 4511-4519.
22. Zuo, F.; Keum, J. K.; Yang, L.; Somani, R. H.; Hsiao, B. S. *Macromolecules* **2006**, 39, 2209-2218.
23. Kumaraswamy, G.; Kornfield, J. A.; Yeh, F.; Hsiao, B. S. *Macromolecules* **2002**, 35, 1762-1769.
24. Ogino, Y.; Fukushima, H.; Matsuba, G.; Takahashi, N.; Nishida, K.; Kanaya, T. *Polymer* **2006**, 47, 5669-5677.
25. Keum, J. K.; Zuo, F.; Hsiao, B. S. *Journal of Applied Crystallography* **2007**, 40, 48-51.
26. Seki, M.; Thurman, D. W.; Oberhauser, J. P.; Kornfield, J. A. *Macromolecules* **2002**, 35, 2583-2594.
27. Nogales, A.; Hsiao, B. S.; Somani, R. H.; Srinivas, S.; Tsou, A. H.; Balta-Calleja, F. J.; Ezquerro, T. *Polymer* **2001**, 42, 5247-5256.
28. Yang, L.; Somani, R. H.; Sics, I.; Hsiao, B. S.; Kolb, R.; Lohse, D. *J. Phys. Condens. Matter* **2006**, 18, 2421-2436.
29. Yang, L.; Somani, R. H.; Sics, I.; Hsiao, B. S.; Kolb, R.; Fruitwala, H.; Ong, C. *Macromolecules* **2004**, 37, 4845-4859.
30. Macosko, C., *Rheology : principles, measurements, and applications*. VCH: Weinheim, **1994**.
31. Balta-Calleja, F. J.; Vonk, C. G., *X-ray scattering of synthetic polymers*. Elsevier: Amsterdam, **1989**.
32. Wilchinsky, Z. W., *Advances in X-ray analysis*. **1962**; Vol. 6.
33. Wunderlich, B., *Thermal analysis of polymeric materials*. Springer-Verlag: Berlin, **2005**.
34. Kimata, S.; Sakurai, T.; Nozue, Y.; Kasahara, T.; Yamaguchi, N.; Karino, T.; Shibayama, M.; Kornfield, J. A. *Science* **2007**, 316, (5827), 1014 - 1017.
35. Coppola, S.; Balzano, L.; Gioffredi, E.; Maffettone, P. L.; Grizzuti, N. *Polymer* **2004**, 45, 3249-3256.

36. Somani, R. H.; Yang, L.; Hsiao, B. S. *Physica A* **2002**, 304, 145-157.
37. van Meerveld, J.; Peters, G. W. M.; Hutter, M. *Rheol Acta* **2004**, 44, 119-134.
38. Wittmann, J. C.; Lotz, B. *J. Polym. Sci., Polym. Phys. Ed.* **1981**, 19, 1837.
39. Thierry, A.; Straupe, C.; J., W.; Lotz, B. *Macromol Symp* **2006**, 241, 103-110.
40. Fillon, B.; Thierry, A.; Lotz, B.; Wittmann, J. C. *Journal of Thermal Analysis* **1994**, 42, 721-731.
41. Lotz, B.; Wittmann, J. C. *J. Polym. Sci., Polym. Phys. Ed.* **1986**, 24, 1559.
42. Bent, J.; Hutchings, L. R.; Richards, R. W.; Gough, T.; Spares, R.; Coates, P. D.; Grillo, I.; Harlen, O. G.; Read, D. J.; Graham, R. S.; Likhtman, A. E.; Groves, D. J.; Nicholson, T. M.; McLeish, T. C. B. *Science* **2003**, 19, 1691 - 1695.

Chapter 6*

Metastable structures *during* fast short term shear

The goal of this Chapter is to study the crystallization of isotactic polypropylene (iPP) during and immediately after a strong pulse of shear (i.e. with a high Deborah number) on the undercooled melt. This is possible using high flux synchrotron X-ray scattering (SAXS and WAXD) that allows for a high frame rate (3 frames/s) maintaining a good signal to noise ratio. We found that shear rate is the dominating parameter for structure formation during shear. When the shear rate is high enough, crystals with a high degree of orientation in the shear direction can be formed already during shear. In contrast, for lower shear rates, no crystalline structures were observed during shear. However, SAXS shows an equatorial streak indicating needle-like scatterers aligned with the flow direction. These scatterers are metastable precursors of crystallization. Although these precursors are not crystalline in the early stages, they crystallize after cessation of the flow and template the nucleation of lamellae with c-axis parallel to the flow direction (shish-kebab morphology).

6.1 Introduction

Bulk crystallinity¹⁻⁵ affects many of the physical properties of semicrystalline polymeric materials⁶⁻¹². Universal rules are difficult to establish as these materials exhibit a processing-property relation, i.e. the final properties of the material are affected by the processing conditions. Temperature history and, especially, flow alter the crystallization behavior. Flow can increase the crystallization rate by decades compared to quiescent conditions¹³⁻¹⁸ and, in addition, the crystalline morphology can change dramatically¹⁹⁻²⁴. In quiescent or quasi-quiescent conditions morphology is dominated by spherulites²⁵, three dimensional assemblies of randomly oriented folded chain lamellae. For strong enough flows, spherulites are replaced by shish-kebabs, composite crystallites with an extended chain fibrillar core (shish) dressed with disk-like folded chain lamellae (kebabs)²⁶⁻³². The origin of

* Partially reproduced from: L. Balzano et al. 'Metastable structures during fast short term shear', *Macromolecules* **2008** (Submitted)

this morphology is the topic of a long standing discussion^{31, 33-37} that begun in the 1960s. In Chapters 4 and 5, some of the classic ideas are combined with new observations, to propose a mechanism for the formation of shish-kebabs that starts with stretch of the longest chains and passes through metastable precursors with undetectable crystallinity. In short term shear, after cessation of the flow, a selection takes place among the precursors. Those exceeding some critical dimension transform into crystalline structures, the remainder dissolve back into the melt state. The ratio between crystallizing and dissolving precursors and the rate of crystallization and dissolution are determined by the temperature. A real competition between crystallization and dissolution of flow induced precursors (FIPs) can be observed only at high enough temperatures. For instance, in the case of polyethylene (PE), it is necessary to be in proximity to or even above the equilibrium melting point T_m^0 ($T_m^0|_{PE} = 141.2 \text{ }^\circ\text{C}$). Although there is no undercooling ΔT , this does not contradict thermodynamics. In fact, flow raises the effective melting temperature by reducing the entropy and, thus, generates the undercooling ΔT_f that is indispensable for nucleation^{13, 38}. At lower temperatures, the driving force due to flow contribute to make most of the precursors stable from the moment of their creation³³. Here, dissolution is absent or limited to a small fraction of precursors.

In many of the experiments available in literature, the study of FIPs is based on short term flow protocols^{33, 39-44} where, a pulse of flow is applied for few seconds, and the evolution of the system is studied after cessation of the flow. In this scenario, some questions arise: when are actually FIPs created and when do they crystallize? During or after cessation of the flow? Reminding that FIPs are disordered bundles of molecules held together only by weak interaction forces, another question that arises is: are these interaction forces strong enough to prevent flow from destroying FIPs and allow them to crystallize during flow? Giving answers to these questions is the aim of this Chapter.

In a short term flow protocol, flow lasts, typically, only for few seconds and this restricts the sampling time to a fraction of a second. For this reason, our investigation demands the use of synchrotron X-ray scattering with a high flux of photons. The material investigated is isotactic polypropylene (iPP).

6.2 Materials and methods

6.2.1 Materials

The polymer used in this work is a commercial homopolymer grade of isotactic polypropylene (iPP). The material, labeled 15M10, was obtained by DSM (Geleen, The Netherlands) and contained no other additives than stabilizers. The specifications of the material are reported in Table 6.1.

Table 6.1: Specification of the iPP used in this work.

Material	M_w [kg/mol]	M_w/M_n	[%mmmm]	T_m [°C]
15M10	350	5.6	96.2	161

6.2.2 X-ray characterization

Small angle X-ray scattering (SAXS) was performed at the beamline ID02 of the European Synchrotron Radiation Facility (ESRF, Grenoble). The samples were irradiated with a wavelength $\lambda=0.995 \text{ \AA}$ and two dimensional images were recorded using a Frelon detector, with a resolution of 1024x1024 pixels and a pixel size of 164 μm , placed at 6.5 m from the sample. After subtraction of the scattering of the empty sample holder, images were integrated to obtain the scattered intensity (I) as a function of the modulus of the scattering vector $q=(4\pi/\lambda)\sin(\theta/2)$ where 2θ is the scattering angle^{45, 46}. The total intensity I^{SAXS} as a function of time was obtained integrating $I(q)$ over the whole accessible q range:

$$I^{SAXS}(t) = \int_{q_{\min}}^{q_{\max}} I(q;t) dq .$$

Wide angle X-ray scattering (WAXS or WAXD) was performed at the beamline ID11 of the ESRF. Experiments were carried out with a wavelength $\lambda=0.508 \text{ \AA}$ and a sample to detector distance of about 32cm. The images were recorded with a two dimensional Frelon detector with a resolution of 512x512 pixels (pixel size $\cong 190 \mu\text{m}$). After correction for spatial

distortions and scattering of the empty sample holder, the images were integrated to obtain the intensity distribution I as a function of the scattering angle 2θ . These one-dimensional profiles were used to calculate crystallinity. For this purpose, the scattering of the amorphous component (I_A) underneath crystalline peaks (I_C) was approximated with a straight line (see Figure 6.1).

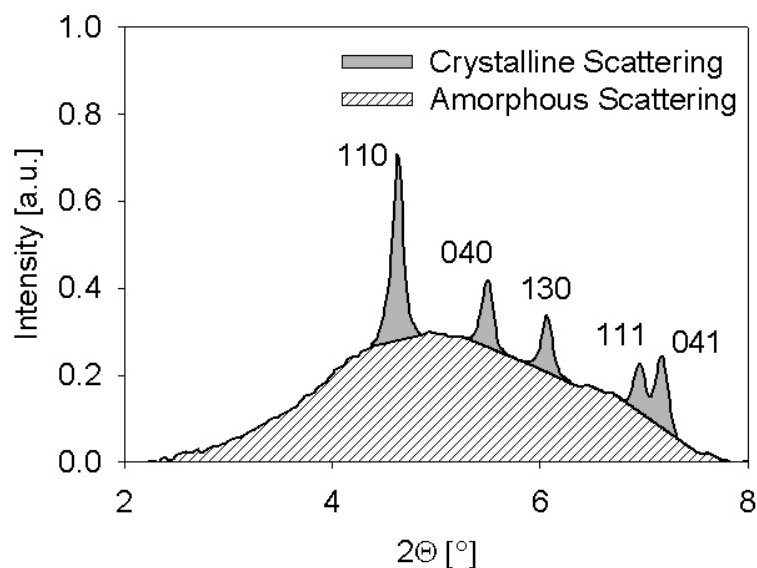


Figure 6.1: Example of the procedure to separate crystalline and amorphous scattering. The Miller indices of the scattering reflections are indicated as well.

This simplified procedure is expected to give trustworthy results at low crystallinities (up to $\sim 15\%$)⁴⁷. Crystallinity (x) was determined as:

$$x = 100 \cdot \frac{I_C}{I_C + I_A} \quad (6.1)$$

WAXD data were also used for calculating the Hermans' orientation factors F_H of the crystalline c-axis:

$$F_H = \frac{3\langle \cos^2 \beta \rangle - 1}{2} \quad (6.2)$$

where β is the azimuthal angle. For iPP, where a $00l$ reflection is not observed, $\langle \cos^2 \beta \rangle$ can be obtained with Wilchinsky's formula⁴⁸. Using geometrical relations, the orientation of the c-axis is calculated from the orientation of the 110 and 040 crystal planes:

$$\langle \cos^2 \beta \rangle = 1 - 0.901 \langle \cos^2 \beta_{040} \rangle - 1.099 \langle \cos^2 \beta_{110} \rangle \quad (6.3)$$

with the definition:

$$\langle \cos^2 \beta \rangle = \frac{\int_0^{\pi/2} I(\beta) \cdot \cos^2 \beta \cdot \sin \beta \cdot d\beta}{\int_0^{\pi/2} I(\beta) \cdot \sin \beta \cdot d\beta} \quad (6.4)$$

6.2.3 Shear experiments

Shear experiments were performed in combination with SAXS and WAXD using a Linkam CSS-450 Shear Cell where, to avoid unwanted scattering, the original glass plates were replaced with kapton. The setup is shown in Figure 6.2.

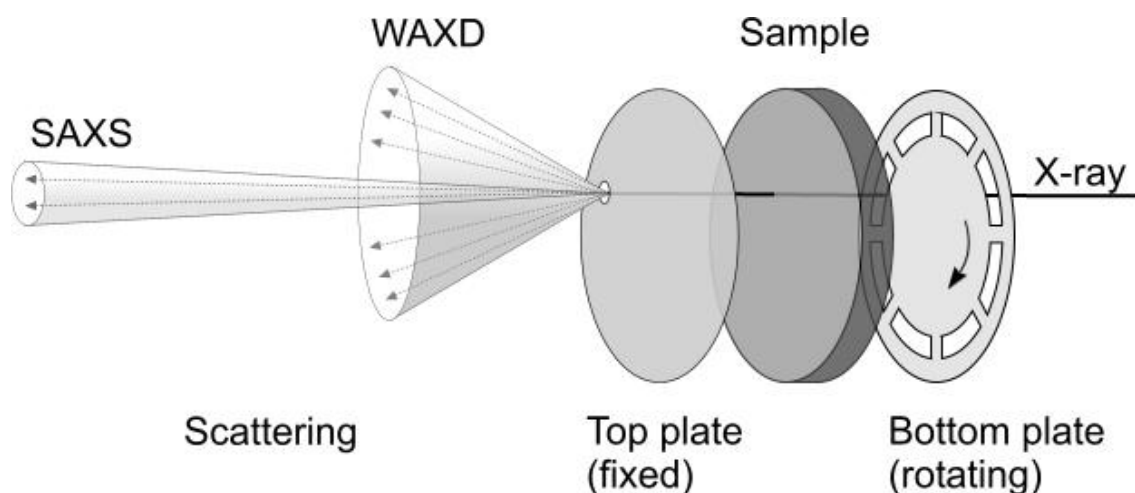


Figure 6.2: Schematic drawing of the shear device.

When shearing, a metal spoke of the rotating plate lies periodically in front of the incoming beam, the corresponding (dark) scattering images are discarded from analysis.

6.3 Results and Discussion

6.3.1 Flow conditions in short term shear

It is well established that shear flow promotes orientation and stretch of polymer molecules in the melt^{23, 24, 49-51}. If τ_D and τ_s are the relaxation times for orientation (disengagement time) and stretch (chain retraction time) of the longest molecules, orientation of these molecules is achieved when the Deborah number for orientation $De_o = \tau_D \dot{\gamma}$ exceeds unity and stretch when the Deborah number for stretch $De_s = \tau_s \dot{\gamma}$ exceeds unity⁴⁹. The ratio τ_D / τ_s is similar to the number of entanglements per chain Z ⁵²⁻⁵⁴. For the iPP under consideration, $Z \cong 100$ and, therefore, $De_o \cong 100 De_s$. In other words, chain orientation is attained at shear rates nearly two decades lower than chain stretch. In this Chapter, we aim to look at crystallization under shear conditions providing orientation and stretch to the molecules, therefore, our experimental conditions are chosen such that $De_s \gg 1$. A high De_o is consequently achieved as well.

A useful way to study the flow induced crystallization (FIC) of a polymer melt is short term shear. In this experiment, after annealing at high temperature, the melt is brought to the desired test temperature where shear is applied for a limited time, typically few seconds, and the subsequent crystallization of the polymer is observed in absence of flow. By choosing a short shear time it is hoped that flow effects are separated from crystallization effects, i.e. no noticeable material changes occur during the flow and thus the ‘normal’ rheological behavior can be used to characterize the flow strength (De_o and De_s). The flow conditions are determined by three parameters: temperature, shear rate ($\dot{\gamma}$) and shear time (t_s). Once these are assigned, the total strain ($\gamma = \dot{\gamma} \cdot t_s$) is also fixed. A fair comparison between different experiments is possible only when holding γ constant.

6.3.2 Flow induced precursors during short term shear

To generate FIPs, we select shear conditions with a relatively high strain value, $\gamma = 180$. This allows for spanning a broad range flow conditions, from relatively slow and long to relatively fast and short. FIPs originate from stretching of the longest chains in the melt^{23, 28, 41, 44, 55}, therefore we restrict $\dot{\gamma}$ such as $De_s \gg 1$. For the iPP considered, $\tau_D \cong 100$ s and $\tau_s \cong 1$ s at 145 °C⁵⁶. Therefore, shear rates of 60 s⁻¹, 90 s⁻¹ and 180 s⁻¹ suite our experimental requirements. The shear time is varied accordingly to keep the total strain $\gamma = 180$. Table 6.2 gives an overview of the selected shear conditions. WAXD patterns acquired at a rate of 3 frames/s during and immediately after short term shear at 145 °C are shown in Figure 6.4. In these figures, as in the rest of the Chapter, the time $t=0$ corresponds to cessation of the flow. During flow ($t < 0$), the level of crystallinity is always relatively low (< 2 %) and, therefore, reflections from crystals are difficult to identify. As we expect strongly oriented structures that lead to arching of the reflections, only the equatorial region is shown. This enhances the visibility.

Table 6.2: Deborah numbers for the experiments of Figure 6.6.

	De_o	De_s
60 s ⁻¹ /3 s	$6 \cdot 10^3$	60
90 s ⁻¹ /2 s	$9 \cdot 10^3$	90
180 s ⁻¹ /1 s	$1.8 \cdot 10^4$	180

For a shear of 60 s⁻¹/3s, no scattering from crystalline structures is detected during shear. In contrast, for the higher shear rates, the scattering fingerprint of crystalline iPP structures is visible already during shear. For 90 s⁻¹/2s, arched 110 and 040 reflections are observed. Such a scattering pattern is associated to iPP crystals with a high degree of orientation in the flow direction⁵⁷⁻⁵⁹. Further analysis indicates that the level of crystallinity during flow reaches ~ 0.1 %. A similar situation is observed for 180 s⁻¹/1s. In this case, arching

is even stronger than $90\text{s}^{-1}/2\text{s}$. The 110 reflection looks like a spot and the 040 (normally less intense than 110) is hardly visible. Crystallinity during flow reaches nearly 2 %.

Summarizing, it is demonstrated that, when the flow rate is strong enough, crystalline structures (presumably shishes) can be formed already during a short term flow. The intermolecular forces within these crystals are high enough to avoid destruction by shearing.

To investigate the dynamics of metastable FIPs during shear, the experiment $60\text{s}^{-1}/3\text{s}$ is studied in more detail. During shear, WAXD suggests the absence of crystalline structures. However, SAXS patterns, see Figure 6.3, show an equatorial streak that indicates the presence of needle-like scatterers aligned with flow⁶⁰. These needle-like structures, with no crystallinity, are indeed FIPs that are formed as a consequence of molecular stretching ($De_s \gg 1$). As revealed by the appearance of SAXS meridional lobes, after cessation of the flow, FIPs start crystallizing and serve as a heterogeneous substrate for the nucleation of stack of lamellae with c-axis parallel to the flow direction.

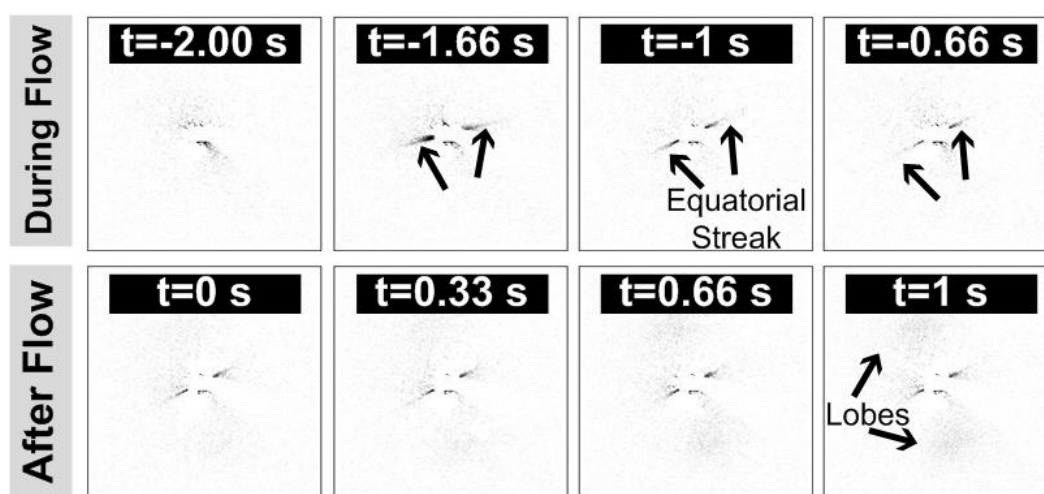


Figure 6.3: SAXS patterns during and immediately after short term shear at $145\text{ }^{\circ}\text{C}$ with $60\text{s}^{-1}/3\text{s}$.

6.3.3 Crystallization after short term shear.

After cessation of shear ($t=0$), samples are allowed to crystallize isothermally at $145\text{ }^{\circ}\text{C}$. Figure 6.5 reports the SAXS intensities in the equatorial (I_{Eq}^{SAXS}) and meridional (I_{Mer}^{SAXS})

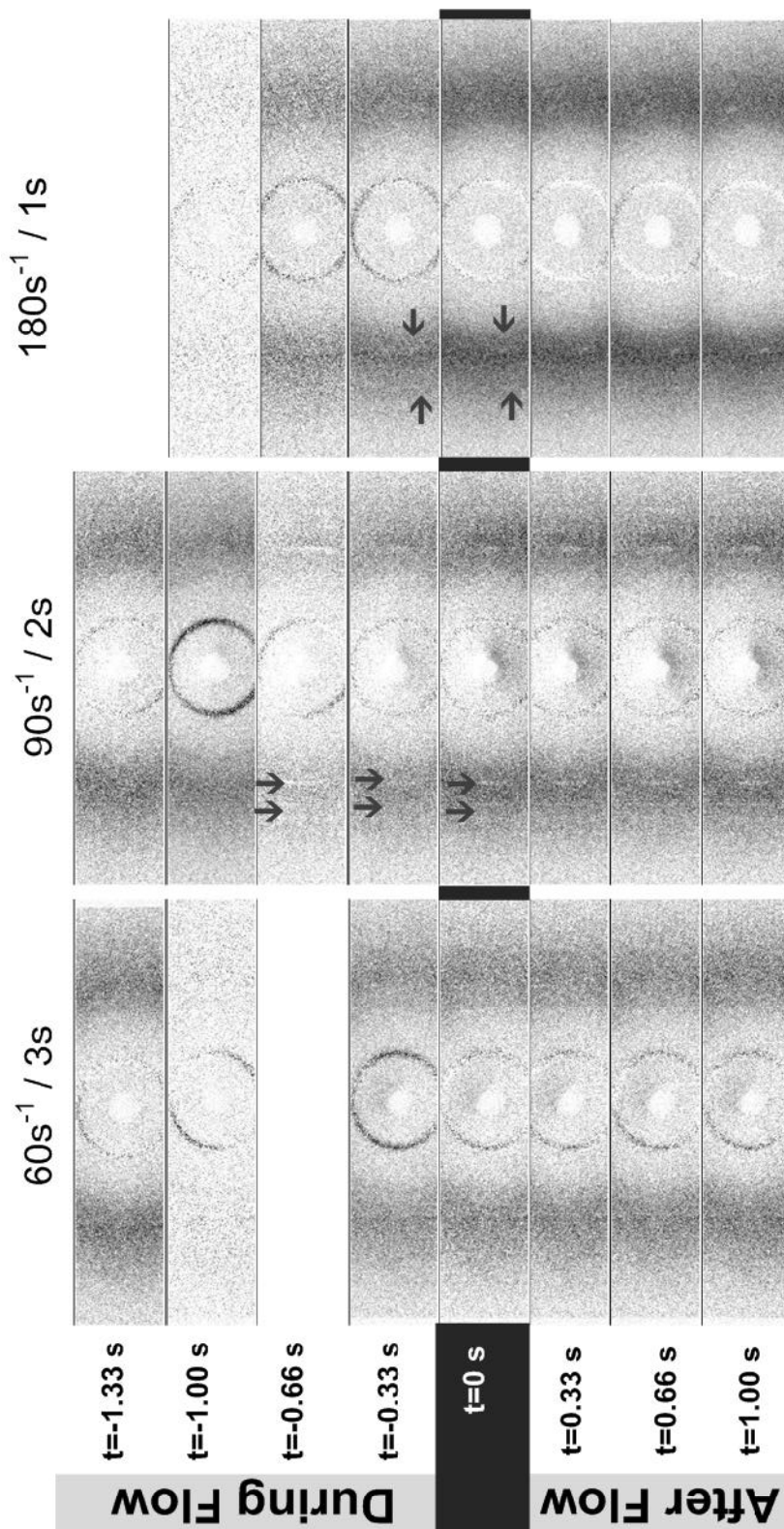


Figure 6.4: Equatorial region of WAXD patterns during and after short term shear at $145\text{ }^{\circ}\text{C}$ with $\gamma=180$. Flow direction is vertical. The arrows indicate arched crystalline reflections.

regions for the experiment $60s^{-1}/3s$. At the beginning, I_{Eq}^{SAXS} is much higher than I_{Mer}^{SAXS} because of the equatorial streak coming from needle like FIPs. However, while I_{Eq}^{SAXS} remains nearly constant, I_{Mer}^{SAXS} grows quickly and after few seconds the situation is reversed, i.e. $I_{Mer}^{SAXS} > I_{Eq}^{SAXS}$. The growth of I_{Mer}^{SAXS} is a consequence of the onset of meridional lobes associated with the decoration of shishes and FIPs with stacks of lamellae (kebabs) with the c-axis oriented with the flow direction. The formation of a similar shish-kebab morphology is observed also for $90s^{-1}/2s$ and $180s^{-1}/1s$ after cessation of flow.

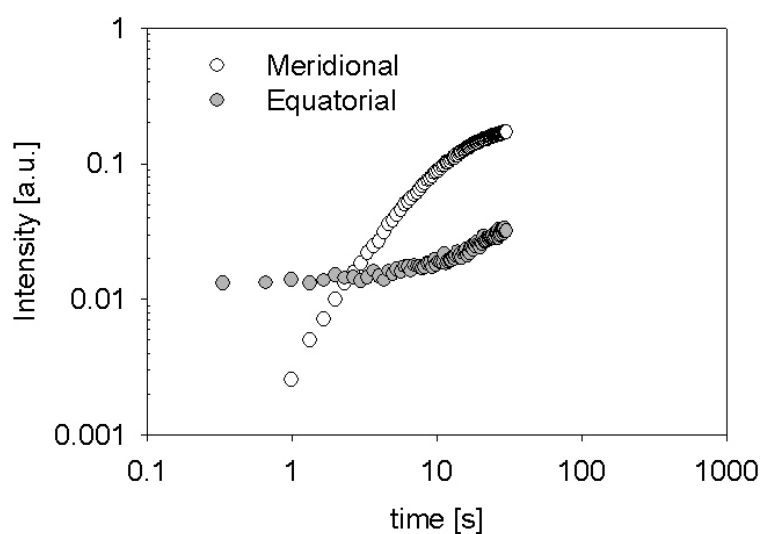


Figure 6.5: SAXS meridional and equatorial intensities at 145 °C as a function of time after the application of shear ($60s^{-1}/3s$).

As shown in Figure 6.6, the growth of kebabs raises the crystallinity and, simultaneously, the crystalline orientation factors (Figure 6.7) tend to decrease. This can be explained with the homogeneous nucleation of randomly oriented lamellae in the bulk of the sample and/or with bending of the kebabs after a certain diameter is exceeded (see Figure 6.8)⁶¹. In the experiments $90s^{-1}/2s$ and $180s^{-1}/1s$, where crystallization is observed already during shear, the orientation is significantly higher than in $60s^{-1}/3s$. As expected, the data of Figure 6.6 indicate that an increase in $\dot{\gamma}$ is more efficient to enhance both nucleation and orientation than an increase in t_s .

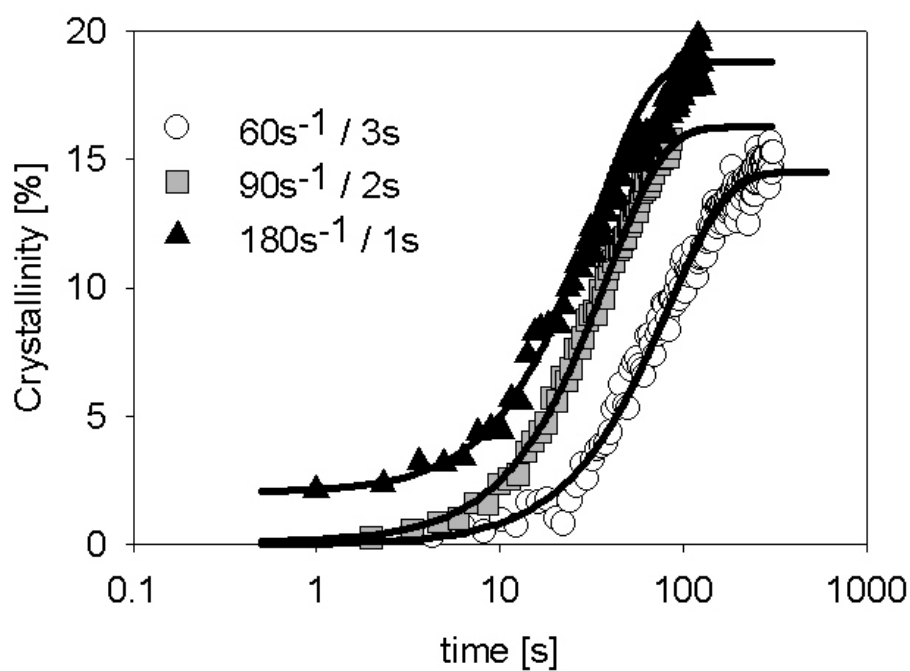


Figure 6.6: Crystallinity developing at 145 °C after the application of 180 strain units.

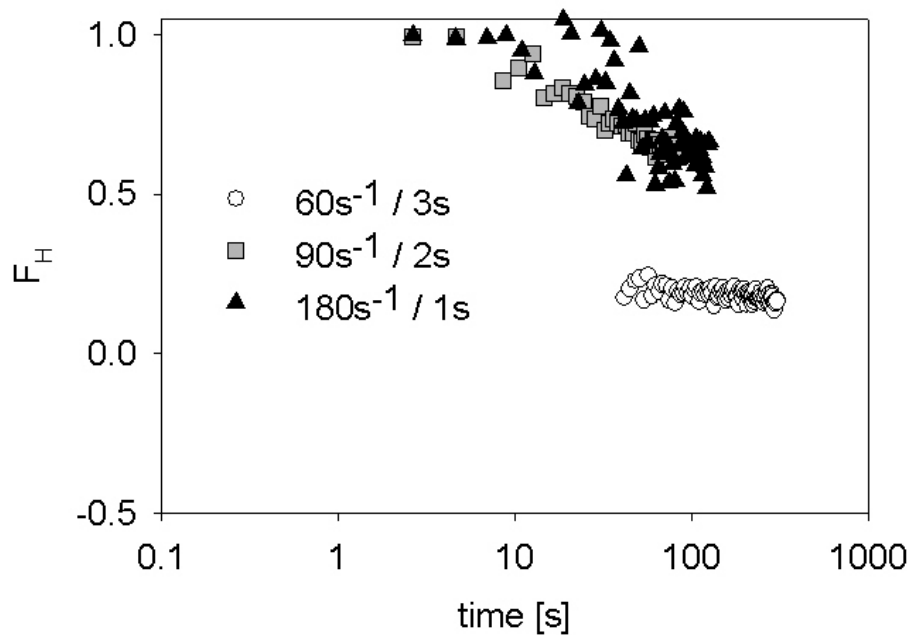


Figure 6.7: Orientation developing at 145 °C after the application of 180 strain units.

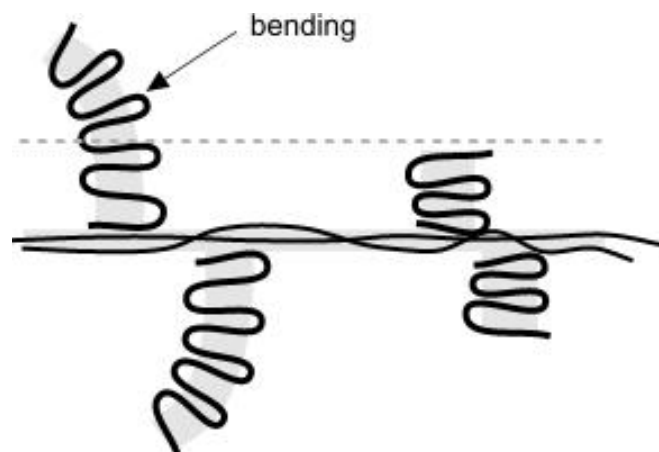


Figure 6.8: Bending of kebab occurring after a certain diameter is exceeded.

More details on structure formation immediately after cessation of shear can be obtained defining a degree of space filling after flow:

$$\Phi(t) = \frac{x(t) - x_0}{x_\infty - x_0} \quad (6.5)$$

x_0 is the crystallinity already present at the time $t=0$ and, therefore, generated during flow, while, x_∞ is the saturation level for the crystallinity, attained at long times. Note that the definition (6.5) is based on the assumption that, at long times, a complete space filling ($\Phi=1$) is attained despite the relatively low degree of crystallinity (x_∞). $\Phi(t)$ can be described with the Avrami equation⁶²⁻⁶⁴:

$$\Phi(t) = 1 - \exp(-kt^n) \quad (6.6)$$

where k is a rate constant and n the Avrami exponent that indicates the geometry of the growing crystallites. Equation (6.6) can be re-written as:

$$\text{Ln}\{-\text{Ln}[1 - \Phi(t)]\} = \text{Ln}(k) + n \cdot \text{Ln}(t) \quad (6.7)$$

In the early stages, $\text{Ln}\{-\text{Ln}[1 - \Phi(t)]\}$ as a function of $\text{Ln}(t)$ (the so called Avrami plot) is a straight line with slope n . The Avrami plot, for the crystallization following the cessation of the shear, is shown in Figure 6.9. Fitting Equation (6.7) on the data yields the parameters given in Table 6.3.

Table 6.3: Parameters used for fitting Equation (6.6) onto crystallization data of Figure 6.6.

	x_∞ [%]	x_0 [%]	n	k [s^{-n}]
$60\text{ s}^{-1}/3\text{ s}$	14.5	0	1.34	$2.70 \cdot 10^{-3}$
$90\text{ s}^{-1}/2\text{ s}$	16.2	0.1	1.37	$6.78 \cdot 10^{-3}$
$180\text{ s}^{-1}/1\text{ s}$	18.8	2	1.38	$8.20 \cdot 10^{-3}$

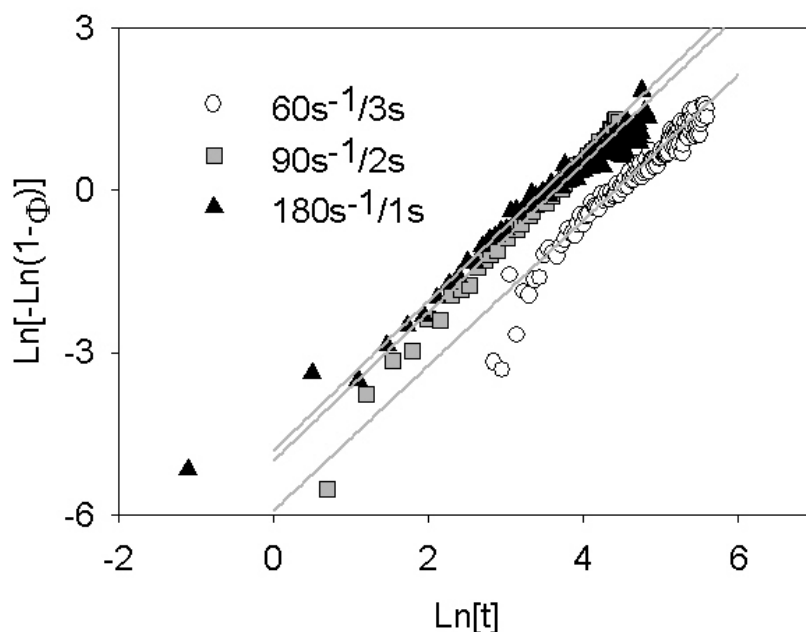


Figure 6.9: Avrami plot constructed with crystallinity data after short term shear at 145 °C.

Independent of the flow conditions, $n \cong 1.36 \pm 0.02$ indicates that, in all cases, space filling occurs because of the athermal growth of circular lamellae (kebabs). The only difference is the rate constant k that increases with $\dot{\gamma}$, in line with the increased number of kebabs at higher shear rates and consistent with an increased number of shishes as well. Combining equations (6.5) and (6.6), it is possible to obtain a description of the crystallinity as a function of time:

$$x(t) = x_0 + (x_\infty - x_0) \left[1 - \exp(-kt^n) \right] \quad (6.8)$$

As expected, using the fitting parameters given in Table 6.3, a good agreement with the measured data is found (lines in Figure 6.6). Some remarkable observations emerge from this analysis:

- After a short term shear, a good description of the crystallization kinetics can be obtained with the Avrami equation. To this end, it is necessary to define the space filling $\Phi(t)$ accounting for the crystallinity generated already during flow (x_0 in Equation (6.5)). Although this value can be very small, it has large influence in the early stages. Furthermore, a complete space filling at long times needs to be hypothesized, despite the relatively low crystallinity.
- The data of Figure 6.6 seem to indicate the presence of an ‘induction time’ for the growth of kebabs, even for $180\text{s}^{-1}/1\text{s}$ where a crystallinity of 2 % is attained already during flow. However, although in all experiments there is a clear characteristic time at which x starts increasing massively, this induction period should not be considered as a time where structure formation is frozen-in. Figure 6.9 indicates that, in all cases, starting from the first measurement ($t=0.3\text{ s}$), major changes take place in the space filling.
- At long times, in isothermal conditions, crystallinity saturates to a plateau level (x_∞) that depends on the flow conditions. Higher $\dot{\gamma}$ yield higher final crystallinity. This behavior can be interpreted in terms of driving force for crystallization, i.e. in terms of Gibbs free energy (G) difference between the melt and the crystal. Flow increases the free energy of the melt generating more driving force for nucleation (see Figure 6.10).

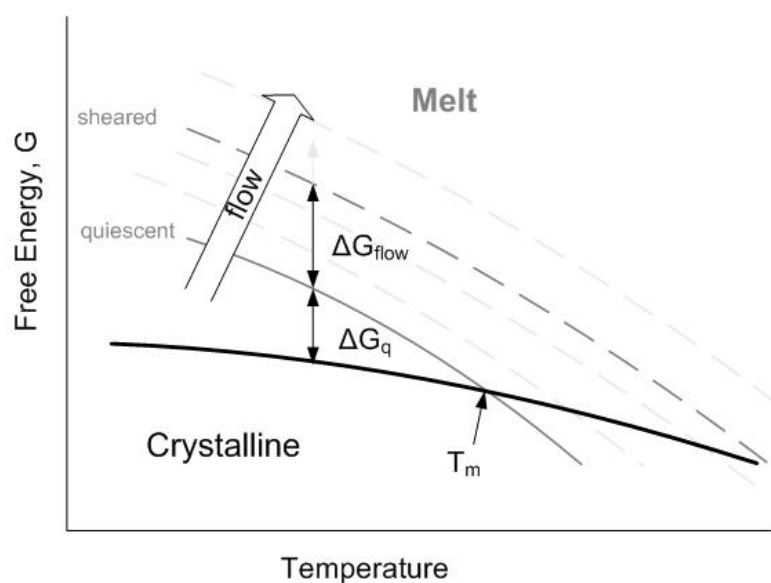


Figure 6.10: Effect of flow on the free energy.

6.4 Conclusions

We studied the early stages of the flow induced crystallization of iPP, during and immediately after the application of a strong (high De) shear pulse. At 145 °C, with a total strain $\gamma = 180$, X-ray scattering data (SAXS and WAXD) suggest that shear rate is the dominant parameter for structure development during flow. When the shear rate is high enough ($> 90 \text{ s}^{-1}$) crystalline structures can be formed already during shear. In these conditions, WAXD suggests the presence of crystallinities up to 2% and a high degree of orientation of the crystals with the flow direction. In contrast, at lower shear rates (for instance 60 s^{-1}) no sign of crystalline structures is observed during shear. However, simultaneously, SAXS indicates the presence of needle like scatterers aligned with the shear direction. As soon as the flow stops, the crystalline or non-crystalline structures generated during shear act as a nucleating substrate for the heterogeneous formation of kebabs. The crystalline morphology is, thus, strongly tied with the structures present in the early stages.

6.5 References

1. Strobl, G., *The physics of polymers*. Springer: Berlin, **1997**.
2. Wunderlich, B., *Thermal analysis of polymeric materials*. Springer-Verlag: Berlin, **2005**.
3. Keller, A. *Phyl. Mag.* **1957**, 2, 1171.
4. Lotz, B. *Journal of Macromolecular Science, Part B-Physics* **2002**, B41, 685-709.
5. Natta, G. *J. Polym. Sci.* **1955**, 16, 143.
6. Schrauwen, B. A. G.; Breemen, L. C. A. v.; Spoelstra, A. B.; Govaert, L. E.; Peters, G. W. M.; Meijer, H. E. H. *Macromolecules* **2004**, 37, 8618-8633.
7. Kristiansen, M.; Werner, M.; Tervoort, T.; Smith, P.; Blomehofer, M.; Schmidt, H. W. *Macromolecules* **2003**, (36), 5150-5156.
8. Smith, P.; Lemstra, P. J. *Journal of Materials Science* **1980**, 15, 505-514.
9. Baastiansen, C. W. M., *Oriented structures based on flexible polymers*. PhD thesis, Eindhoven University of Technology: **1991**.
10. Govaert, L. E., *Deformation behavior of oriented polyethylene fibers*. PhD thesis, Eindhoven University of Technology: **1990**.
11. Meer, D. W. v. d.; Pukanszky, B.; Vancso, G. J. *J. Macromol. Sci.-Phys.* **2002**, 41, 1105-1119.
12. Bashir, Z.; Odell, J. A.; Keller, A. *Journal of Materials Science* **1984**, 19, 3713-3725.
13. Coppola, S.; Balzano, L.; Gioffredi, E.; Maffettone, P. L.; Grizzuti, N. *Polymer* **2004**, 45, 3249-3256.
14. Lagasse, R. R.; Maxwell, B. *Polym. Eng. Sci.* **1976**, 16, 189.
15. Heeley, E. L.; Morgovan, A.; Bras, W.; Dolbnya, I. P.; Gleeson, A. J.; Ryan, A. J. *Phys. Chem. Comm.* **2002**, 5, 158-160.

16. Kumaraswamy, G.; Kornfield, J. A.; Yeh, F.; Hsiao, B. S. *Macromolecules* **2002**, *35*, 1762-1769.
17. Nogales, A.; Hsiao, B. S.; Somani, R. H.; Srinivas, S.; Tsou, A. H.; Balta-Calleja, F. J.; Ezquerro, T. *Polymer* **2001**, *42*, 5247-5256.
18. Devaux, N.; Monasse, B.; Haudin, J. M.; Moldenaers, P.; Vermant, J. *Rheol. Acta* **2004**, *43*, 210-222.
19. Keller, A.; Kolnaar, H. W. H., *Flow induced orientation and structure formation*. VCH: New York, **1997**; Vol. 18.
20. Hsiao, B. S.; Yang, L.; Somani, R. H.; Avila-Orta, C. A.; Zhu, L. *Physical Review Letters* **2005**, *94*, 117802.
21. Hobbs, J. K.; Humphris, A. D. L.; Miles, M. J. *Macromolecules* **2001**, *34*, 5508-5519.
22. Sakellarides, S. L.; McHugh, A. J. *Rheol Acta* **1987**, *26*, 64-77.
23. Seki, M.; Thurman, D. W.; Oberhauser, J. P.; Kornfield, J. A. *Macromolecules* **2002**, *35*, 2583-2594.
24. Somani, R. H.; Hsiao, B. S.; Nogales, A.; Srinivas, S.; Tsou, A. H.; Sics, I.; Balta-Calleja, F. J.; Ezquerro, T. A. *Macromolecules* **2000**, *33*, 9385-9394.
25. Basset, D. C.; Franck, F. C.; Keller, A. *Phyl Trans Roy Soc London A* **1994**, *348*, 29-43.
26. Binsbergen, F. L. *Nature* **1966**, *211*, 516-517.
27. Pennings, J.; Kiel, A. M. *Kolloid ZZ Polym* **1965**, *205*, 160.
28. Ogino, Y.; Fukushima, H.; Matsuba, G.; Takahashi, N.; Nishida, K.; Kanaya, T. *Polymer* **2006**, *47*, 5669-5677.
29. Wang, Z. G.; Hsiao, B. S.; Sirota, E. B.; Srinivas, S. *Polymer* **2000**, *41*, 8825-8832.
30. Yamazaki, S.; Watanabe, K.; Okada, K.; Yamada, K.; Tagashira, K.; Toda, A.; Hikosaka, M. *Polymer* **2005**, *46*, 1685-1692.
31. Kimata, S.; Sakurai, T.; Nozue, Y.; Kasahara, T.; Yamaguchi, N.; Karino, T.; Shibayama, M.; Kornfield, J. A. *Science* **2007**, *316*, (5827), 1014 - 1017.
32. Hill, M. J.; Barham, P. J.; Keller, A. *Colloid & Polymer Sci.* **1980**, *258*, 1023-1037.
33. Janeschitz-Kriegl, H.; Eder, G. *Journal of Macromolecular Science, Part B* **2007**, *46*, 591-601.
34. Kanaya, T.; Takayama, Y.; Ogino, Y.; Matsuba, G.; Nishida, K. *Lect. Notes Phys.* **2007**, *714*, 87-96.
35. McHugh, A. J. *Polym. Eng. Sci.* **1982**, *22*, (15-26).
36. Somani, R. H.; Yang, L.; Zhu, L.; Hsiao, B. S. *Polymer* **2005**, *46*, 8587-8623.
37. Yamazaki, S.; Hikosaka, M.; Toda, A.; Wataoka, I.; Gu, F. *Polymer* **2002**, *43*, 6585-6593.
38. Coppola, S.; Grizzuti, N.; Maffettone, P. L. *Macromolecules* **2001**, *34*, (14), 5030 - 5036.
39. Azzurri, F.; Alfonso, G. C. *Macromolecules* **2005**, *38*, 1723-1728.
40. Keum, J. K.; Zuo, F.; Hsiao, B. S. *Journal of Applied Crystallography* **2007**, *40*, 48-51.
41. Jerschow, P.; Janeschitz-Kriegl, H. *International Polymer Processing* **1997**, *12*, (1), 72-77.
42. Van der Beek, M. H. E.; Peters, G. W. M.; Meijer, H. E. H. *Macromolecules* **2006**, *39*, (5), 1805 -1814.
43. Pogodina, N. V.; Winter, H. H.; Srinivas, S. *Journal of Polymer Science: Part B: Polymer Physics* **1999**, *37*, 3512-3519.
44. Elmoumni, A.; Gonzalez-Ruiz, R. A.; Coughlin, E. B.; Winter, H. H. *Journal of Chemical Physics* **2005**, *206*, 125-134.
45. Stribeck, N., *X-ray scattering of soft matter*. Springer Laboratory: **2007**.

46. Balta-Calleja, F. J.; Vonk, C. G., *X-ray scattering of synthetic polymers*. Elsevier: Amsterdam, 1989.
47. Kumaraswamy, G.; Verma, R. K.; Kornfield, J. A.; Yeh, F.; Hsiao, B. S. *Macromolecules* **2004**, 37, (24), 9005-9017.
48. Wilchinsky, Z. W., *Advances in X-ray analysis*. 1962; Vol. 6.
49. van Meerveld, J.; Peters, G. W. M.; Hutter, M. *Rheol Acta* **2004**, 44, 119-134.
50. Dukovski, I.; Muthukumar, M. *Journal of Chemical Physics* **2003**, 118, (14), 6648-6655.
51. Somani, R. H.; Yang, L.; Hsiao, B. S. *Physica A* **2002**, 304, 145-157.
52. Dealy, J. M.; Larson, R. G., *Structure and Rheology of Molten Polymers*. Hanser Gardner Pubns: Cincinnati, **2006**.
53. Doi, M.; Edwards, S. F., *The theory of polymer dynamics*. Clarendon Press: Oxford, 1986.
54. McLeish, T. C. B. *Advances in Physics* **2002**, 51, (6), 1379-1527.
55. Yang, L.; Somani, R. H.; Sics, I.; Hsiao, B. S.; Kolb, R.; Lohse, D. *J. Phys. Condens. Matter* **2006**, 18, 2421-2436.
56. Peters, G. W. M.; Swartjes, F. H. M.; Meijer, H. E. H. *Macromol. Symp.* **2002**, 185, 277-292.
57. Fujiyama, M.; Wakino, T. *Journal of Applied Polymer Science* **1988**, 35, 29-49.
58. Kolb, R.; Seifert, S.; Stribeck, N.; Zachmann, H. G. *Polymer* **2000**, 41, 1497-1505.
59. Ran, S.; Zong, X.; Fang, D.; Hsiao, B. S.; Chu, B. *Macromolecules* **2001**, 34, 2569-2578.
60. Ruland, W. *Journal of Polymer Science: Part C* **1969**, 28, 143-151.
61. Xu, J.; Johnson, M.; Wilkes, G. L. *Polymer* **2004**, 45, (15), 5327-5340.
62. Avrami, M. *J. Chem. Phys.* **1939**, 7, 1103-1112.
63. Avrami, M. *J. Chem. Phys.* **1940**, 8, 212-224.
64. Avrami, M. *J. Chem. Phys.* **1941**, 9, 177-184.

Conclusions and recommendations

7.1 Conclusions / Technology assessment

Polyolefins, basically polyethylene (PE) and polypropylenes (PP), are materials with a vast number of applications. However, nearly seventy years after the industrial launch, their potential is not yet fully exploited. Smart processing, additives and control over molecular parameters can still enhance the performances of these olefin-based materials.

The mechanical, optical and transport properties of polyolefins are strictly related to crystallinity and crystalline morphology. For this reason, one of the key issues is understanding the crystallization behavior, especially in presence of flow, in order to be able to direct it in the desired way. Flow can enhance the crystallization kinetics, can change the morphology and can make crystallization happen even at temperatures where it is not expected, i.e. above the melting point (extended chain crystals).

During processing, the flow conditions (geometry, temperature, flow rate) should be tailored *in primis* to the molecular weight and to the molecular weight distribution of the melt but also to the additives that are present.

Self-assembling sorbitol-based additives (DBS, MDBS, DMDBS, etc.) are often used as nucleating/clarifying agent for isotactic polypropylene (iPP). At concentrations between 0.1 and 1 wt%, these additives can crystallize before iPP, leading to an interconnected network of nano-fibrils. The polymer crystallizes forming disk-like lamellae that grow in the direction of the radius of these nanofibrils. As a consequence, the orientation of iPP lamellae is controlled by the orientation of the nanofibrils at the onset of iPP crystallization. In absence of flow, DMDBS nanofibrils grow randomly oriented in the melt but they can be aligned with flow. Like in many other cases, flow can switch lamellar orientation on and off. However, when sorbitol based additives are used, there is a rather sharp transition between the flow conditions that can yield orientation and those that cannot. This transition is the crystallization of the additive. When a random lamellar orientation is desired, flow should be

applied at temperatures higher than the crystallization of the additive. On the other hand, when a high degree of lamellar orientation is desired, flow should be applied at temperatures lower than the crystallization of the additive. Such a procedure, in combination with ~0.5 wt% of DMDBS, can lead to a fully oriented iPP morphology after the application of flow at a temperature as high as ~200 °C.

Heterogeneous nucleation on oriented substrates can be used in several processes (e.g. spinning) where a high degree of lamellar orientation in the final product is demanded. The outstanding performances of sorbitol-based additives in iPP are due to: 1) a good dispersion in the polymer matrix; 2) a high aspect ratio of the nanofibrils; 3) a good epitaxy matching. Similar conditions, with a pre-aligned nano-fibrillar substrate templating the morphology of the bulk of the polymer, can be generated also in polyethylene (PE). Here the nanofibrils are made out of the same polymer and can be produced *in-situ* by inducing, with flow, the extended chain crystallization of the longest molecules of the melt. The molecular weight distribution of the melt needs to be carefully tailored on the flow conditions. Very broad and bimodal molecular weight distributions can fulfill the requirements as demonstrated in the thesis.

7.2 Recommendations for future research

Like all scientific contributions, this thesis tries to give few answers and puts forward many questions. Several aspects demand further clarification. Two outstanding questions are:

- Heterogeneous crystallization is based on the epitaxial relation (lattice matching) between the nucleating agent and the crystallizing polymer. Polymer molecules *prefer* to crystallize onto heterogeneous substrates because, below the melting point, the contact (adsorption) of a polymer molecule onto the foreign particle minimizes the energy of the system. What happens above the melting point? Is this scenario retained? And what are the consequences on the rheology of the melt?
- Formation of needle-like flow induced precursors with undetectable crystallinity is a typical example of ‘SAXS before WAXD’. Flow induced precursors assume the form of structures with only short range order. In this

thesis, by calling them *precursors*, we confine them in a black box. What is the structure of flow induced precursors? Do they differ from the precursors in quiescent conditions? Do they alter the rheology of the system? Do chains need to disentangle to generate a FIP?

- Polymers with broad molar mass distributions are often used in applications (e.g. film blowing). In these melts, there is a subtle balance between the relaxation times of long and short chains based on the life time of entanglements that can be very limited (constraint release). For the formation of oriented morphologies, what is more important? The high or the low molar mass?

Samenvatting

Synthetische polymeren worden momenteel geproduceerd in grote hoeveelheden, meer dan 200 miljoen ton op jaarbasis. Meer dan 70% van dit productie volume wordt ingenomen door de zogenaamde klasse van “Commodity Plastics”, te weten de bekende vier bulkpolymeren: polyethyleen (PE), polypropyleen (PP), polystyreen (PS) en polyvinylchloride (PVC). Polyethyleen en Polypropyleen vormen samen de subgroep Polyolefinen en deze klasse van polymeren is met meer dan 100 miljoen ton op jaarbasis de belangrijkste groep van industriële polymeren.

De aanduiding Polyolefinen of PE en PP is generiek, bijv. er worden van PE en PP tal van soorten geproduceerd die onderling verschillen in molmassa (ketenlengte), ketenstructuur (stereoregulariteit, vertakkingen etc.), allemaal toegesneden op specifieke toepassingen.

De eigenschappen van synthetische polymeren worden niet alleen bepaald door de chemische structuur van het polymeer maar ook door de verwerkingscondities tot eind produkt. Ketenoriëntatie is met name bepalend voor de mechanische eigenschappen met als extreem voorbeeld het verschil in eigenschappen tussen flexibele folies en containers en de supersterke vezel Dyneema® van DSM, allemaal gebaseerd op (lineair) PE maar met een verschil in keten oriëntatie en molmassa. Naast de chemische structuur en verwerkingscondities kan men de eigenschappen van polymeren ook sterk beïnvloeden door het gebruik van additieven en er zijn tal van additieven ontwikkeld zoals kleurstoffen, brandvertragers, anti-oxydanten en om bijv. de vloeit van de polymeren te verbeteren bij verwerking of ter verbetering van de mechanische eigenschappen zoals glasvezels ter verhoging van de stijfheid. In feite is een plastic (compound) een polymeer + additief!

In dit proefschrift is aandacht besteed aan het fenomeen van nucleatie, het begin van het kristallisatie-proces. Polymeren zoals PE en PP kunnen kristalliseren en het optreden van kristallisatie is zeer belangrijk voor de mechanische eigenschappen. Zonder kristallisatie zouden polymeren zoals PE en PP rond kamertemperatuur en/of verhoogde temperatuur niet gebruikt kunnen worden omdat het dan slechts hoog-visceuze vloeistoffen zouden zijn. Kristallisatie c.q. ordening van de lange polymeer moleculen in de bekende zogenaamde gevouwen-keten kristallen (lamellar folded-chain crystals) geeft versteviging aan PE en PP

tot aan het smeltpunt. Polypropeen (PP) is een uiterst traag kristalliserend polymeer en dat is inherent aan de structuur van het molecuul, een 3_1 helix in de kristallijne fase. Bij vormgeving, bijv. spuitgieten, is dit kristallisatie proces te traag. Om de *overall* kristallisatiesnelheid te verhogen worden zogenaamde kiemvormers toegevoegd die het ontstaan van kiemen, resulterend in kristallen, in het materiaal sterk bevorderen.

Er zijn twee typen kiemvormers bestudeerd, te weten:

- De bekende sorbitol derivaten die commercieel worden gebruikt en die als eigenschap hebben dat ze, gemengd met PP, assembleren in nano-fibrillen bij afkoelen voor dat de PP fase kristalliseert. Op deze nano-fibrillen kan PP gemakkelijk ontkiemen;
- Een mengsel van hoog- en laag-moleculair PE, gemaakt via een unieke zogenaamde “one pot” synthese waardoor de beide componenten op moleculaire schaal zijn gemengd. Onder afschuiving, zoals optreedt bij verwerking via de polymere smelt, zal de hoog-moleculaire component gemakkelijker oriënteren en deze gestrekte ketens fungeren als kiem voor kristallisatie van de laag-moleculaire matrix PE.

Bij het PP/sorbitol systeem werd gevonden dat bij zeer lage concentraties, < 1%, van het gebruikte type 1,3:2,4-bis (3,4-dimethylbenzylideen) sorbitol (DMDBS) zeer efficiënte kiemvorming optreedt en resulteert in zeer kleine PP kristallieten die nagenoeg geen licht verstrooien, dus geeft een transparant PP produkt. DMDBS is oplosbaar in gesmolten PP maar kristalliseert uit in nano-fibrillen, door zelf-assemblage, die fungeren als kiem voor kristallisatie van PP. Door gebruik te maken van gecombineerde temperatuur en afschuifprofielen kunnen de DMDBS nano-fibrillen worden georiënteerd in een bepaalde richting en dit biedt de mogelijkheid om unieke structuren te maken.

Bij het PE/PE systeem, respectievelijk laag- en hoog-moleculair PE, werd gevonden dat de hoog-moleculaire component kan worden georiënteerd boven het smeltpunt van de matrix, de laag-moleculaire component. Dit biedt de mogelijkheid tot nucleatie van de laag-moleculaire component op de gestrekte ketens van hoog-moleculair PE., in feite kristalliseert de laag-moleculaire PE component op hetzelfde materiaal, een perfecte vorm van epitaxy!

In conclusie, er werden twee systemen bestudeerd die ogenschijnlijk niets met elkaar te maken hebben maar het samenbindend element is het genereren van georiënteerde kiemen resulterend in unieke structuren c.s. morfologie van respectievelijk PP en PE.

Acknowledgements

Many people have contributed to this thesis and many have contributed to make my last four years in Eindhoven a real good time, I want to express my gratitude to everyone.

First of all, I would like to acknowledge the people who offered me the opportunity of doing a PhD and provided the necessary resources: Prof. Piet Lemstra, Prof. Sanjay Rastogi and Dr. Gerrit Peters.

I am grateful to Prof. Piet Lemstra for the motivations, the teachings and for instilling in my mind his research style, deeply scientific but always with an eye to applications. This work could not be done without Prof. Sanjay Rastogi, a daily source of inspiration. Thank you, Sanjay, for all the discussions and for the stimulating ideas that led to this thesis. Working with you, I learned a lot, challenging or validating the existing ideas, always with determination and enthusiasm. In addition, I want to thank you for the friendship that made me always feel comfortable. This thesis is largely due to Dr. Gerrit Peters. *Hartelijk bedankt*, Gerrit, for your inputs (including the idea of FIP) and for examining thoroughly the results with constructive criticism. You thought me to read the physics beyond the data and showed me positive thinking and great competence.

For this thesis, I made large use of X-rays. In my 22 (!) synchrotron (ESRF) experiments, I benefitted of the help of many people. I am grateful to the staff of the beamlines BM26/ DUBBLE, ID02 and ID11 of the ESRF for supporting our experiments. Here, I would like to mention the persons that introduced me to X-ray scattering: Dr. Guido Heunen and Dr. Ann Terry. Guido cleverly arranged setups at BM26 at all times of the day and of the night. Ann is a tireless coworker that solved many setup and software deadlocks at ID02 and ID11. The discussions with Wim Bras were important in building motivations. I also acknowledge Dr. Giuseppe Portale for the support at BM26, Dr. Caroline Curfs for ID11 and of Dr. Peter Boesecke for ID02. Colleagues from SKT and M@te gave their valuable contribution to several ESRF experiments. Above all, I am indebted with Jan-Willem Housmans for all the time spent at the ESRF, including the always present *dropjes*.

I had good time working in SKT where I benefitted of the support of several people. I would like to thank Dr. Han Goossens for the discussions and the comments, especially in the early stages of my PhD and Dr. Juan Fran Vega for teaching me the *tricks* of rheometry. My gratitude extends to Dirk Lippits for the stimulating discussions about rheology and for

calling me ‘*maestro*’, to Jules Harings for thorough discussions about my and his research that helped in building motivations, to Esther Vinken for the help with TGA and ‘that’ sms, to Nilesh Kukalyekar for the fruitful collaboration, to Irina Cotiuga for the discussions and the good time, to Joachim Loos, Anne Spoelstra and Pauline Schmit for microscopy, to Denka Hristova for the help in solving my initial problems with X-rays, to Sachin Jain for the discussions, to Joost Valetton for DSC, to Jules Kierkels for the help with X-rays and to Sainath Vaidya for the CNTs solutions. The list includes also my officemates at STO 0.42 Mano Prusty, Dirk Lippits and Gizela Mikova and the other people of SKT and PTG: Laurent Nelissen, Peter Koets, Mark van der Mee, Chunxia Sun, Lijing Xue, Rafiq Ahmed, Marjolein Diepens, Marjoleine Driessens, Roy l’Abee, Saeid Talebi, Weizhen Li, Maya Ziari, Bjorn Teurlings, Edgar Karssenbergh, Soney Varghese, Martijn Jansen, Cees Weijers, Thierry Leblanc. Thanks to Bob Fifield for all the incursions in my office, the handshakes and the always open debate about the reason why the Romans did not invade Wales. Thanks to Elly Langstad and Ineke Kollenburg for all the care. From the group M@te, I am grateful to Reinhard Forstner, Roel Janssen, Frederico Custodio and Rudi Steenbakkens for the discussions and the good time together, also at the ESRF. I also want to thank Sjef Garenfeld for providing help to my last minute requests.

My life in Eindhoven was always hectic thanks to some memorable characters. I was introduced *en la movida de Eindhoven* by Carlos. *Graciaaaaas*, Carlos, for being a *real* friend. All the events (including the FORT) together with Blanca, David, Ben and Chiara have something to be remembered. I enjoyed these times like *there is no tomorrow*. Unforgettable. This list cannot be closed without acknowledging the friendship of Dillip (is he spanish?), the class of Brett, the black clothing of Chris, the bbqs of Dani, the world according to Kuba, the dinners of Lorenzo, the sweetness of Mari, the twisted reasoning of Vincente, the French accent of Emilie, the smiling eyes of Amparo, the sincerity of Víctor and the smiles of Monica.

Last and certainly not least, Chiara. I take the risk of being banal saying that you gave me incredible support. We had great time and you also tolerated my difficult moments. I thank you for the comprehension and the patience.

Per chiudere, ringrazio la mia famiglia per tutto il supporto e gli incoraggiamenti ricevuti e quella Rabotti per la stima e le vacanze in Toscana.

Curriculum Vitae

The author was born in Pompei, Italy, on June 25th 1977. After finishing secondary school (Liceo Scientifico 'E.Pascal', Pompei), he studied Chemical Engineering at the University 'Federico II' of Naples (Italy). He completed his master thesis, entitled 'Temperature effects in flow induced crystallization of thermoplastic polymers' under the supervision of Prof. Nino Grizzuti.

At the beginning of 2004, he started his Ph.D. in the Polymer Technology group (SKT) of Prof. P.J. Lemstra at Eindhoven University of Technology under the guidance of Prof. dr. S.Rastogi and dr. G.W.M. Peters.